Title
A Mass Spectrometry Study of Isotope Separation in the Laser Plume

Author
Suen, Timothy Wu

Publication Date
2012

A Mass Spectrometry Study of Isotope Separation in the Laser Plume

by

Timothy Wu Suen

A dissertation submitted in partial satisfaction of the

requirements for the degree of

Doctor of Philosophy

in

Engineering – Mechanical Engineering

in the

Graduate Division

of the

University of California, Berkeley

Committee in charge:

Professor Samuel S. Mao, Co-Chair
Professor Ralph Greif, Co-Chair
Professor Costas Grigoropoulos
Professor Tsu-Jae King Liu

Fall 2012

A Mass Spectrometry Study of Isotope Separation in the Laser Plume

by

Timothy Wu Suen

Abstract

A Mass Spectrometry Study of Isotope Separation in the Laser Plume

by

Timothy Wu Suen

Doctor of Philosophy in Engineering – Mechanical Engineering

University of California, Berkeley

Professor Samuel S. Mao, Co-Chair
Professor Ralph Greif, Co-Chair

Accurate quantification of isotope ratios is critical for both preventing the development of illicit weapons programs in nuclear safeguards and identifying the source of smuggled material in nuclear forensics. While isotope analysis has traditionally been performed by mass spectrometry, the need for in situ measurements has prompted the development of optical techniques, such as laser-induced breakdown spectroscopy (LIBS) and laser ablation molecular isotopic spectrometry (LAMIS). These optical measurements rely on laser ablation for direct solid sampling, but several past studies have suggested that the distribution of isotopes in the ablation plume is not uniform.

This study seeks to characterize isotope separation in the laser plume through the use of orthogonal-acceleration time-of-flight mass spectrometry. A silver foil was ablated with a Nd:YAG at 355 nm at an energy of 50 μJ with a spot size of 71 μm, for a fluence of 1.3 J/cm^2 and an irradiance of 250 MW/cm^2. Flat-plate repellers were used to sample the plume, and a temporal profile of the ions was obtained by varying the time delay on the high-voltage pulse. A spatial profile along the axis of the plume was generated by changing the position of the sample, which yielded snapshots of the isotopic composition with time. In addition, the reflectron time-of-flight system was used as an energy filter in conjunction with the repellers to sample slices of the laser plasma orthogonal to the plume axis.

Mass spectrometry of the plume revealed a fast ion distribution and a slow ion distribution. Measurements taken across the entire plume showed the fast ^{109}Ag ions slightly ahead in both space and time, causing the ^{107}Ag fraction to drop to 0.34 at 3 μs, 4 mm from the sample surface. Although measurements centered on the near side of the plume did not show isotope separation, the slow ions on the far side of the plume included much more ^{109}Ag than ^{107}Ag. In addition to examining the isotope content of the ablation plume, this study has developed a mass spectrometry characterization technique that may be useful for investigating chemical reactions during laser ablation.

Contents

Acknowledgments

Performing the research described in this thesis has been the most challenging endeavor I have undertaken thus far. Without some of these people, it would have been impossible. With the rest, it would simply have been excruciating.

First of all, I would like to thank Prof. Sam Mao and Dr. Rick Russo for letting me work in their labs. I would like to thank my committee members Prof. Costas Grigoropoulos and Prof. Tsu-Jae King Liu for helping me along with this process and Prof. Ronald Gronsky for teaching me the difference between science and engineering. I owe an enormous debt of gratitude to Dr. Xianglei Mao, who helped me set up many experiments and looked at every graph, and Prof. Ralph Greif, who was instrumental in the writing process and provided invaluable guidance throughout.

I enjoyed many conversations with and learned a lot about science and politics from Coleman Kronawitter, Derrick Speaks, Deang Liu, Matt Beres, Matt Rogers, Russell Carrington, Steve Barcelo, and Tony Ho from Sam's lab and Meirong Dong, Inhee Choi, Ivan Lu, Travis Owens, and Vassilia Zorba from Rick's group. It was always incredibly fun and productive working with Carlos Cabezas, Daniele Pergolesi, and Joe Savina.

I would like to thank Eli Patten, Esha Datta, Heather Chiamori, Kim Lau, Pam Berkeley, Ryan Shelby, and Vera Dadok from the mechanical engineering department for their friendship and encouragement. My Berkeley experience would not have been complete without David Kim, Jean Lyu, Jenny Lee, Matt Satriano, Rob Lee, and Vimalier Reyes-Ortiz. I would also like to thank Amy Wibowo, Heidi Hsieh, Kim Kam, Rick Henrikson, Roy Esaki, and Xiaoyu Gu from undergrad and Aaron Greenspan, Curtis Fabens, and Philip Wong from before that. Thanks especially to Lisa Porter for reminding me to breathe and to my roommates David Hoffman and Ari Simmons for putting up with me.

The love and support of my father, my mother, and my sister Lucy go without saying.

Special thanks to Ray Cho, Amy Wong, Rashmi Singh, Mike Fina, and David Moody for keeping me sane.

Through Lawrence Berkeley National Laboratory, this research was supported by the Office of Science, Office of Basic Energy Sciences, Chemical Sciences, Geosciences, and Biosciences Division, and the Deputy Administrator for Defense Nuclear Nonproliferation, Research and Development of the US Department of Energy under Contract No. DE-AC02-05CH11231.

Chapter 1

Introduction and Background

Over two decades after the end of the Cold War, nuclear weapons remain at the heart of America's most pressing foreign policy challenges [1]. Ever increasing sanctions are being leveled against Iran in an effort to dissuade the government from seeking further nuclear capabilities [2, 3], while food aid has been offered to cajole North Korea back to negotiations regarding its existing weapons program [4, 5]. The United States' difficult relationship with Pakistan is exacerbated by concerns over both terrorist activity and the security of its rapidly increasing nuclear arsenal, the combination of which is particularly troubling [6].

1.1 Nuclear Safeguards and Nuclear Forensics

Although the diplomatic scenarios differ greatly, the characterization of nuclear materials plays a critical role in each of these situations. With regard to preventing the spread of nuclear weapons, analysis of nuclear materials falls broadly into two categories: safeguards and forensics. The purpose of nuclear safeguards, as detailed in the Non-Proliferation Treaty (NPT), is to prevent countries without nuclear weapons from developing weapons programs [7]. In exchange, nuclear weapons states are to make civilian nuclear technologies available to non-nuclear states. In accordance with the NPT, all signatories must declare their nuclear activities, which are then subject to verification by the International Atomic Energy Agency (IAEA) [8, 9]. By checking for undeclared activity and ensuring compliance with the NPT, IAEA inspections aim to limit the number of countries with nuclear weapons, thereby avoiding a worldwide arms race and reducing the risk of nuclear war [10, 11]. While safeguards are designed to keep countries from starting weapons programs, nuclear forensics is concerned with identifying illicit nuclear material after it has been discovered [12, 13]. In particular, nuclear forensics seeks to determine the origin of smuggled material, especially in the case of a terrorist attack. If the source of the nuclear material can be identified, security can be strengthened in order to break the supply chain and prevent further theft or diversion. In the case of a terrorist detonation of a nuclear device, this ability to trace the material may be enough to help avert a second or third explosion [13, 14]. Although nuclear forensics is directly applicable after a terrorist act or in the confiscation of nuclear material on the black market, the capability to identify the source of such material can serve a broader goal of deterrence [1, 14]. If the nuclear material in any given terrorist attack could be reliably traced back to the national program that produced it, it would be possible to hold that country responsible for supreme negligence, turning a blind eye to if not directly abetting terrorist groups. Therefore, by making it possible for the United States to threaten retaliation against governments whose nuclear material was used in an act of terrorism, accurate nuclear forensics might encourage those nations to maintain tighter control over their weapons programs, restricting the availability of weapons and materials to terrorist organizations.

Since safeguards verify that nuclear activity is as declared while nuclear forensics seeks to identify nuclear material of an unknown origin, there are differences in the tools and analytical techniques used for each purpose. For instituting safeguards, the IAEA has developed a comprehensive system for collecting and analyzing swipe samples from nuclear facilities that focuses primarily on isotopic analysis [8, 15], with an emphasis on individual particles [9, 16]. Nuclear forensics, on the other hand, makes use of a much broader array of analytical techniques, from trace chemical analysis [17, 18] to structural morphology [19]. Even the physical dimensions of seized material may be important, if the size and shape of a fuel assembly point to a specific type of reactor [18]. For both safeguards [16] and forensics [20], however, isotopic analysis plays a critical role, providing information about intended use, reactor conditions, age, and chemical processing.

1.2 Parameters Affecting Isotopic Composition

Nuclear weapons and nuclear energy are based on fission, for which the most relevant isotopes are ^{233}U, ^{235}U, and ^{239}Pa [10, 21]. Although fissionable isotopes are responsible for the energy produced in both reactors and weapons, explosive devices require a much higher concentration of these isotopes in order to sustain a rapid chain reaction. Under IAEA safeguards, nuclear material is typically considered weapons grade if the uranium includes more than 20% ^{235}U [10] or the plutonium less than 6% ^{240}Pu [22]. The cutoff for uranium is somewhat arbitrary in that critical mass can be achieved at lower levels of enrichment, but progressively larger amounts of ^{235}U are needed [11, 23]. Analysis of individual particles, in addition to digesting entire swipe samples, is especially important for uranium, because minute amounts of enriched uranium can be masked by larger quantities of natural or depleted uranium [8]. Plutonium, on the other hand, demands higher purity for weapons use, because ^{240}Pu undergoes spontaneous fission, which can cause the device to explode before reaching maximum criticality and drastically reduce the yield in a “fizzle” [11, 21]. The additional heat generated by ^{240}Pu also makes lower grade material more difficult to handle, especially since standard implosion devices require the plutonium to be surrounded by high explosives [22].

The fissionable isotope ^{239}Pu is produced from ^{238}U by neutron capture, and additional neutron irradiation yields the heavier isotopes ^{240}Pu, ^{241}Pu, and ^{242}Pu [21]. Thus, fuel elements in reactors for weapons material are typically removed when ^{240}Pu/^{239}Pu is between 0.05 and 0.07. Due to economic constraints, fuel rods in commercial reactors typically undergo higher burn-up [21, 24], generating a significant quantity of heavier plutonium isotopes, which can not be used in weapons due to either a large number of spontaneous neutrons or rapid radioactive decay [22]. The exact distribution of plutonium isotopes depends on the reactor type, initial fuel composition, moderator type, neutron flux and energy spectrum, and burn-up [20]. A hardened neutron energy spectrum, for example, produces a smaller proportion of heavier plutonium isotopes, due to higher rates of fission during neutron capture. Given the reactor type, initial enrichment, and burn-up, simulations can be used to calculate the expected isotope content of spent fuel, and comparison with analytical measurements can confirm declared activity in safeguards [16] or determine material origin in forensics [20].

In addition to material use and reactor processing, age is an important parameter that can be determined from isotope analysis. For uranium and plutonium, parent/daughter ratios can be used to measure the amount of time since the last chemical separation [25]. Assuming that the daughter nuclides were completely removed from the parent element during the last chemical processing step, any further buildup of daughter products must be due to radioactive decay. If the previous separation was incomplete, the preexisting daughter nuclides will cause the age to be overestimated. For uranium, the most relevant parent/daughter pairs are ^{234}U/^{230}Th and ^{235}U/^{231}Pa, and for plutonium they are ^{238}Pu/^{234}U, ^{239}Pu/^{235}U, ^{240}Pu/^{236}U, ^{241}Pu/^{241}Am, and ^{242}Pu/^{238}U [19, 25]. The proportion of daughter nuclides tends to be very low because of the relatively short periods of time since chemical separation, compared to the half-lives of the parent. As a result, high sensitivity is required for an accurate calculation of age. The ^{241}Pu/^{241}Am ratio is measured using gamma spectrometry while the other ratios are typically obtained by thermal ionization mass spectrometry (TIMS) after the elements have been chemically separated [25]. In forensics, age determination can be used to trace the sample to a specific stock of nuclear material, especially for plutonium that has been separated from spent fuel. With safeguards, dating is important for confirming that facilities listed as decomissioned have indeed been shut down [16]. The age of an enriched sample can help distinguish whether the material originated from existed stockpiles or was generated in recent production [26].

Fission and activation products around an existing reactor [16] or from atmospheric surveillance stations after a detonation [27] can also be quantified for determining the timeframe of nuclear activity. In the case of safeguards, fission products, such ^{106}Ru with a half-life of 374 days, and activation products, such as ^{134}Cs with a half-life of 2.1 years, are measured by gamma spectrometry and compared to model predictions for a given reactor type and burn-up in order to verify operations at a facility [16]. Similarly, a network of control posts established to track ^{135}Xe with a half-life of 9.14 hours and ^{140}Ba with a half-life of 12.75 days was used in conjunction with weather observations to date clandestine testing of nuclear weapons in North Korea to within a day [27]. Atmospheric monitoring has aspects of both safeguards, in preventing undeclared activity, and forensics, in identifying the material used in a detonation.

Finally, it may be possible to use the isotopic composition as a signature in forensics to identify the source of the raw ores from which an unknown sample of uranium was produced [17, 28]. Of the four isotopes of lead, ^{206}Pb, ^{207}Pb, and ^{208}Pb are produced from the radioactive decay of ^{238}U, ^{235}U, and ^{232}Th respectively [17]. As a result, the isotopic composition of lead in uranium ore can vary significantly from the natural abundance values, depending on the age of the ore and the original uranium and thorium content. Since the isotope ratios of lead frequently differ from one mine to another and one production plant to another, they can be used as one of several indicators for tracing the origin of nuclear material. Similarly, the oxygen isotope ratio varies slightly by region and can serve as part of the isotopic signature of a sample [28]. Because many reactors use oxide fuels [21] and uranium and plutonium mostly appear as oxides in collected particles [28], secondary ionization mass spectrometry (SIMS) of the oxygen isotope ratio is being considered for this application.

1.3 Standard Methods for Measuring Isotopes

Multiple techniques are available for quantifying the isotopic composition of a sample. Each method has specific advantages and disadvantages, typically with accuracy and precision balanced against convenience and speed. Typical levels of precision for different methods of mass spectrometry are listed in Table 1, but accuracy for any given measurement will vary with the sample composition, sample preparation, calibration methods, and mass analyzer [29, 30]. Although gamma ray spectrometry is also a powerful tool for isotope detection, its principles of operation are based on radioactive decay instead of the mass-to-charge ratio and can not be compared directly with the mass spectrometry techniques.

Ionization Method	Single Ion Collector (%)	Multiple Ion Collector (%)
Thermal Ionization Mass Spectrometry (TIMS)	0.01-1	0.001-0.01
Secondary Ionization Mass Spectrometry (SIMS)	0.01-1	0.002-0.1
Inductively Coupled Plasma Mass Spectrometry (ICP-MS)	0.02-2	0.001-0.01
Laser Ablation Inductively Coupled Plasma Mass Spectrometry (LA-ICP-MS)	0.08-1	0.006-0.02
Resonance Ionization Mass Spectrometry (RIMS)	5	-

Table 1 Precision of mass spectrometry methods [29, 30]

1.3.1 Gamma Ray Spectrometry

Gamma ray spectrometry will be the only technique discussed in this section that relies on measuring emitted radiation rather than the isotopes themselves. Gamma rays are released during the radioactive decay of unstable isotopes [31]. When radioactive nuclides undergo beta decay, in which a neutron is converted to a proton, or alpha decay, in which a ^{4}He nucleus is emitted, the transition often leads to an excited state of the daughter nuclide. As that daughter nuclide drops from that excited state to the ground state, characteristic gamma radiation is emitted. In detectors based on insulators and semiconductors, each gamma ray produces a high-energy primary electron, which interacts with other electrons to set off a cascade of electron-hole pairs in the material. The number of electron-hole pairs ultimately generated is proportional to the energy of the original gamma ray. While scintillators, such as NaI(Tl), have traditionally been used to detect gamma rays, semiconductors, such as Ge and CdZnTe, have much better energy resolution [31, 32]. High-purity germanium (HPGe) detectors have become the standard for high-resolution measurements but require liquid nitrogen cooling to minimize the leakage current, whereas CdZnTe has worse resolution but can be used in more compact applications.

One of the main advantages of gamma spectrometry is that it can be performed nondestructively with no sample preparation [31, 33]. Because it is possible to detect gamma rays through most packaging, samples can even be scanned in their original bags and bottles, minimizing the possibility of contamination [16, 19]. In addition, different nuclides release gamma rays of different energies, so the technique is inherently selective to radioactive isotopes. As a result, gamma spectrometry is a critical tool for initial screening in both forensics and safeguards. Quantitative analysis, however, is considerably more challenging. Lines with similar energies should be chosen to minimize differences in absorption efficiency, and corrections for self-absorption may be required, depending on the geometry of the sample [31, 33, 34]. In addition, many radioactive nuclides do not release gamma rays during alpha and beta decay, so emission from the daughter products must be used instead and those daughters should be in secular equilibrium with the parent when the measurements are taken [31, 33]. Furthermore, branching of the decay chain may reduce the available signal. ^{239}Pu and ^{240}Pu, in particular, have very low gamma-emission probabilities and release low-energy gamma rays that must be distinguished from nearby X-ray peaks that are produced by self-fluorescence. Because of this, sophisticated programs, such as the Multi Group Analysis code [19, 35], are needed to deconvolute the spectra. Data from uranium samples tends to be easier to interpret, although there can be overlap between the ^{226}Ra and ^{235}U peaks in environmental samples [31, 34] as well as between the Th K_{α_1} X-ray line, whose fluorescence is used as a proxy for the decaying ^{235}U, and ^{234}Th gamma emission, a measure of ^{238}U [34]. While HPGe detectors make it possible for isotopes ratios to be measured to 1% accuracy in certain samples, significant technical complications remain.

1.3.2 Thermal Ionization Mass Spectrometry (TIMS)

First used in 1918, thermal ionization mass spectrometry (TIMS) is one of the oldest methods of performing mass spectrometry [36]. It is the most established method described in this section and remains the gold standard for measuring the isotope ratio [30, 37]. TIMS uses filaments made from refractory elements with high work functions, such as Re, Ta, Pt, or W, to atomize and ionize samples for mass spectrometry [37]. While both functions can be performed by a single filament, most instruments use two filament facing each other, one for vaporization and the other for ionization, in order to maintain better control over the process. In TIMS, the sample is deposited on the vaporization filament as an aqueous solution, often in the chloride, nitrate, or oxide form of the element. The filament is dried and mounted in the instrument, where resistive heating is used to heat the filament and atomize the sample under vacuum. As the evaporated neutrals migrate toward the ionization filament, the Fermi level of the atom approaches that of the surface and electrons are exchanged between the atom and the metal filament [30, 37]. The probability that the atom will be ionized is given by the Langmuir-Saha equation [30],

$$\alpha = \frac{n^+}{n_0} = \frac{g^+}{g_0} \exp\left(\frac{\phi - E_i}{kT}\right) \tag{1.1}$$

where α is the ionization yield, n^+ and n^0 are the number of ions and neutral atoms respectively, g^+ and g^0 are the degeneracy of the ionized and neutral states respectively, ϕ is the work function of the filament surface, E_i is the ionization energy of the atom being ionized, k is the Boltzmann constant, and T is the temperature in Kelvin. Thus, the ionization filament needs to have a high work function and operate at high temperatures in order to increase the ionization yield. The vaporization filament, on the other hand, only needs to be hot enough to produce the desired rate of evaporation [37]. Once the sample is atomized and ionized, it is accelerated by an electric field into the mass analyzer, usually a sector instrument with a multicollector for maximum precision in the isotope ratio. Because the thermal ions produced by this technique have very low kinetic energy, down to 0.1-0.2 eV, only a single magnetic sector field is needed for mass analysis [30, 38].

The controlled ionization process allows TIMS to achieve 0.01% precision for single ion collectors and 0.001% with multicollector systems, making it suitable for measuring even fine isotopic variation in nature [30, 38]. Furthermore, only nanograms are needed for precise measurements [25]. The samples, however, should only include the element of interest, and this often necessitates laborious chemical separation [17, 37]. Taking a TIMS measurement is also very time-consuming, and large filament turrets are commonly used for automation [37, 38]. Because the yield is dependent on the ionization potential, standard procedures can only measure elements with an ionization energy up to 7 eV, which includes uranium and plutonium [30]. In addition, lighter isotopes evaporate preferentially from the vaporization filament, so reference calibrations are needed. Although TIMS requires extensive sample preparation and long measurement times, it remains the standard tool for precise quantification of the isotope ratio.

1.3.3 Secondary Ionization Mass Spectrometry (SIMS)

Secondary ionization mass spectrometry (SIMS), on the other hand, performs multi-elemental analysis of the surface and requires little sample preparation [37]. In SIMS, the sample is placed under high vacuum and bombarded by a stream of primary ions, such as Ar^+, Cs^+, Ga^+, O^-, $O_2{}^+$, with an energy of 0.2-40 keV [30, 39]. As the primary ions are implanted in the solid sample, the kinetic energy is transferred back along impact cascades, causing charged and neutral species to be sputtered from the surface. Of these particles, 1% are ions and can be processed by the mass analyzer. Because of the large kinetic energy spread of the ions, double focusing mass analyzers that can handle both velocity and direction focusing are necessary [37].

Although SIMS and corresponding neutral sputtering techniques can be performed on almost any solid sample, the ion yields are highly matrix-dependent [30], and matrix-matched standards are needed for quantitative analysis [38, 39]. There is an exponential relationship between positive ion yields and ionization energy and between negative ion yields and electron affinity [40], so the relative sensitivity can vary by orders of magnitude for different elements [30]. The yield is also heavily influenced by the composition and energy of the ion beam. The advantages of ion beam sputtering, however, include the ability to perform depth profiling with a resolution of 2-5 nm and microprobe analysis with a lateral resolution of 50 nm at high levels of sensitivity for a wide range of elements [30]. This has allowed the characterization of plutonium and uranium particles with diameters down to 10 μm [41], a useful capability for both safeguards [16] and forensics [28].

1.3.4 Inductively Coupled Plasma Mass Spectrometry (ICP-MS)

Although the inductively coupled plasma (ICP) was originally developed for optical emission spectroscopy [42], inductively coupled plasma mass spectrometry (ICP-MS) has become the more popular technique due to its high sensitivity and comparatively simple spectra [37, 43]. The ICP is produced by induction heating of a noble gas, typically argon, in a torch consisting of three concentric quartz tubes. The sample flows through the innermost tube, carried as an aerosol by the argon gas, and an auxiliary flow of argon in the middle tube forces the plasma away from the torch, keeping it from melting the quartz tubes [43, 44]. The plasma is generated in the argon gas that flows between the middle tube and the outer tube as it passes through the copper induction coils at the end of the torch. These load coils are connected to a radio-frequency power source, which creates an oscillating electric field that accelerates the electrons into neutral atoms, ionizing the argon and sustaining the plasma at about 8000 K. The ions produced in this plasma are then coupled into a mass analyzer through orifices in a water-cooled sampling cone and a skimmer cone [37, 43]. Differential pumping in the space between the two cones allows the ions to transition from the plasma in atmosphere to the high vacuum of the mass analyzer.

The ICP ionizes almost completely all atoms with ionization potentials below 8 eV [45] and produces singly charged ions with a low energy spread [37], making it an excellent source for mass spectrometry. While the nebulizer requires the sample to be in solution, the ability for ICP-MS to perform multielement analysis simplifies sample preparation considerably, and measurements can be performed in minutes [45]. Furthermore, although only a small percentage of ions makes it to the detector, the sensitivity remains fairly high [30]. Isobaric interferences, however, can occur from oxides, hydrides, and combinations with Ar [37, 44, 46]. In addition, significant mass fractionation is caused by lighter isotopes being deflected off-axis as they leave the skimmer, which can result in the suppression of light elements when amidst heavier matrix ions [44, 47]. ICP-MS allows for rapid trace analysis with relatively little sample preparation, but, due to the need to correct for isobaric interferences and mass fractionation, it can be challenging to obtain precise isotope ratios [48, 49].

Coupling laser ablation to ICP-MS allows for direct solid sampling with the mass spectrometer. In laser ablation-inductively coupled plasma-mass spectrometry (LA-ICP-MS), material removed by laser ablation of the sample surface is carried by the flow of Ar gas from a sealed ablation cell to the ICP torch [30]. Since laser ablation can be used under atmospheric conditions to vaporize almost any material, minimal sample preparation is required and LA-ICP-MS can be performed in situ without limitations on the sample matrix [50]. This technique offers low detection limits [51], high throughput, and typical spatial resolutions of 10 µm [52]. The measurements, however, are heavily influenced by the ablation dynamics, which includes many complicated and coupled phenomena. Particle formation in the laser plume, for example, is considered one of the major sources of elemental and isotopic fractionation [53]. Laser fluence, wavelength, and pulse duration are key parameters of laser ablation and must be optimized for individual experiments [50], with shorter wavelengths [54] and shorter pulses [55] usually leading to lower levels of fractionation.

1.3.5 Resonance Ionization Mass Spectrometry (RIMS)

In resonance ionization mass spectrometry (RIMS), tunable lasers matched to the optical resonance lines are used to excite an atom from the ground state to an excited energy level [56, 57]. The excited atom then absorbs additional photons, from the same laser or a different laser, until it becomes ionized and enters the mass analyzer. For coupling with pulsed lasers, time-of-flight systems are often used [37]. Depending on the setup, these experiments can even take advantage of multiple lasers with different wavelengths to enhance the signal and selectivity [56, 58]. Since the laser wavelength is precisely tuned to the resonance excitation, RIMS is extremely selective, with very little isobaric interference, and has high ionization efficiencies. As a result, ultratrace elements can be detected in the femtogram range [57]. Due to the cost of tunable lasers and the complexity of the experimental apparatus, RIMS has not become widespread [30]. Furthermore, RIMS can only be applied once the sample is in the gas phase, so an initial vaporization step, such as sputtering or laser evaporation, is still required [58].

1.4 Optical Approaches to Measuring Isotopes

While mass spectrometry techniques are the most quantitative for measuring isotopes, they all rely on mass analyzers in vacuum [30] and often require either signficant sample preparation, in the case of TIMS [25], or complicated equipment for direct solid sampling, as is the case for SIMS [39] and LA-ICP-MS [55]. The need to operate instrumentation under vacuum or with argon gas, in particular, excludes the possibility of isotope characterization being performed on site, a critical feature for both safeguards and forensics [59]. The use of optical approaches for obtaining the isotope ratio is thus appealing, because vacuum systems are not strictly necessary. Although a low-pressure background gas is often used to minimize Stark broadening [60, 61], the isotopes can be distinguished in atmosphere given the appropriate plasma conditions and detection parameters [59, 62]. In addition, if laser ablation is used for vaporization, samples can be measured in situ or even at a distance in stand-off analysis [63]. Eliminating sample preparation not only reduces the amount of time needed for each measurement but also avoids contamination between samples [54, 61]. To address the need for portable, in situ instruments for monitoring isotopes, this section will survey optical techniques that use laser ablation for solid sampling.

1.4.1 Laser-Induced Fluorescence

Smith et al. [61] first combined laser ablation with laser-excited atomic fluorescence in 1998 to measure the isotope ratio of lithium, which has an isotopic shift of 15 pm in the fine structure. Ablation was performed on a pressed pellet of lithium oxalate by an excimer laser at 308 nm with an irradiance of 50 MW/cm^2. The plume was scanned by a dye laser over the Li doublet at 670 nm, and a photomultiplier tube (PMT) at right angles with the excitation laser was used in conjunction with a monochrometer for detection. With an optimal argon pressure of 0.01 Torr and probe distance of 1 cm from the sample surface, a ^{7}Li/^{6}Li ratio of 12.1 ± 0.5 was obtained for a relative standard deviation (RSD) of 5%, compared with 11.95 ± 0.08 by ICP-MS.

This technique was refined for determining the isotope ratio of depleted UO$_2$ [64]. A ^{238}U line at 682.6913 nm and a ^{235}U line at 682.6736 nm provided a separation of 17.7 pm in the spectra. A Nd:YAG laser at 1064 nm, optimized at 0.5 mJ per pulse for a fluence of 8.8 J/cm^2 and an irradiance of 880 MW/cm^2, was used for ablation. The probe laser was aligned perpendicular to the plume, and a monochrometer with a PMT, orthogonal to both the probe laser and the plume, was used to detect emission. At optimal conditions of 0.9 mbar argon atmosphere, 0.8 cm from the sample surface, a ^{235}U fraction of 0.39 ± 0.05% was found for the 0.407% ^{235}U sample (13% RSD) and a ^{235}U fraction of 0.18 ± 0.05% for the 0.204% sample (27% RSD). The detection limit was estimated at 0.6 mg/g. The precision was limited by continuum emission from the laser plasma, which had to be subtracted from the signal to obtain the fluorescence intensity, even at long delay times of 500 μs and especially for the ^{235}U minor isotope. Shot-to-shot variation caused by degradation of the sample surface also contributed to uncertainty in the measurement.

1.4.2 Atomic Absorption Spectrometry

Due to interference from broad-band emission during laser ablation, laser-induced fluorescence could only be measured at long timescales, after the plasma had become relatively cold [65]. By this point, however, the numder density within the sampled region had been greatly reduced, and the concentration of minor isotopes was even lower. Atomic absorption spetrometry avoids background emission by using a small solid angle for detection. The detector is placed in line with the probe laser and only needs to be as large as the laser beam, minimizing the signal from continuum emission.

This technique was first used to study isotopes of rubidium in a $CaCO_3$ matrix [66]. A Nd:YAG laser at 1064 nm with an energy of 100 mJ and an irradiance of 2 GW/cm^2 was used to generate the plasma, which was scanned by a Ti:Sapphire laser at 780.02 nm. The intensity of the probe beam was monitored by a PMT coupled to a monochrometer. The best spectral resolution was observed at 0.15 Torr argon with a delay time of 120 µs, but a pressure of 2.5 Torr and a delay time of 75 µs were used to increase the signal when measuring the isotope ratio. A ^{85}Rb/^{87}Rb ratio of 2.7 ± 0.2 (5% RSD) was obtained compared to 2.68 ± 0.03 by ICP-MS, with a detection limit of 24 ppm for both isotopes.

Quentmeier et al. [65] used a similar method to measure the ^{235}U abundance in depleted uranium. The sample was ablated using an Nd:YAG at 1064 nm with an energy of 7.5 mJ focused to a spot diameter of 85 µm, for a fluence of 130 J/cm^2 and an irradiance of 13 GW/cm^2. Conditions were optimized to an argon pressure of 30 mbar, 3 mm from the sample surface to give a ^{235}U fraction of 0.38 ± 0.02% for the 0.407% ^{235}U sample (5% RSD) and 0.22 ± 0.03% for the 0.204% sample (13% RSD). The detection limit of 100 µg/g for ^{235}U was an order of magnitude lower than obtained from laser-induced fluorescence. Line-broadening from ^{238}U contributed significantly to the ^{235}U background and was the limiting factor in its precision.

Liu et al. [67] used two diode lasers separated by 4° to measure ^{235}U and ^{238}U simultaneously. This yielded a ^{235}U fraction of 0.686 ± 0.119% compared to the natural abundance of 0.719% for an accuracy of 5% and precision of 17% RSD, with poor shot-to-shot reproducibility attributed to inhomogeneities in the sample. The limit of detection for ^{235}U was estimated at 47 µg/g. Two diode lasers were also used to measure ^{152}Gd at 405.9 nm and ^{160}Gd at 413.4 nm in micron-size particles [68]. In this case, the beamlines of the two probe lasers were overlapped using a beam splitter and then separated with a holographic grating after passing through the ablation plume.

1.4.3 Laser-Induced Breakdown Spectroscopy (LIBS)

Laser-induced breakdown spectroscopy (LIBS) is a more basic technique than laser-induced fluorescence and atomic absorption spectrometry in that there is no additional excitation other than the ablation itself [50]. After the shot is fired, a monochrometer is simply used to record the optical emission from the laser plasma generated during ablation. Without an additional probe laser, however, sampling and excitation are coupled and optimizing the plasma properties is critical.

The use of LIBS for obtaining the isotope ratio of uranium was demonstrated by Pietsch et al. in 1998 [60]. A XeCl excimer laser at 308 nm with an energy of 400 mJ per pulse and an irradiance of 460 MW/cm^2 was used to ablate samples of natural and enriched uranium. A 1-m spectrometer was coupled to a PMT for termporal profiles and to an intensified charge-coupled device (ICCD) for recording entire spectra at once. The ionic transition at 424.437 nm, which has an isotopic shift of 25 pm, was used for the study. In order to minimize Stark broadening, the samples were measured under reduced pressure at 0.0267 mbar using delay times greater than 250 ns. At this point, Doppler broadening resulted in a line width of 12 pm, over twice the instrumental limit of 5.5 pm. A relative precision of 5% was estimated for 3.5% ^{235}U, and deconvolution was necessary to remove the ^{238}U wing from the baseline of the ^{235}U peak.

Smith et al. [69] used a helium buffer gas at 133 mbar and a longer delay time of 1 µs to study the ^{239}Pu/^{240}Pu ratio, which has an isotopic shift of 12.55 pm at 594.52202 nm. The plasma was generated by ablation from a Nd:YAG at 1064 nm with an energy of 25 mJ per pulse and an irradiance of roughly 10 MW/cm^2, and the spectra were recorded on a 2-m spectrometer coupled to an ICCD. The observed plutonium linewidths of 6.7 pm were just above the theoretical instrument linewidth of 5.2 pm, allowing the individual isotope peaks to be clearly resolved.

The ability to differentiate between hydrogen and deuterium using LIBS has been demonstrated for mixtures of water and heavy water in helium gas at 1 Torr [70] and for mixtures of $NaBD_4$ and $NaBH_4$ in a sealed reaction cell [71]. Although the hydrogen and deuterium lines at 656.3 nm are separated by 179 pm, the high electron density produced by the laser plasma and subsequent avalanche ionization result in significant Stark broadening [71]. As a result, even in a low-pressure helium environment, the two lines are not fully resolved until 5.5 µs after the laser has been fired [70]. The study of $NaBD_4$ and $NaBH_4$ also used a long delay of 30 µs for line widths on the order of 150 pm, compared to instrumental broadening of 50 pm [71]. With deconvolution of curve peaks, the isotope ratio D/H could be calculated to 5% RSD.

In a more recent study, Doucet et al. [72] constructed a Partial Least-Squares (PLS1) model to analyze LIBS spectra for isotopic composition at atmospheric pressure. Although the ionic lines for ^{235}U at 424.437 nm and ^{238}U at 424.412 nm could not be resolved in the spectra, PLS1 was able to determine the concentration of 0.70, 3.0, 20, and 93% ^{235}U to 8, 6, 3, and 0.1% relative accuracy, respectively. Similarly, PLS1 predicted the concentration of 20% and 80% D_2O mixtures with H_2O to less than 7% accuracy in nine of the ten standards. Cremers et al. [59], however, achieve good resolution between the same ^{235}U and ^{238}U ionic lines simply by using an extremely long gate width of 20 µs for the ICCD. Although the peaks are resolved at 424.437 nm with zero gate delay, waiting 4 µs before triggering the ICCD allowed for reduced line widths and yielded an RSD of 9% for samples with 10, 30, 50, 70 and 90% ^{235}U.

1.4.4 Laser Ablation Molecular Isotopic Spectrometry (LAMIS)

As mentioned above, the isotopic shifts in the atomic and ionic lines of uranium and plutonium are on the order of picometers. The separation in the atomic lines of many other elements, such as boron, is even smaller, but shifts in the molecular emission of BO are considerably larger. In 1998, Niki et al. [73] proposed that emission from the $^{2}\Pi\,(v=0) \rightarrow {}^{2}\Sigma\,(v=2)$ band might reflect the isotopic composition of boron. The calculated spectra agreed very well with the observed emission, and it was estimated that the molecular spectra could be used to detect a 5% change in the natural abundance ratio.

Development of the technique, however, did not resume until 2011, when Russo et al. [62], who termed it Laser Ablation Molecular Isotopic Spectrometry (LAMIS), demonstrated the use of molecular emission to differentiate between $^{11}B^{16}O$ and $^{10}B^{16}O$, ^{16}OD and ^{16}OH, and $^{13}C^{14}N$ and $^{12}C^{14}N$. In the case of hydrogen and deuterium, the molecular shift was several times larger than the separation in the atomic lines, but the primary advantage arose from the fact that the molecular spectra, taken at later times and lower electron densities, experienced little Stark broadening. In addition, the molecular spectra are not typically observed until most of the continuum emission has disappeared [74]. Using the natural abundance as weighting factors in calculating emission intensities, simulated spectra were shown to closely match optical emission for not only the BO transition $B^{2}\Sigma^{+}\,(v=0) \rightarrow X^{2}\Sigma^{+}\,(v=2)$ from 255 to 259 nm [74] but also the SrO transitions $A^{1}\Sigma^{+}\,(v=2) \rightarrow X^{1}\Sigma^{+}\,(v=0)$ and $A^{1}\Sigma^{+}\,(v=1) \rightarrow X^{1}\Sigma^{+}\,(v=0)$ as well as the SrF transition $B^{2}\Sigma^{+}\,(v=1) \rightarrow X^{2}\Sigma^{+}\,(v=0)$ [75]. In addition, the molecular spectra of $^{10}B_{0.99}{}^{11}B_{0.01}O$, $^{10}B_{0.8}{}^{11}B_{0.2}O$, $^{10}B_{0.52}{}^{11}B_{0.48}O$, $^{10}B_{0.2}{}^{11}B_{0.8}O$, and $^{10}B_{0.05}{}^{11}B_{0.95}O$ between 579 and 585 nm were used as a library for a partial least squares (PLS) linear regression [74]. The PLS model yielded a ^{11}B fraction of 78 ±3.7% for an RSD of 5%, and this precision held even for spectra at much lower resolutions.

1.5 Motivation for the Study

When basic time-of-flight mass spectrometry on the ablation plume began to produce data along the lines of Fig. 1.1, the separation of isotopes in the laser plume immediately presented itself as an intriguing area of study. Not only were the results striking, with the proportion of the lighter isotope dropping from a half to a third based on a mass difference of only several percent, but they also held serious implications for isotopic characterization techniques based on laser ablation. If isotopes were indeed being separated within the laser plume, any method using ablation for solid sampling might be subject to this effect and it would be critical to minimize this separation in order to obtain accurate isotope ratios. Conversely, if it is possible to enhance separation in the plume, then the phenomena could be used to strengthen the signal of minor isotopes, such as ^{235}U in depleted uranium [64] or short-lived fission products [16], in order to improve the precision of the measurement. In both absorption [65] and fluorescence [64] studies, for example, evaluation of the isotope intensities is made considerably more difficult by the large disparity in the magnitude of the signal and the minor ^{235}U peak can even become hidden in the wing of an adjacent

^{238}U line. Probing a region of the plasma enriched in ^{235}U might be an effective way to counteract this issue. Finally, observing differences in the isotope distribution suggests a possible means of isotope separation, although being able to collect such particles efficiently and economically remains at least several steps away from detecting and describing the principle at work.

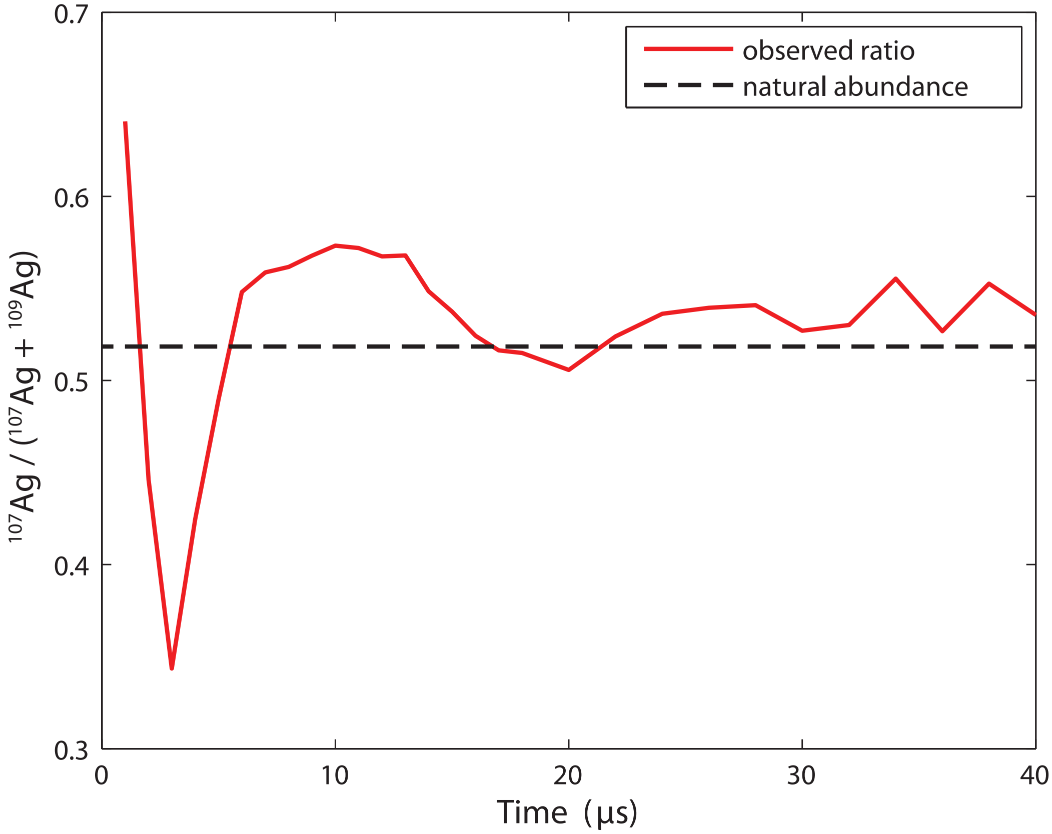

Fig. 1.1 The dramatic change in the ^{107}Ag abundance over time was highly unexpected, given that the mass difference between the two isotopes amounted to only a couple percent. Separation of isotopes in the laser plume has significant implications for any isotopic characterization technique using laser ablation for solid sampling.

1.6 Isotope Separation in the Laser Plume

Isotope separation due to laser ablation has been reported by only three groups thus far, each under different ablation conditions and using different methods of detection. All three groups performed studies on both the laser plume and the deposited film, with the film showing significantly less deviation from the natural abundance.

In 1980, Gupta et al. [76] ablated boron oxide targets at 10^{-5} Torr with a Nd:glass laser at 600 mJ for a fluence of 2000 J/cm^2 or an irrandiance of 60 GW/cm^2. The flight tube of a time-of-flight was placed at an angle to the sample and coupled to an electrostatic analyzer to obtain isotope intensities by kinetic energy. The energy distributions for ^{10}B and ^{11}B peaked at 640 and 700 eV respectively, as expected from hydrodynamic expansion. The ion intensities, however, were heavily skewed in favor of the lighter isotope, with a ^{10}B/^{11}B ratio of 1.3 in the energy range of 600 to 900 eV and around 1.7 at the ^{10}B peak of 640 eV, compared to a natural abundance of 0.245 in the original sample. A substrate was placed behind a 500 V grid 30° from the target normal in order to collect ions from the plume, but analysis of the deposited film revealed a ^{10}B/^{11}B ratio of only 0.277 ± 0.006, 10% above the natural abundance. The more modest change in the isotope ratio of the film is attributed to the presence of neutrals in the plume, which have a relatively even isotope distribution and were not repelled by the electrostatic grid. The enrichment of ^{10}B in the mass analyzer, on the other hand, was observed specifically for singly-charged ions.

Almost two decades later, Pronko et al. [77] observed isotope separation in laser ablation of BN and GaN with a 780-nm femtosecond laser at a fluence of 50 J/cm^2 and an irradiance of 2.5×10^{14} W/cm^2. A sector-field electrostatic analyzer perpendicular to the sample surface was used to detect the ions. Highly charged states of boron included a much larger fraction of ^{10}B than the natural abundance of 19.78%, and the +3 and +4 charge states showed almost as much ^{10}B as ^{11}B when the electrostatic analyzer was set at 1 keV. Even when the chamber was backfilled with 8×10^{-4} Torr nitrogen was used, there was still substantially more ^{10}B compared to the natural abundance ratio, although the charge states were greatly reduced. Film deposited on a subtrate 7 cm in front of the sample confirmed that the plume center had a significantly higher proportion of ^{10}B than the edge of the plume. Rutherford backscattering (RBS) of the boron film revealed a ^{10}B/^{11}B ratio of 0.45 near the center compared to 0.29 ±0.02 at the edge. A centrifuge mechanism based on transient magnetic fields in the laser plasma was proposed, but this explanation was difficult to justify based on the measurements obtained and was regarded as unnecessarily complicated [78]. A later study produced similar results from ablation of GaN, titanium, zinc, and copper, showing enrichment of the lighter isotope at higher levels of ionization [79]. Isotope separation was also achieved at lower fluences and using a nanosecond laser, although the effect was significantly diminished for nanosecond ablation in the ultraviolet with an irradiance of 4 GW/cm^2.

Joseph and Manoravi, however, measured a ^{10}B/^{11}B ratio of 0.9, compared to the natural abundance of 0.25, using a Nd:YAG at 532 nm with a fluence of 6.4 J/cm^2 and an irradiance of only 800 MW/cm^2 on a B_4C target. In contrast to the previous studies, a quadrupole mass spectrometer was mounted 56 cm away from the sample, parallel to the sample surface and orthogonal to the direction of the plume. Lowering the irradiance to below 420 MW/cm^2, by overfocusing the lens to produce a larger spot size, brought the isotope ratio back down to the natural abundance. Sampling the plume off-axis by placing a 30°wedge under the sample also tended to reduce the skew in the isotope ratio. The same group deposited thin films of B_4C with a nanosecond laser at an irradiance of 800 MW/cm^2 and with a picosecond laser at an irradiance of 330 GW/cm^2. SIMS analysis of the films showed a small but measurable decrease in the ^{10}B/^{11}B ratio from 0.29 at the center of the film to 0.26 at a distance of 35 mm for deposition using the picosecond laser. With the nanosecond laser, on the other hand, the isotope ratio remained fairly constant at around 0.26, which was attributed to large particles in the deposited film.

1.6.1 Space Charge Effects

There exists considerable literature concerning the effects of space charge on ion sampling in the ICP-MS [44, 47]. Although this effect is used to describe ions from the inductively coupled plasma, laser ablation similarly involves a high density of charged ions expanding under vacuum, albeit in a pulsed process rather than as a continuous stream. Thus, the description of this phenomenon, while not completely analogous, may be helpful in explaining isotope separation in the laser plume.

Mass discrimination during ICP-MS was first reported by Tan and Horlick [80], who observed that the sample signal in the mass spectrometer could become suppressed by a high concentration of matrix elements. Heavy matrix elements typically caused a greater degree of analyte suppression, while lighter sample ions tended to be more affected by this process than heavier ones [80, 81]. This matrix effect, the crowding out of lighter analytes by matrix ions, has been attributed to space charge from the plasma selectively repelling the lighter ions off-axis as they enter the skimmer and interact with the ion optics [81, 82]. Gillison et al. [81] performed simulations showing that not only do lighter ion distributions become defocused about the instrument axis once space charge is taken into account, but the presence of only 0.1 to 1% of a heavy matrix element is enough to cause the ion trajectories to defocus. Further calculations [82] confirmed that higher ion currents lead to greater deflection off-axis and preferentially higher transmission of heavier isotopes through the system. Experimental results demonstrated that the presence of heavy elements in the matrix increased both the temporal [83] and spatial [84] spread of lighter ions, although this mass discrimination could be reduced by increasing the voltage potential of the ion optics.

1.7 Organization of Thesis

The rest of this thesis consists of four chapters. Chapter 2 describes the equipment and procedures used to run the experiments. The instrumentation for ablating the sample and then performing mass spectrometry on the ablation plume is detailed in Sec. 2.1, and Sec. 2.2 describes how the time-of-flight traces are processed to provide temporal and spatial profiles. Sec. 2.2.1 explains the upper limit on the number of shots per location and how this affects the choice of laser fluence. Sec. 2.2.2 describes the largest known source of systematic error in this study as well as a failed attempt to correct for this extraneous signal. Sec. 2.3 explains how the beam was aligned to the sample and the sample to the entrance of the mass spectrometer, and includes calculations of the spot size in Sec. 2.3.1. The effect of the repeller geometry and, specifically, changes that were made to ensure a linear electric field between the repellers are described in Sec. 2.4.

The time-of-flight mass spectrometer allowed many parameters to be adjusted, but it was difficult to tune these variables properly without computational simulations of the instrument. Chapter 3 explains the physical significance of these parameters and describes the optimization of voltages within the system. Sec. 3.1 focuses on the electrodes that guide the ions from the repellers to the detector. Sec. 3.1.1 explains an instrumental limit on the forward velocity of accessible ions, while Sec. 3.1.2 and Sec. 3.1.3 describe optimization of electrode voltages to direct and compress the ion distribution, respectively. Sec. 3.2 provides a detailed account of how the reflectron is used to both compress the ion time-of-flight and serve as an energy filter. Sec. 3.2.1 describes a fundamental limit on the mass resolution of a time-of-flight system. Sec. 3.2.2 explains how the potential energy of an ion can be correlated to its position between the repellers, and Sec. 3.2.3 explains how the reflectron includes both potential and kinetic energy in determining which ions are able to reach the detector. Sec. 3.2.4 describes how to determine the time-of-flight for a given ion distribution and how that calculation is used to optimize the reflectron voltages. The section concludes with implications for the ion position and velocity based on observed time-of-flight traces.

The results are presented in Chapter 4. Full spatial and temporal profiles of the isotope content were obtained for the experiments in Sec. 4.1. The mass spectrometer was initially configured to collect ions from the entire plume in Sec. 4.1.1, but the isotope separation observed suggested that it might be helpful to focus on specific regions of the plume. Parameters limiting ion detection to the center of the plume were used in Sec. 4.1.2 and those limiting ion detection to the side of the plume in Sec. 4.1.3. A direct comparison with data from the entire plume was difficult due to the early ions, described in Sec. 4.1.4, but the results showed little isotope separation when sampling the plume center and the plume side. Sec. 4.1.5 proposes an explanation for this discrepancy. To locate the region with the greatest isotope separation, several different schemes were used to sample specific windows over the laser plume. The sampling window was widened from the center in Sec. 4.2.1, widened from the side in Sec. 4.2.2, and scanned across the width of the plume in Sec. 4.2.3. The results revealed the greatest isotope separation when the system was configured for ions on the far side of the plume, and full spatial and temporal profiles were obtained in Sec. 4.3.

Chapter 5 summarizes the major accomplishments of this project, specifically, the development and validation of the time-of-flight instrument in Sec. 5.1 and characterization of isotope separation during laser ablation in Sec. 5.2. Potential directions for future work are provided in Sec. 5.3, with an emphasis on developing the current instrumentation in Sec. 5.3.1, interrogating the plume with atomic absorption spectrometry in Sec. 5.3.2, and using this time-of-flight system to study chemical reactions during laser ablation in Sec. 5.3.3.

Chapter 2

Experimental Setup

Orthogonal-acceleration time-of-flight mass spectrometry was used to measure the isotope content of the ions generated in the laser plume during ablation. Measurements were obtained at different locations within the plume by adjusting the position of the sample relative to the mass spectrometer and at different points in time by varying the delay between the laser pulse and the high voltage repellers.

Over the course of conducting the experiments, extensive calibration procedures were developed and implemented to ensure shot-to-shot consistency, to align the laser beam with the lens and the sample, and to maintain the spot size of the beam. These methods were used to validate the repeatability and consistency of each measurement.

In addition, the repeller geometry was modified from an ion trap to flat plate electrodes in order to allow measurements to be taken at different distances from the target surface. Changing the geometry, however, also reversed the isotopic composition measured in the plume. The electric field of the repellers was modeled in order to verify that the ions sampled in each trial corresponded to the intended region within the plume.

2.1 Instrumentation

The experimental setup, shown in Fig. 2.1, was designed for mass spectrometry of laser ablation on a solid sample in vacuum. The system was a modified version of the laser ablation ion-storage time-of-flight instrument described in Russo et al. [85] and Klunder et al. [86], which was based on the ion-storage time-of-flight system in Chambers et al. [87]. Although the ion trap (Finnigan MAT) was kept in place for the initial measurements, it was replaced by flat-plate repeller electrodes in order to to allow movement of the sample and to establish a linear electric field, as will be described in Sec. 2.4.

A Nd:YAG laser frequency-tripled to 355 nm (Quantel, Brilliant) was used to generate 50 µJ laser pulses with a 5 ns duration. The laser energy was measured by a pyroelectric

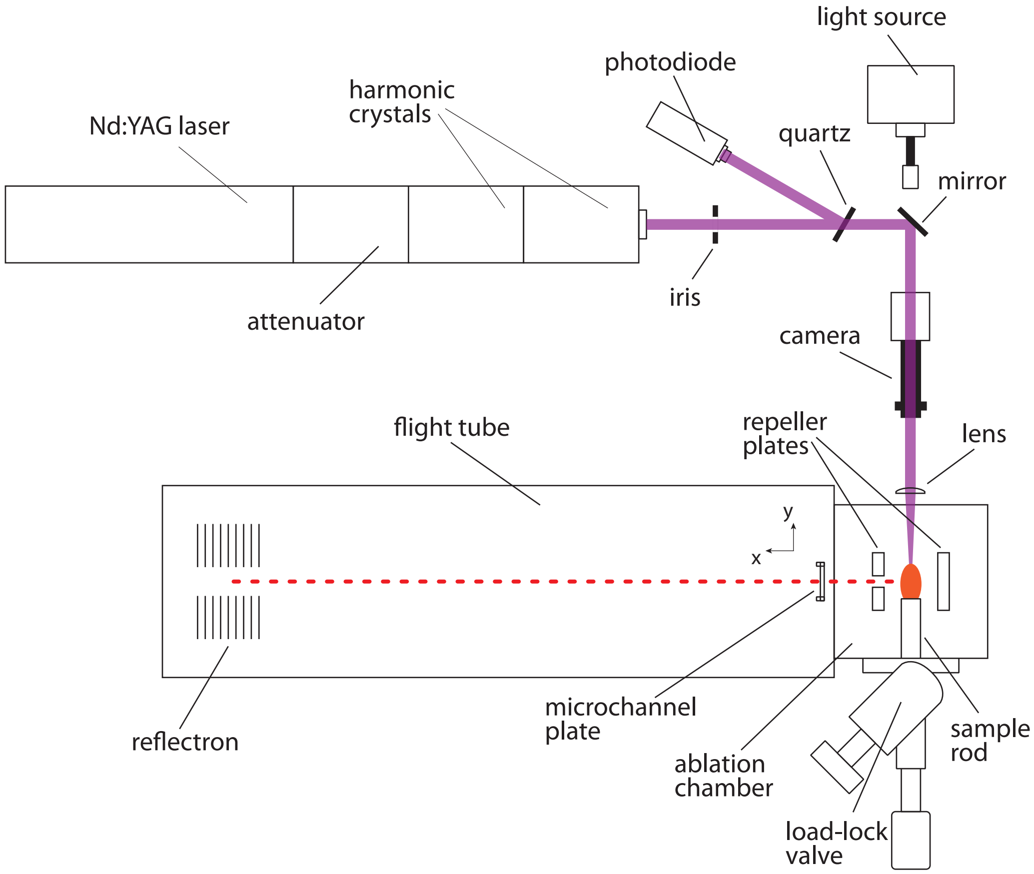

Fig. 2.1 The laser beam from a Nd:YAG nanosecond laser is focused by a fused silica lens into the ablation chamber, generating an ion plume that was examined using mass spectrometry. The repeller plates pulse the ions into the flight tube, where their trajectory is reversed by the reflectron before they finally register at the microchannel plate. Although not apparent from the overhead view in this diagram, the ion path curves downward from the plume to the reflectron to the microchannel plate. Similarly, the camera is positioned physically below the laser beam and lens, while the light source is in line with the beam and illuminates the sample through the lens.

energy probe (Molectron, J4-09-070) before each run and correlated to readings from a photodiode (Thorlabs), which was used to to monitor the energy stability during the actual experiments. The laser beam was focused through a plano-convex fused silica lens (CVI, PLCX-12.7-41.2-UV) to a spot size of roughly 71 µm during ablation. Although copper foil (Alfa Aesar, 0.127 mm, 99.9%) was used during initial testing and gold foil (Alfa Aesar, 0.1 mm, 99.95%) was used to validate the instrument response, the bulk of the experiments were conducted using silver foil (Alfa Aesar, 0.127 mm, 99.9%), because its two stable isotopes are evenly distributed. The isotopic composition of silver is 51.84% ^{107}Ag and 48.16% ^{109}Ag [88].

Laser ablation was observed from a camera (JAI, CV-S3200) coupled to a microscope objective lens (Edmund Optics), and the sample was illuminated using a fiber optic light source (Dolan-Jenner, MI-152). Once the sample was removed from the ablation chamber, the craters produced were measured using a microscope (Olympus, BX51) and the images recorded on a USB camera (IDS, UI-1485LE-C-HQ).

Mass spectrometry was performed using an angular reflectron time-of-flight system (R.M. Jordan, D-850) equipped with a 40-mm dual microchannel plate detector (R. M. Jordan, C-726). All of the voltage potentials within the flight tube were provided by the accompanying power supply (R. M. Jordan, D-803) except for the R2 back reflectron voltage, which was connected to a separate 5 kV DC power supply (Stanford Research Systems, PS350). Voltage potentials to the two repeller plates in the ablation chamber were provided by a pair of 3 kV power supplies (Bertan, 825-3N/P), with switching controlled by a high voltage MOSFET push-pull switch (Behlke, HTS 31-GSM) for each repeller. A 1.5 mm hole in the one of the repeller plates allowed ions to enter the mass spectrometer, and the other plate was completely solid.

There was a 10.16 mm hole between the ablation chamber and the flight tube for differential pumping, since the ion trap was originally designed to allow a cooling gas into the system during ablation of the sample. The pressure of both chambers, nevertheless, was maintained at below 3×10^{-6} mbar for all of the experiments by a pair of turbomolecular pumps (Pfeiffer Balzers, TPU/H 180H), each regulated by a turbopump controller (Pfeiffer Balzers, TCP 380) and both backed by a single rotary vane roughing pump (Alcatel, Pascal). The vacuum pressure in each chamber was monitored by a cold cathode gauge (Pfeiffer Balzers, IKR 020) connected to a common two-channel pressure controller (Pfeiffer Balzers, TPG 300). Sample exchange was provided by a custom load-lock system based on a manual poppet valve (Nor-Cal), and the pressure during sample transfer was monitored by a combined Pirani and piezoelectric pressure sensor (MKS, 901P Loadlock Transducer).

A digital delay generator (Stanford Research Systems, DG645) was used to fire the laser q-switch and to trigger the oscilloscope and the high-voltage repellers in the ablation chamber. Voltage traces from the detector, as well as the laser energy and photodiode readings, were recorded on a four-channel digital oscilloscope (Tektronix, DPO3054), and both the delay generator and the oscilloscope were connected to a laptop computer via ethernet to synchronize data acquisition.

2.2 Data Collection

In a typical trial, the laser is fired and, after a delay of 0 to 50 µs, a voltage potential is applied to the repeller plates, pulsing the ions into the flight tube. At the same time, the oscilloscope is triggered and starts recording the voltage at the microchannel plate. Fig. 2.2 contains a diagram of the timing, and a sample trace with a delay time of 20 µs is shown in Fig. 2.3. Since silver was being measured in these experiments, the area under the peaks in Fig. 2.3 corresponds to the number of ^{107}Ag and ^{109}Ag ions collected from the plume 20 µs after the laser pulse. On the x-axis of this plot is time-of-flight, which is used to distinguish the isotopes in the mass spectrometer. Given similar initial kinetic energies, heavier isotopes will take longer to traverse the flight tube and have longer times-of-flight than lighter isotopes. This will be discussed in greater detail in Sec. 3.2.4. It is important to note that the time-of-flight variable, used primarily in the individual mass spectrometry measurements, is different from the delay time, which relates to development of the ablation plume and is one of the key parameters of this study.

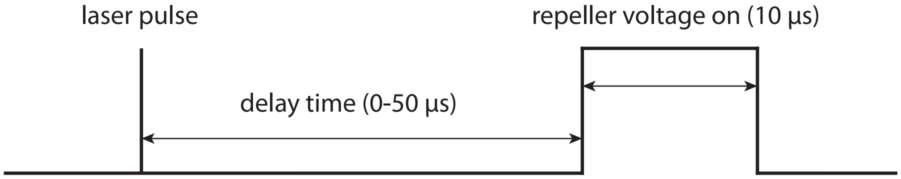

Fig. 2.2 After the laser is fired, a brief period of time is allowed to elapse before the high-voltage repellers are turned on. The oscilloscope is also triggered at the end of this delay interval. By adjusting the delay between the laser pulse and the repellers, a temporal profile of the plume can be obtained.

Varying the delay between the laser pulse and the high-voltage repellers in Fig. 2.2 allows the laser plume to be sampled at different points in time. By measuring the isotopes in the plume at different delays, the temporal profile of the plume can be reconstructed, as shown in Fig. 2.4. In this case, the x-axis represents delay time, the interval over which the plume is allowed to develop unperturbed before being sampled by the mass spectrometer. Each of the points on the blue and green lines represents integrated areas from the ^{107}Ag and ^{109}Ag peaks respectively in the original oscilloscope traces. The ^{107}Ag and ^{109}Ag content derived from the trace in Fig. 2.3, for example, is mapped onto the blue and green lines at 20 µs in Fig. 2.4. The red line in Fig. 2.4 represents the fraction of ^{107}Ag relative to the total number of silver ions in the plume measured at that specific time. This study uses the fraction of the lighter isotope rather than the isotope ratio, because the concentration of both isotopes may be changing, so neither serves as a suitable reference. In addition, the ^{107}Ag fraction avoids overstating the change in the isotopic composition when it becomes heavily

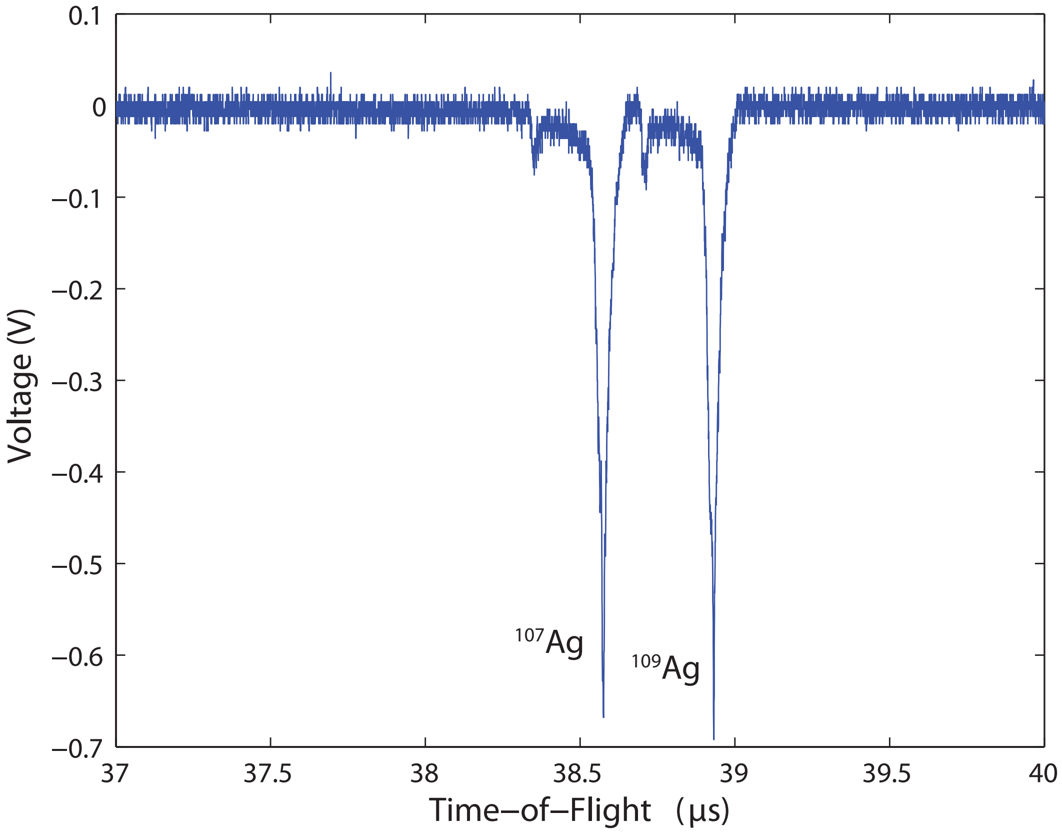

Fig. 2.3 This sample trace at a delay time of 20 μs includes peaks from the two isotopes of silver: ^{107}Ag and ^{109}Ag. The time-of-flight on the x-axis starts when the repellers are pulsed, and the position of the peaks can shift with the position and velocity of the ion distributions, as will be discussed in Sec. 3.2.4. The area under the peaks is integrated in order to obtain the isotope content in the plume.

skewed in either direction. The two terms, however, will be used almost interchangably to refer to the proportion of one isotope relative to the other.

Not all of the ions in the ablation plume, however, are able to make it to the detector. Because the hole in the repeller plate is only 1.5 mm in diameter, only those directly in front of the hole can enter the mass spectrometer, as shown in Fig. 2.5. The rest will collide with the repeller plate once the high voltage potential is applied. As a result, the isotope intensities reported in Fig. 2.4 represent only a small slice of the plume 10 mm away from the target. Moving the sample in the y direction closer and farther away from the hole in the repeller plate, as shown in Fig. 2.5, allows the mass spectrometer to sample different parts of the laser plume, namely, those closer and farther away from the target surface.

By measuring the isotope content at different locations in the plume, a spatial profile can be reconstructed, as shown in Fig. 2.6. In this case, the delay time is held constant at 6 μs after the laser has fired been, while the distance between the part of the plume being

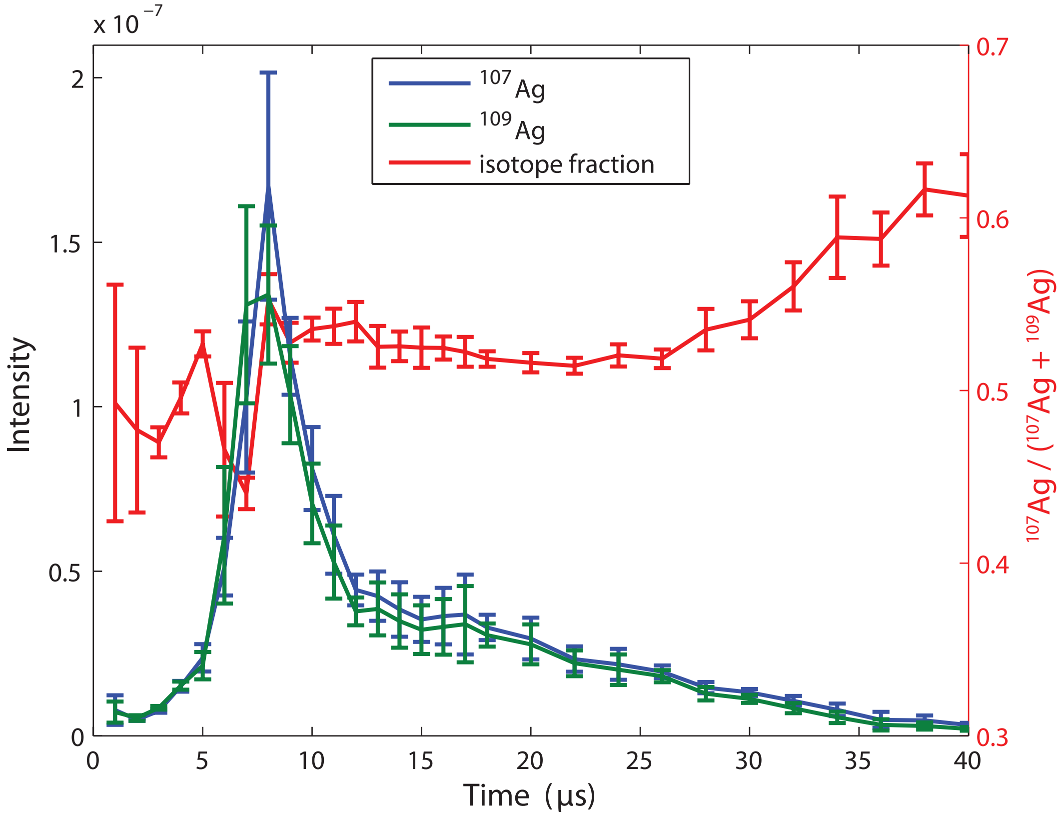

Fig. 2.4 This is a typical plot of isotope content against time and represents the temporal profile of the isotopes measured in one part of the laser plume. The x-axis corresponds to the delay time between the laser pulse and ejection of the plume by the high-voltage repellers in Fig. 2.2. In this case, the sample is at a distance of 10 mm. Very few ions can be observed at early times, because the plume has not yet reached the entrance to the mass spectrometer. At later times, the plume slowly dissipates and the intensity decreases.

measured and the target surface is scanned from 0 to 16 mm. As before, the intensities displayed were obtained by integrating the isotope peaks in oscilloscope traces taken at each of these different locations, with every set of points on the graph representing peak areas from an individual trace.

If all of the particles in the ablation plume moved at the same constant velocity, the temporal and spatial profiles in Figs. 2.4 and 2.6 would simply differ by a factor of that velocity. Collisions in the plume and hydrodynamic expansion into vacuum, however, invalidate this premise. Thus, in order to capture fully the development of the plume, it is helpful to vary both delay time and distance, which provides a frame-by-frame depiction of the different isotope distributions as the plume propagates through space and time.

For the rapid measurements in Sec. 4.2, however, the distance is often kept constant while only time is varied. Because the sample is not mounted on a stage, sample manip-

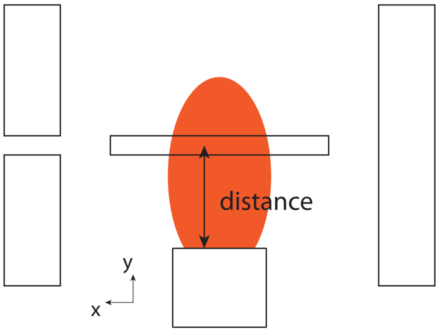

Fig. 2.5 Each time high voltage is applied to the repeller plates, the ions are accelerated in the x direction, toward the flight tube. Because the hole is only 1.5 mm in diameter, however, only the thin cylinder of ions enclosed by the rectangle make it into the mass spectrometer and are able to be measured. By moving the sample in the y direction and changing the distance between the sample and the hole, different parts of the plume can be interrogated. Plotting these intensities against distance gives the spatial profile of the plume in Fig. 2.6.

ulation is cumbersome and the position of the sample can only be established by visually observing whether the camera is in focus. The delay time, in contrast, can be changed quickly, accurately, and automatically using the delay generator. Because the temporal profiles are much easier to obtain and maintain more consistent ablation conditions from one trial to the next, they will be given greater precendence in the results and can generally be considered a very rough proxy for spatial information.

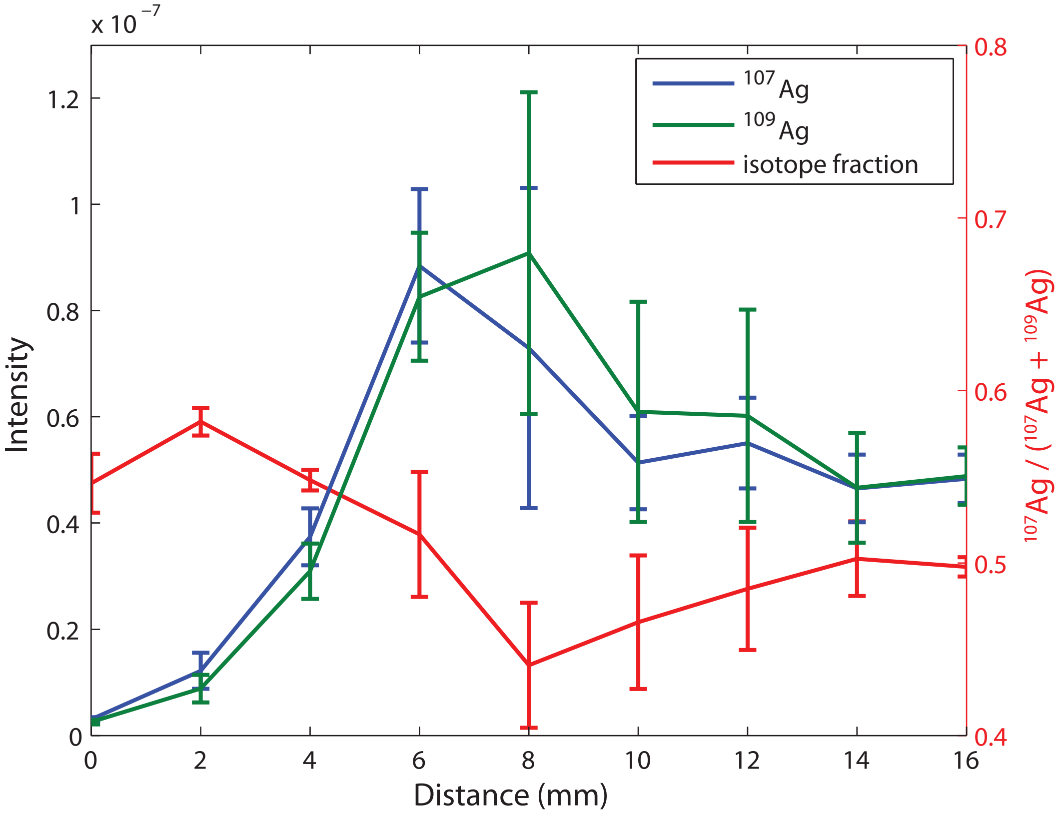

Fig. 2.6 The spatial profile can be obtained by changing the distance between the target and the entrace to the mass spectrometer, as shown in Fig. 2.5. Keeping the delay constant while varying the distance provides a snapshot of the laser plume at a single time, in this case 6 μs. Plotting the isotope content in the plume against distance instead of time gives a more physically intuitive representation of how the ions in the laser plume are propagating, but scanning along this dimension tends to be more involved and less accurate than varying the delay time.

2.2.1 *Shot-to-Shot Consistency*

There is a significant amount of uncertainty in these measurements, as is apparent from the large error bars on some of the points in Figs. 2.4 and 2.6. Most of this uncertainty stems from the large variation in the laser energy, which typically had a standard deviation of around 15% or 7.5 μJ for a 50 μJ shot. The relative standard deviation could have been reduced at higher energies, but this would have come at the expense of degrading the sample surface, the other major source of uncertainty in these measurements. Since each laser pulse literally vaporizes a small portion of the sample, a crater forms at the surface and deepens with each subsequent shot in the same location. To minimize alterations of the sample surface, which has a significant effect on the ablation dynamics, the laser fluence was set as low as possible while still allowing for a reasonable signal intensity. A low laser energy was also helpful in avoiding saturation of the detector.

Since roughly 50 different delays were needed to cover the temporal profile of the plume, the fluence was chosen such that 50 to 100 shots could be fired at a single spot without substantial degradation of the signal. This was tested by firing 100 shots at the same spot with the same delay for several different delay times. Fig. 2.7 shows the isotope content in consistency tests with a spot size of 50 µm, or a fluence of 2.5 J/cm^2. At 5 µs in Fig. 2.7(a), the ^{107}Ag fraction drops steadily until 60 shots while the isotope intensities rise haphazardly after that. At 16 µs in Fig. 2.7(b), the ^{107}Ag fraction remains fairly constant, but the individual ion intensities decrease from the start and do not settle until after 60 shots. Neither plot demonstrates the needed consistency.

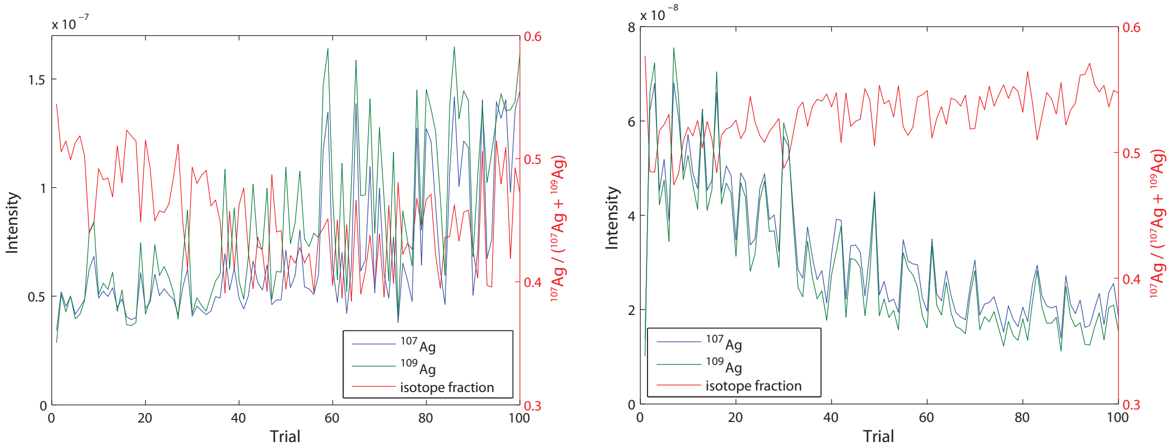

(a) Consistency at a delay of 5 µs.

(b) Consistency at a delay of 12 µs.

Fig. 2.7 Isotope intensities and ratios were measured over 100 shots fired at a single spot. The ablation diameter was 50 µm, for a fluence of 2.5 J/cm^2. The decrease in the ^{107}Ag fraction at 5 µs (a) and in the ion intensities at 12 µs (a) over the first 60 shots suggests that a deepening crater may be degrading the measurement consistency and that a lower fluence should be used.

To maintain a higher degree of repeatability, the area irradiated was doubled to a diameter of 71 µm, or a fluence of 1.3 J/cm^2. The isotope content over 100 shots at two delays is shown in Fig. 2.8. While the variation in Fig. 2.8(a) at 6 µs is fairly large, the range of fluctuation remains relatively constant for both the ion intensities and the isotope ratio. The intensities do decrease slightly after 60 shots in Fig. 2.8(b) at 12 µs, but the ^{107}Ag fraction stays roughly the same over the course of the test. Because of the change in the ion intensities, however, most of the experiments fired less than 60 shots before moving to a fresh surface. In addition, based on Figs. 2.7 and 2.8 the first couple shots tended to be less representative of the average composition and were discarded before the measurements were started.

Note also that in the temporal and spatial profiles as well as the consistency measurements, the relative uncertainty in the ^{107}Ag fraction is often less than that of the isotope

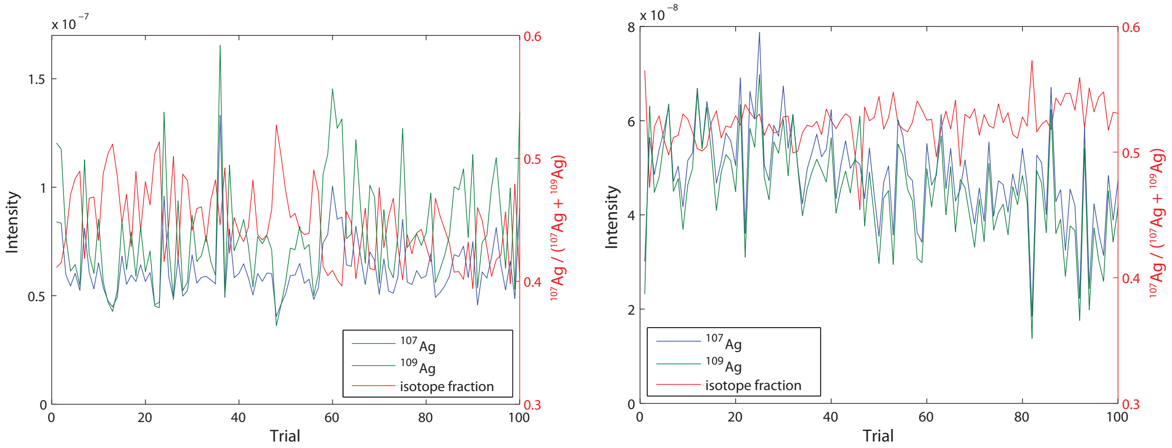

(a) Consistency at a delay of 6 µs.

(b) Consistency at a delay of 12 µs.

Fig. 2.8 Consistency tests, with 100 shots to the same spot, were performed for a spot diameter of 71 µm, or a fluence of 1.3 J/cm^2. Although there is a large degree of variation in both the intensities and the ^{107}Ag fraction at 6 µs (a), the average values do not change significantly over the course of 100 shots. The ion intensities decrease slightly after 60 shots at 12 µs (b), so most experiments took no more than 60 measurements at a single location.

intensities themselves. This is especially true in Fig. 2.8(b) at 12 µs. Although there may be a large degree of variation in the number of individual ions measured from shot to shot, the ratio between the two isotopes generally stays within a much smaller range.

2.2.2 *Early Ions*

The extra ions registered by the oscilloscope at early times are one of the most important disadvantages of performing laser ablation in this instrument and present the greatest source of systematic error in this study. As shown in the voltage traces of Fig. 4.9, there is a significant amount of undesired signal that is recorded just before the peaks from the ejected ions. This is especially a problem at relatively early delays, where the signal can overlap with the peaks of interest and distort the calculated isotope ratio.

Because the extraneous voltage always appears just microseconds ahead of the desired ions in the time-of-flight, the extraneous signal is most likely the result of additional silver ions arriving at the microchannel plate. Since ions must be brought back by the reflectron before they can reach the detector, it would be very difficult for a particle to be recorded unless it has traversed the path shown in Fig. 2.1. Furthermore, if the ion has taken that path and reaches the detector near the same time as the silver being measured, it must have a mass close to that of silver or be a silver ion itself. In addition, as shown in Fig. 4.9, the timing of these ions is synchronized with the laser pulse. If there is 2 µs between the laser and the repeller pulse, as in Fig. 2.9(a), the early ions appear just under 2 µs before the pulsed ions. If the delay is 3 μs, as in Fig. 2.9(b), the interval between the two ion packets is just under 3 μs.

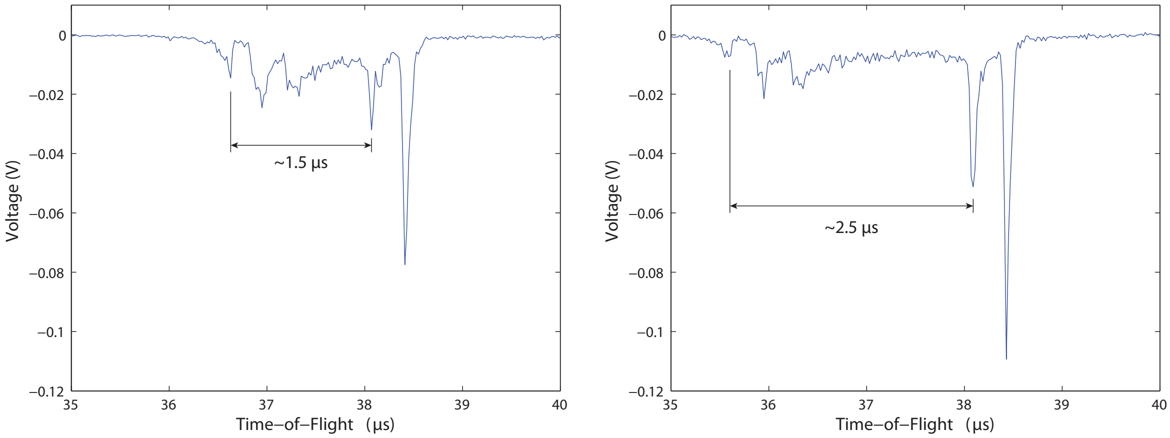

(a) Voltage trace at a delay of 2 μs.

(b) Voltage trace at a delay of 3 μs.

Fig. 2.9 Ions in the laser plume that enter the mass spectrometer even before the repeller plates have been pulsed are responsible for the extraneous signal before the peaks of interest. These undesired early ions can overlap with the isotope peaks and distort the isotope ratio. Note that a time average of 50 points has been used in these plots for the sake of clarity.

This suggests that the undesired signal is the result of ions that enter the mass spectrometer early, even before the repeller plates have been turned on. The early ions described here correspond to the untrapped ions in Klunder et al. [86], which are synchronized to the laser pulse instead of the endcaps. Since the liner in the flight tube is at -1300 V, these ions quickly gather speed after entering the mass spectrometer, allowing them to reach the microchannel plates just ahead of the pulsed ions. When the pulser is off, the trace does indeed resemble the early signal in Fig. 2.9(b), except that the voltage slowly tapers off instead of terminating in the two sharp isotope peaks. In Fig. 2.9(b), however, the voltage goes to zero immediately after the pulsed ions, because, in addition to pushing the desired cross-section of ions into the flight tube, the repellers also cause the rest of the plume to collide with the solid part of repeller plate. Therefore, the extraneous signal consists of ions in the plume that are capable of entering the mass spectrometer without the electric field, and includes only those before the high voltage is applied to the repeller plates and the entire plume is accelerated toward the flight tube.

The peaks near the beginning of the early ion signal are due to the initial burst of ions almost immediately after the laser pulse. Because the fastest of these ions originate within a single burst, they can be separated by mass within the reflectron system to some extent. The peak structure at the beginning of the signal is due to different isotopes in the plume having different times-of-flight within the mass spectrometer, but the high velocity of the ions at these early times prevents the reflectron from forming sharp peaks the same way it does with the pulsed ions.

Since these early ions distort the signal and can change the integrated area under the isotope peaks, an attempt was made to prevent them from reaching the detector. If the deflector plates were turned on after the repellers, the early ions would fail to be deflected down toward the microchannel plate while the pulsed ions could still pass through a little later. Thus, instead of keeping the deflectors on all the time, they were also pulsed, using the timing in Fig. 2.10. Before the repeller pulse and during the deflector delay, the bottom deflector (XY1) was kept at 0 V, which accelerates the ions toward the top of the flight tube and away from the microchannel plate. After the deflector delay, the bottom deflector (XY1) was pulsed to its normal operating voltage of -1300 V, directing the ions from the repeller toward the microchannel plate.

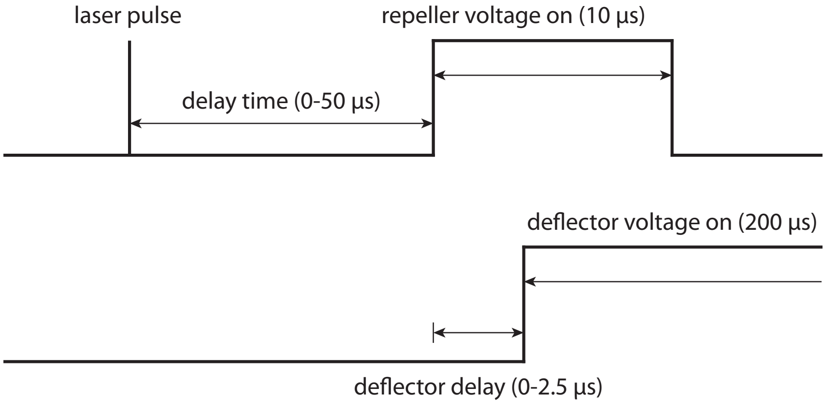

Fig. 2.10 An attempt was made to eliminate the early ions from the voltage trace by delaying the deflectors until after the repeller pulse instead of keeping them always on. Applying a voltage to the deflectors right before the pulsed ions entered the mass spectrometer would force the early ions onto a different trajectory while still allowing the pulsed ions to reach the detector.

Pulsing the voltage on the deflector, however, had some unintended consequences. First of all, it was difficult to determine how long to set the deflector delay to allow all the pulsed ions through. More importantly, though, it turned out that varying the deflector timing had its own effect on the isotope ratio. As shown in Fig. 2.11, increasing the deflector delay from 0.8 µs to 1.4 µs causes the fraction of ^{107}Ag to jump from 0.22 to 0.48. Note that this effect is the opposite of what should be expected from eliminating the early ions. The undesired signal tends to overlap more with the lighter isotope, which arrives at an earlier time-of-flight, so removing the early ions should lead to a decrease in the ^{107}Ag content.

At the beginning, using a long deflector delay seemed to be producing better results, judging from the lower levels of uncertainty in the ^{107}Ag fraction in Fig. 2.11 and the well-defined traces in Fig. 2.12. In addition, the isotope fraction measured was much closer to the natural abundance ratio, even if the observed effect ran counter to what was expected with regard to removing the early ions. The timing of the later traces in Fig. 2.12, however,

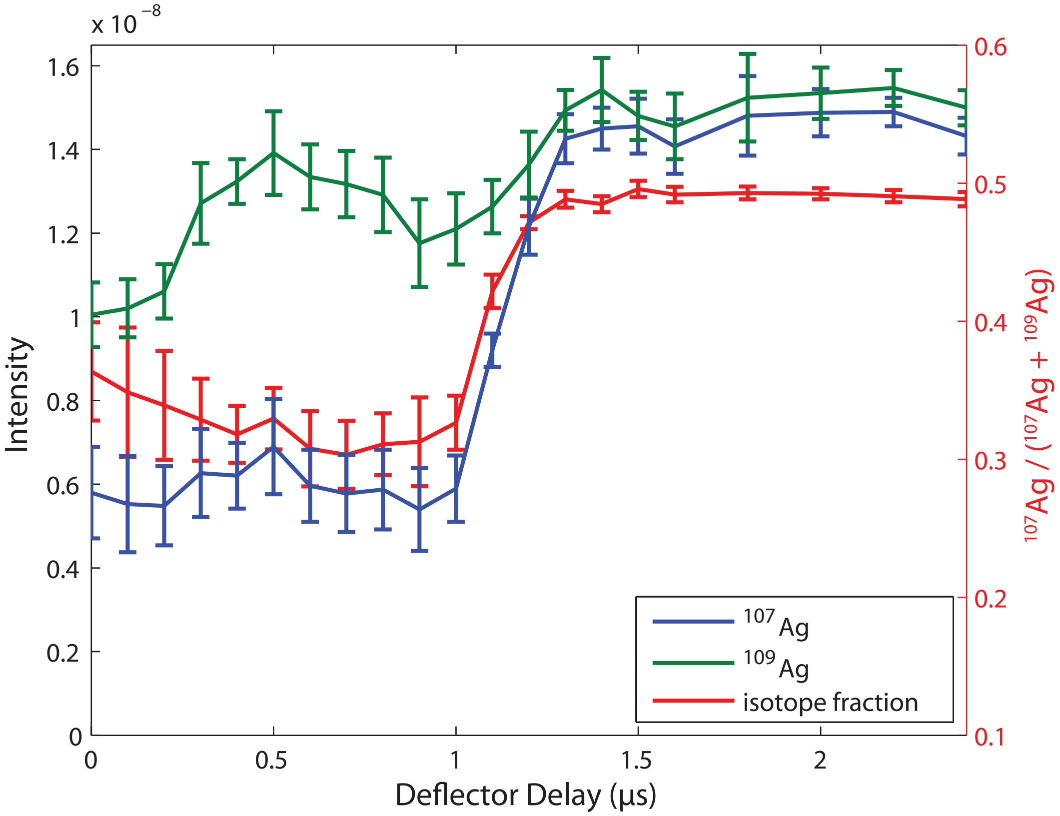

Fig. 2.11 Changing the deflector delay affected the isotope ratio, but not as anticipated. Removing the early ion interferences should lead to a slight decrease in the concentration of ^{107}Ag, which has an earlier time-of-flight, but instead the proportion of ^{107}Ag increases drastically after a deflector delay of 1 μs.

was highly suspect. If the deflector delay was set to 1.4 μs or later, the oscilloscope traces were shifted to the right by a corresponding time interval. That is, the isotope peaks had become synchronized to the deflector pulse rather than the repeller pulse. Instead of just serving as a gate, the deflector was acting as its own pulser and shunting an entirely different group of ions toward the detector. This was especially problematic, because these ions appeared to have an isotopic content different from that of the original plume slice.

The fact that the timing of the isotope peaks in the voltage traces could be shifted so much later suggested that a different population of ions was making it to the microchannel plate when the deflector delay was longer than 1 μs. It is not clear where in the plume these ions originated, but, if pulsing the deflector allowed them to reach the microchannel plate, their trajectory is likely to be very far off-axis from the path of the pulsed ions that were originally intended to be measured. The appearance of sharp peaks when pulsing the deflector at later times also indicates that many of the ions that enter the mass spectrometer never make it to the detector. Nevertheless, it is difficult to use measurements from these

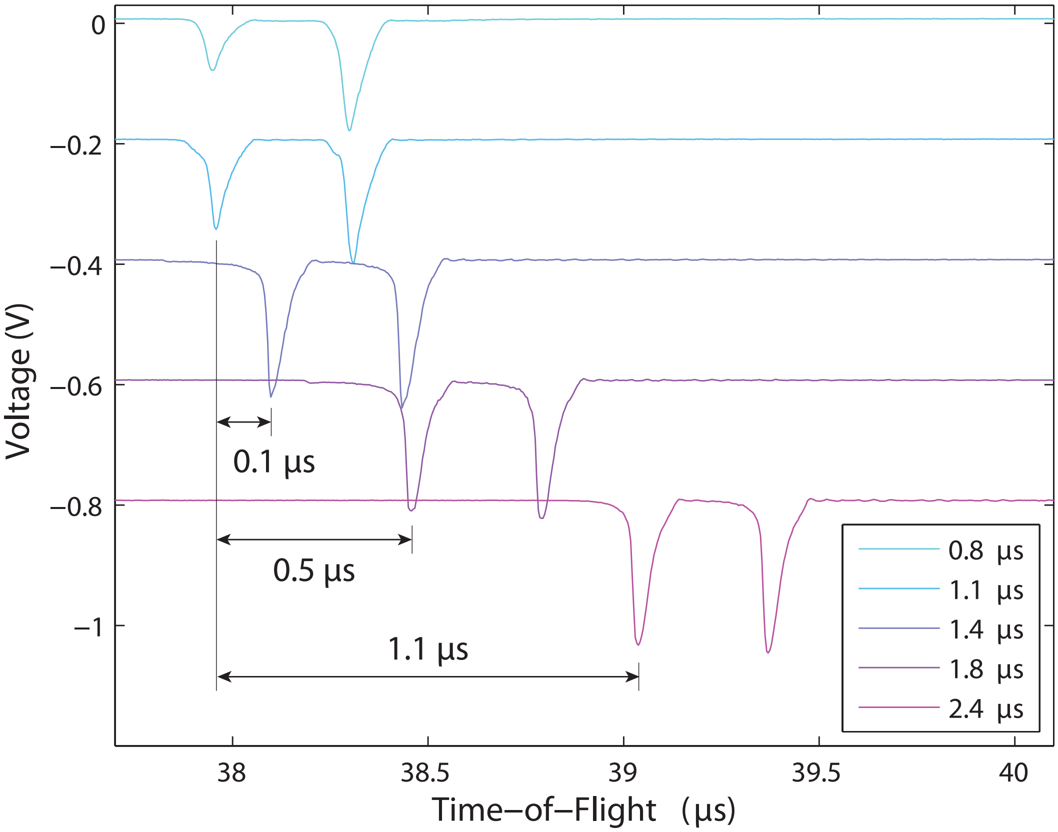

Fig. 2.12 Voltage traces for deflector delays of 0.8, 1.1, 1.4, 1.8, and 2.4 µs. Although increasing the deflector delay produced traces with sharp peaks and high intensities, the change in the time-of-flight with deflector time suggested that the deflector was acting as its own separate pulser instead of just gating the desired ions. This is especially problematic, because the large shifts in the time-of-flight and changing isotope ratios suggests that a different population of ions within the mass spectrometer was being observed. Without knowing the trajectory of these ions, which could not have followed the standard path, it was difficult to describe what was being measured when the deflector was pulsed.

ions without knowing their trajectory through the mass spectrometer. As a result, the timing scheme was abandoned and the deflector was kept on at a constant voltage in all of the experiments.

2.3 Aligning the Laser Beam and the Sample

The laser beam was aligned perpendicular to the target surface using the back-reflection method. First, the mirrors were adjusted so that the beam was perpendicular to the window of the ablation chamber. Then, the lens was aligned with the laser beam and moved laterally until the focused beam hit the desired spot on the target. Finally, the beam was shifted to the center of the mirror, and the process was repeated, if necessary, to ensure that the laser beam was in line with both the lens and the chamber window.

In order to set the distance between the target surface and the entrance to the mass spectrometer in Fig. 2.5, the sample was first positioned directly in front of the hole in the repeller plate. This was done visually with an uncertainty of 0.13 mm in the y direction. Once this distance was set to zero, the camera was adjusted to be in perfect focus with the sample. Because the camera was mounted on a linear stage, it was possible to determine the distance in the y direction between the sample and the mass spectrometer by using the stage position at which the camera was in focus as a proxy for the sample position. Based on this technique, the sample could be positioned relative to the camera with an uncertainty of about 0.05 mm in the y direction. The lens was also mounted on a translation stage, which was used to shift the laser beam vertically in the z direction until the ablation spot was in line with the hole. This was also performed visually to an uncertainty of 0.13 mm. Alignment of the sample and the laser beam with the entrance to the mass spectrometer could only be performed with the system vented and open and the repeller plate opposite the mass spectrometer removed. In the x direction, it was assumed that the center of the sample rod was exactly at the midpoint between the two repeller plates, but this could not be independently confirmed. An uncertainty of roughly 0.2 mm and no more than 0.5 mm is estimated for alignment of the target in the x direction.

2.3.1 Spot Size

Careful alignment was necessary, not only for allowing repeatability of the measurements, but also for ensuring uniform fluence over the irradiated area. Laser ablation performed after alignment yielded spots that were significantly more circular, and the surface texture within these spots tended to be much more homogeneous.

In order to maintain a set spot size when the sample was moved in the y direction along the axis of the laser, it was first necessary to determine the position at which the lens was completely in focus with the sample. This was done by firing 50-μJ shots to form craters along the target for a wide range of lens distances from completely underfocused to completely overfocused. Five shots were used for each spot to compensate for the variability in laser energy and to ensure that the ablated area would be visible even at lower fluences. The diameters of the craters were measured on a microscope, as shown in Fig. 2.13(a), and the location of perfect focus was found using linear fits on the points to either side of the smallest crater, as shown in Fig. 2.13(b).

Once the lens was at perfect focus relative to the target, moving the lens in either direction would increase the spot size. For these experiments, the lens was always underfocused such that the focal point was below the surface of the sample. Given an underfocus distance of δ, the spot size can be calculated as the focal waist of a Gaussian beam [89],

$$w(\delta) = w_0 \left[1 + \left(\frac{\delta}{z_R} \right)^2 \right]^{1/2}, \tag{2.1}$$

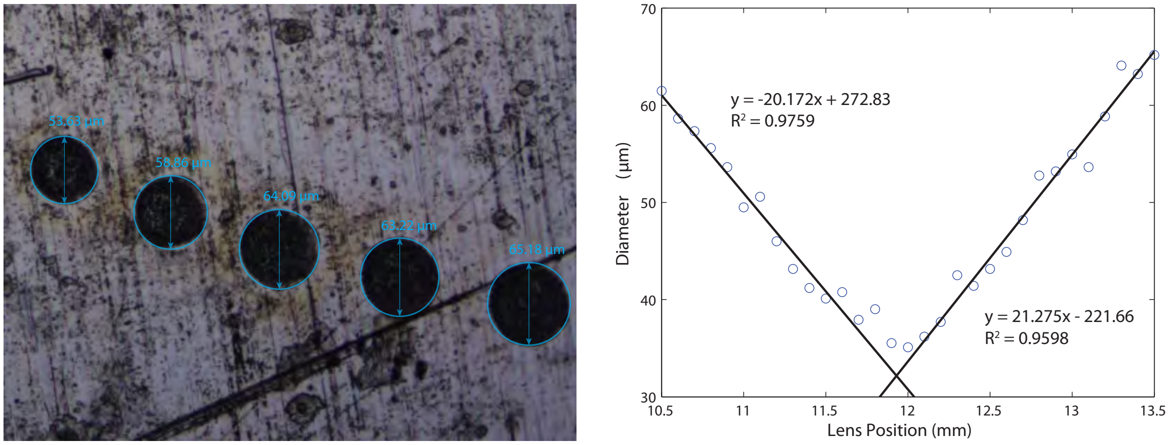

(a) Crater diameters measured for different lens positions.

(b) Linear fits on the diameters to determine the position of perfect focus.

Fig. 2.13 To control the spot size of the laser beam, it was helpful to determine the point at which the lens was exactly in focus with the sample. This was done by (a) ablating a series of craters with the lens slightly underfocused to slightly overfocused. The underfocused and overfocused crater diameters were fit to the lens position (b), and the intersection of the two linear fits was used as the point of focus.

where

$$z_R = \pi w_0^2/\lambda \quad \text{and} \tag{2.2}$$

$$w_0 = \lambda f/\pi w_1, \tag{2.3}$$

λ is the wavelength of the laser, f is the focal length of the lens, and w_1 is the radius of the beam. The waist radius at perfect focus is w_0, and the Rayleigh length, z_R, is the distance at which the diameter of the beam increases by $\sqrt{2}$. An iris was used to crop the beam diameter down to 4.3 mm, and the fused silica lens had a focal distance of 86.54 mm at the wavelength of 355 nm. The spot size was initially set to 50 µm with an underfocus of 0.99 mm, but, as discussed in 2.2.1, the fluence was too high for consistency over a large number of shots. As a result, the area of the spot was doubled to a diameter of 71 µm for an underfocus of 1.41 mm. Based on the measurements in Fig. 2.13, this typically produced a crater diameter of around 61 µm after 5 50-µJ shots. While the irradiated region is typically slightly larger than the area visibly affected by laser ablation, it seems more likely that the discrepancy between the measured and calculated diameters was due to the beam intensity not being Gaussian. Since the iris retained the center portion of the beam, the beam profile was probably more uniform than assumed by Eq. 2.1 and the spotsize slightly smaller than calculated.

2.4 Repeller Geometry

As shown in Fig. 2.14(a), the original instrument from Russo et al. [85] and Klunder et al. [86] included an ion trap, which had been modified to allow for introduction of a solid sample and to provide access to the laser beam and a camera. Although ion trapping and storage were never part of this study, the system was initially left intact and the endcaps were used solely as a set of repellers for accelerating the ions into the flight tube. The ring electrode, to which an rf voltage would be applied during normal operation of the ion trap in the original studies, was left floating for most of these early experiments. Attempts to ground the ring electrode seemed to make little difference in the resulting time-of-flight spectra.

This configuration sufficed for the tests in which the delay time was varied, but the small hole in the ring electrode of Fig. 2.14(a) restricted movement of the sample, so the spatial profile could not be obtained. To address this, the ring electrode was removed and replaced with aluminum spacers, as shown in Fig. 2.14(b). Eliminating the ring electrode, however, caused a qualitative change in the intensities measured for the two isotopes, as shown in Fig. 2.15. While there are many differences between the two plots, the most important is that isotope ratio was reversed between the two configurations. When the ring electrode was in place, in Fig. 2.15(a), the data showed a soft increase in the proportion of ^{107}Ag relative to ^{109}Ag centered around 16 µs. Without the ring, in Fig. 2.15(b), there is significantly more ^{109}Ag due to a sharp spike at 13 µs whereas the fraction of ^{107}Ag observed never rises much above half over the development of the plume. In addition, the distribution of faster ions centered at 11 µs and slower ions at 26 µs in Fig. 2.15(b) are much closer together in time than the faster and slower ion distributions at 9 and 32 µs respectively in Fig. 2.15(a).

Because the results changed so drastically once the ring electrode was removed, simulations were performed using COMSOL [90] to investigate the difference in the electric field between the two configurations. For the geometry with the ring electrode in Fig. 2.14(a), the voltage of the ring was set to ground in the simulation. This was done because the charged particles in the plume were not expected to shift the potential of the ring and because no major differences were observed experimentally in the oscilloscope traces between when the ring was grounded and when it was left floating. Based on the finite element models, there was indeed a large difference between the electric field in the configuration with the ring electrode in Fig. 2.16(a) and the electric field of the system without the ring in Fig. 2.16(b). The ring electrode, which has a voltage potential of its own, introduced a significant distortion to the electric field in Fig. 2.16(a). Since the stainless steel ring is completely conductive, the electric field gradient must remain perpendicular to the surface of the ring and the field lines have been bent in that direction. This is especially critical near the target, where positive ions below the centerline would be accelerated radially outward toward the ring while ions above the centerline would be accelerated radially inward toward the center of the ion trap. While this effect is to some extent unavoidable because of the conductive silver target, the radial field is much less dramatic without the ring. In

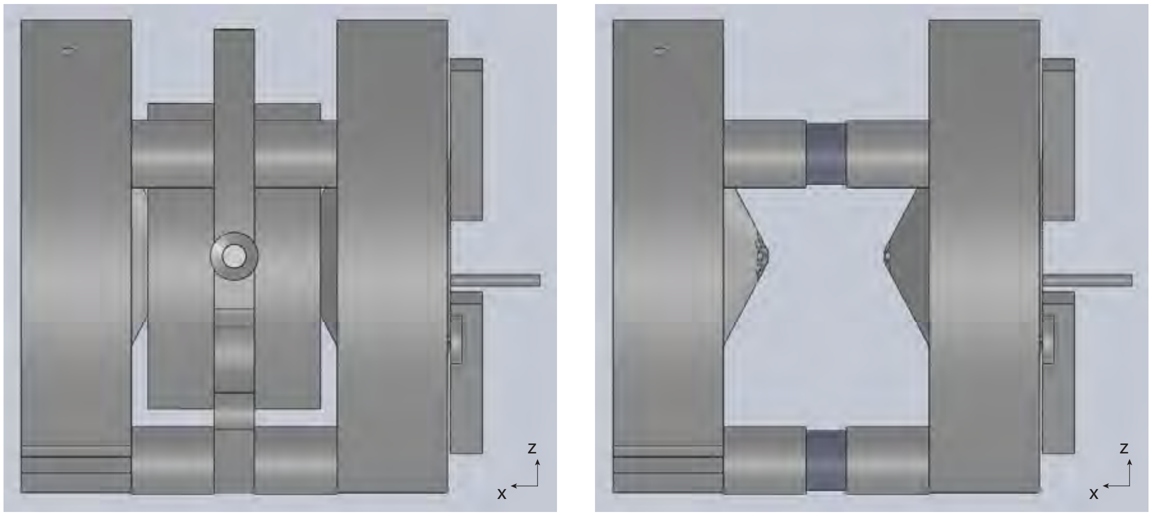

(a) The full ion trap, with the ring electrode left floating.

(b) The ring electrode removed to allow for greater movement in the y direction.

Fig. 2.14 Although the original system (a) included an ion trap, it was not used to trap ions and the endcaps were simply pulsed in order to eject the ions into the mass spectrometer. After some initial experiments, the ring electrode was removed (b) so that the spatial profile of the plume could be obtained, but this led to an unexpected change in the results.

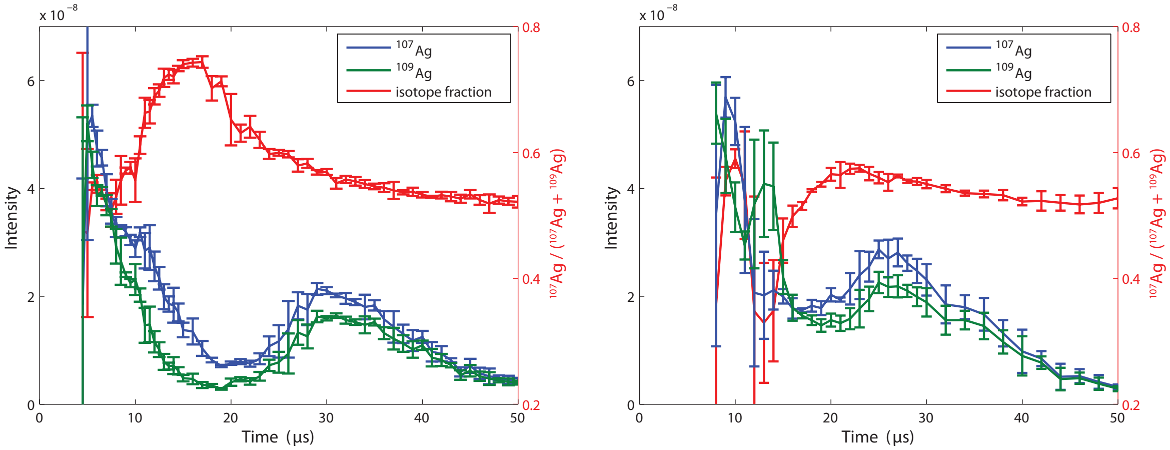

(a) Temporal profile of silver isotopes with the ring electrode in place.

(b) Temporal profile of silver isotopes with the ring electrode removed.

Fig. 2.15 Since the ring electrode was usually left unconnected to any voltage source, removing the ring was not expected to have much of an effect on the results observed. The difference in the temporal profile between the two conditions, however, was quite dramatic, with the original configuration (a) showing a higher proportion of the lighter ^{107}Ag isotope and the modified version (b) a higher proportion of the heavier ^{109}Ag.

the absence of this large grounded surface, the electric field is much closer to being linear, making the system more conducive to sampling the desired cross-section of the plume, as illustrated in Fig. 2.5.

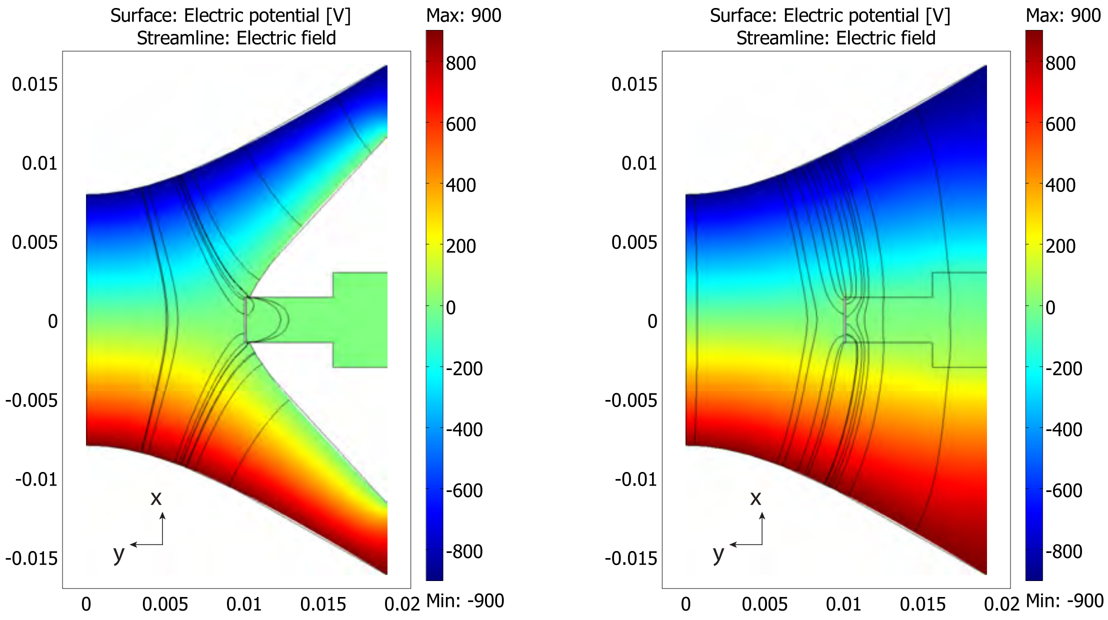

(a) Electric field of the ion trap with the ring electrode in place.

(b) Electric field of the ion trap with the ring electrode removed.

Fig. 2.16 Finite element analysis was performed using axially symmetric geometries. The hyperbolic endcaps responsible for pulsing the ions into the flight tube are at the top and bottom, and a cross-section of the ring electrode is to the right of the potential plot (a). In the original configuration (a), the grounded ring electrode distorts the electric field by bending field lines perpendicular to the conductive ring. This exerts a force radially outward on ions below the center of the trap and radially inward on ions above. Removing the ring electrode (b) causes the electric field to become more linear.

The potential used to sample the plume, however, would be almost completely linear if flat electrodes were used. Based on the solution in Fig. 2.17, only the region near the target surface deviates significantly from the desired field. This departure is due to the conductive silver sample, from which the electric field lines must extend in a perpendicular direction, and unavoidable if a metallic target is to be used. Even in this region, however, radial fields have been minimized by the flat plates.

Since the ion trap was no longer being used and flat plates could provide a more linear electric field, new electrodes, as shown in Fig. 2.18, were machined. These circular electrodes have a raised lip, visible in Fig. 2.18(b), to accomodate the same ceramic spacers

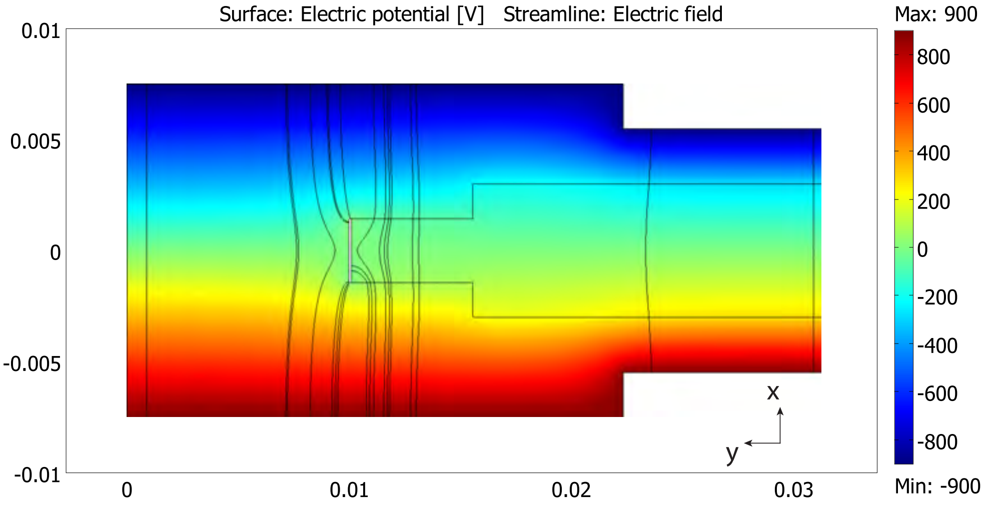

Fig. 2.17 Using flat surfaces for the repellers generates an electric field that is almost completely linear. The main non-linear region in the field is near the conductive target, and this deviation is both unavoidable in practice and somewhat overestimated by the axial symmetry used in the model.

used in the original trap and to keep the electric potential more uniform at the boundaries. The plates at the center of each electrode were constructed from thin sheets of stainless steel, and these shims could be swapped out to provide different hole patterns through which ions enter the mass spectrometer. Testing on these flat electrodes started out with 7 holes in a honeycomb pattern, as opposed to 19 in the original endcaps, but ultimately a single hole was yielded sufficient intensity. The opposing electrode was blank and did not have any holes in the final configuration.

Experiments conducted with the flat repellers produced results that were similar but not exactly the same as when using the endcaps alone. Most importantly, Fig. 2.19 reproduces the increase in ^{109}Ag relative to ^{107}Ag, although the change in isotope ratio is centered slightly later at 19 µs instead of 13 µs as in Fig. 2.15(b). In addition, the slower distribution of ions at around 27 µs in Fig. 2.19 is not as prominent. This may be due to the reduction in the number of holes in the repeller or different voltage focusing conditions, as will be discussed in Sec. 3.2.2. That the general characteristics of the temporal profile are much more similar to Fig. 2.15(b) without the ring than to Fig. 2.15(a) with the ring confirms that the electric field generated by the flat plates is fairly close to that of the endcaps only. If the actual potentials are similar to those plotted in Fig. 2.17, the ions sampled should resemble the cross-section in Fig. 2.5.

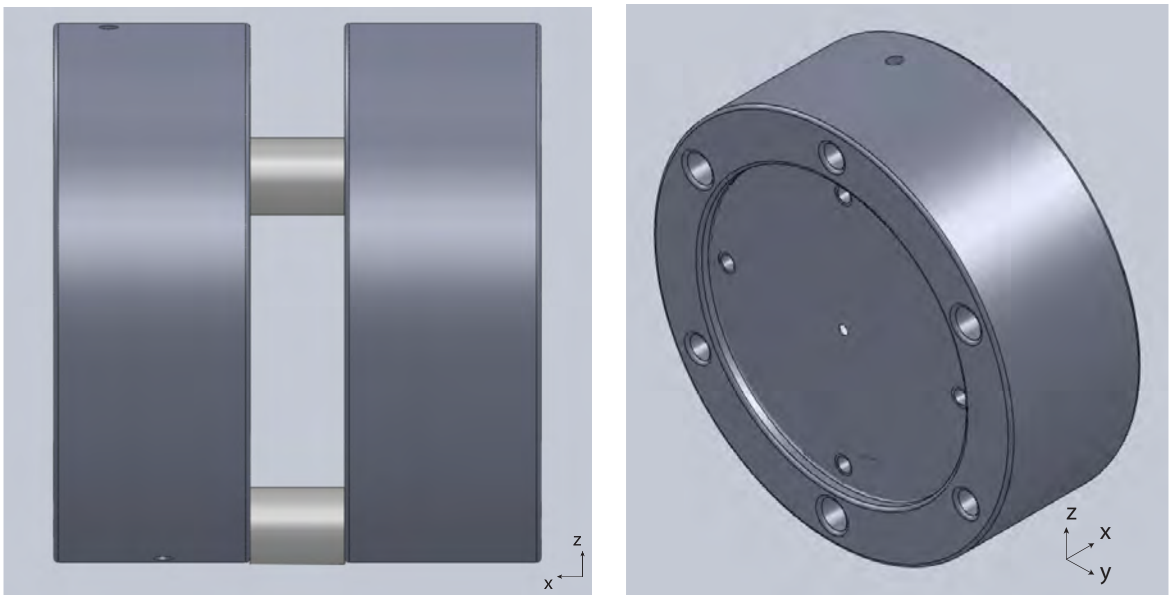

(a) Flat electrodes designed to provide a linear electric field.

(b) Only a single hole for transmitting ions to the flight tube.

Fig. 2.18 Flat repellers were used to ensure that pulsing the electrodes with a high voltage potential would select a perpendicular cross-section of the plume. The removable shim in this design allowed the number and size of the holes to be changed.

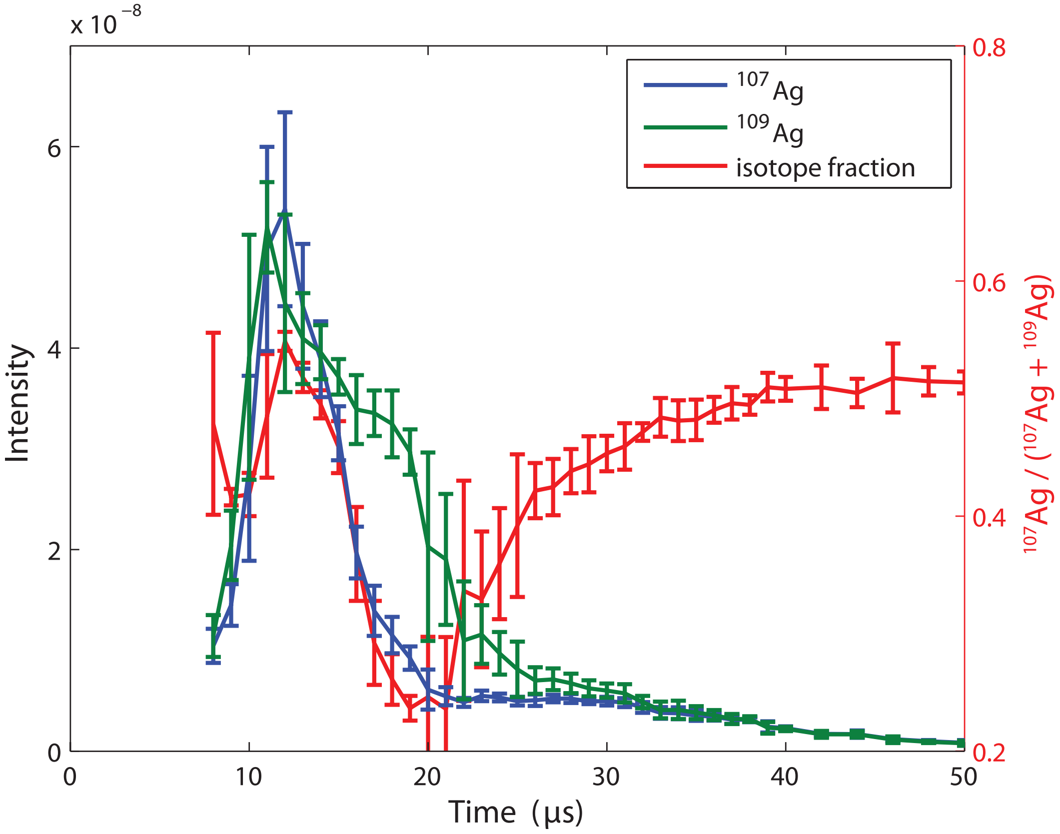

Fig. 2.19 Temporal profile of silver isotopes with flat plate repellers. The variation in isotopic composition, with significantly more ^{109}Ag than ^{107}Ag in the shoulder of the faster ion distribution is qualitatively similar to the results obtained from using only endcaps without the ring. Since many other parameters have been changed, the agreement between these two results suggests a fairly robust effect despite small changes to the electric field.

Chapter 3

Instrument Parameters

The electrodes in the time-of-flight mass spectrometer, as shown in Fig. 3.1, are used to accelerate, decelerate, focus, deflect, and reflect the ions in the system. Working in concert, they control the signal intensity, the mass resolution, and the selection of ions that are ultimately detected by the microchannel plate. The electrodes do so by altering the electric fields in the mass spectrometer, bending the ion trajectories toward or away from the detector and changing the ion time-of-flight by moderating the kinetic energy or the flight path or both.

Due to the complexity of the system and the interaction between the different electrodes, simulations and calculations were needed to determine appropriate parameters for the experiments. The electrodes in the system can be broadly divided into two groups: ones change the direction of the ions and ones that affect the ion energy. The deflector and focus electrodes are used primarily to alter the ion direction and are discussed in Sec. 3.1. Since it is difficult to treat the geometry analytically, the finite difference program SIMION is used to describe how the ion trajectories change when different voltages are applied [91]. While the deflector and the focus can mostly be adjusted and optimized independently, the repellers and reflectron both manipulate the ion energy and their effects are heavily coupled. As a result, a more comprehensive framework is needed to explain how these parameters influence the time-of-flight and reject certain ions from the system. This analysis is presented in Sec. 3.2.

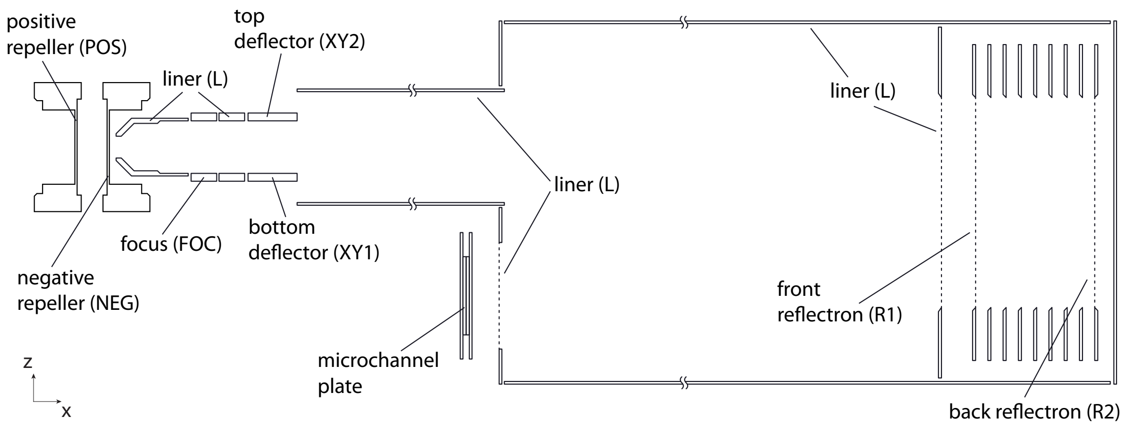

Fig. 3.1 The time-of-flight mass spectrometer allows for the voltage of all of the electrodes in the system to be adjusted. The repellers eject the ions from the plasma, the liner provides additional acceleration, the focus compresses the ion beam, the deflectors angle the ions toward the microchannel plate, and the reflectron reverses the ions while compensating for the kinetic energy in the time-of-flight. As described in Sec. 3.2.2, the reflectron also serves as an energy filter. Within the system, the liner potential of -1300 V serves as a baseline minimum voltage.

3.1 Ion Trajectory

Optimizing the ion trajectory is important not only for adjusting the signal intensity but also for determining which ions are able to make it to the detector. One set of voltages might allow slow ions to be observed while another might result in electric fields that deflect them off-axis. Certain parameters might even cause an unrepresentative population of ions to be selected for measurement, as occurred with the pulsed deflector in Fig. 2.12. Since many more ions enter the mass spectrometer than can be recorded by the detector in a single trial, tuning the trajectory is necessary to direct the appropriate subset of ions to the microchannel plate.

To determine the trajectory of the ions, the entire time-of-flight mass spectrometer was modeled in SIMION [91]. SIMION consists primarily of a finite difference solver that computes the electric potential at each point in the grid based on the specified electrode configuration. The electric field is calculated from the potential array, and ion trajectories are obtained by numerical integration using a fourth order Runge-Kutta method.

3.1.1 Plume Velocity

One of the major constraints of using this system to study laser ablation is that the instrument is limited in its ability to observe ions with high forward velocities. Since the detector is only 40 mm wide, an ion can move no more than 20 mm from the center of the flight tube over its time-of-flight before missing the microchannel plate. Given a typical kinetic energy of 1300 eV from the repeller and a flight path of 1764 mm, the ion will take a minimum of 36.4 µs to reach the detector, restricting its orthogonal speed to below 550 m/s. While the Einzel lens, as will be discussed in Sec. 3.1.3, can be used to steer some of the ions back toward the center of the flight tube, the geometry of the instrument favors slow speeds in the y and z directions. This is particularly a concern in the y direction perpendicular to the sample, since the velocity of plume ions is typically strongly forward-peaked [92, 93].

Since ions with high velocities orthogonal to the mass spectrometer can not be recorded and ions in the ablation plume have high velocities in the plume direction, much of the plume, even if it enters the flight tube, will not be detected. In fact, if there are no collisions in the plume and the target is more than a couple millimeters away from the entrance to the mass spectrometer, it should be impossible to observe any ions at all in the first microseconds after the laser pulse. Assuming a collisionless plasma, the ions will need considerable forward velocity to reach the hole in the repeller plate within a couple microseconds, but this same velocity will cause it to hit the wall of the flight tube rather than making it to the microchannel plate. This is borne out by the simulation results in Fig. 3.2, which show that the fastest ions that can reach the detector have a velocity of around 700 m/s and, as a result, nothing will be measured before 7 µs at a hole distance of 5 mm or 14 µs at a distance of 10 mm. Moreover, unless the ion velocities are within the narrow range set by the markers in Fig. 3.2, the ions will not be counted. These predictions follow from the assumption that there are no collisions during plasma expansion. If ions are not allowed to change velocity, aside from the electric field generated by the repellers, their initial velocities must reside within a narrow window that allows them both to enter the flight tube and to hit the microchannel plate.

As shown in Fig. 2.4, however, many ions are observed at a distance of 10 mm before 14 µs, even without additional focusing. Hence, ions must exist that have low velocities in the forward y direction when entering the mass spectrometer, but these slow ions must have had higher velocities prior to entering the flight tube. Without higher initial velocities, they could not have reached the hole in the repeller plate and entered the mass spectrometer so early in time. Collisions must play an important role in the development of the plume, at least within the first few microseconds, to account for the large number of ions measured at early times. Furthermore, all of the ions detected within the first few microseconds are ions that have experienced a collision near the entrance of the mass spectrometer and that have been scattered in as a result, and are not those flowing along the plume stream directly from the target surface.

3.1.2 Ion Direction

In a reflectron time-of-flight mass spectrometer, the ions are brought back toward the ion source in order to compensate for different starting energies. If the ions travel along the same line in both directions, an annular detector must be used and the ions may collide with one another in the reflectron. For simplicity, most systems angle the direction of flight

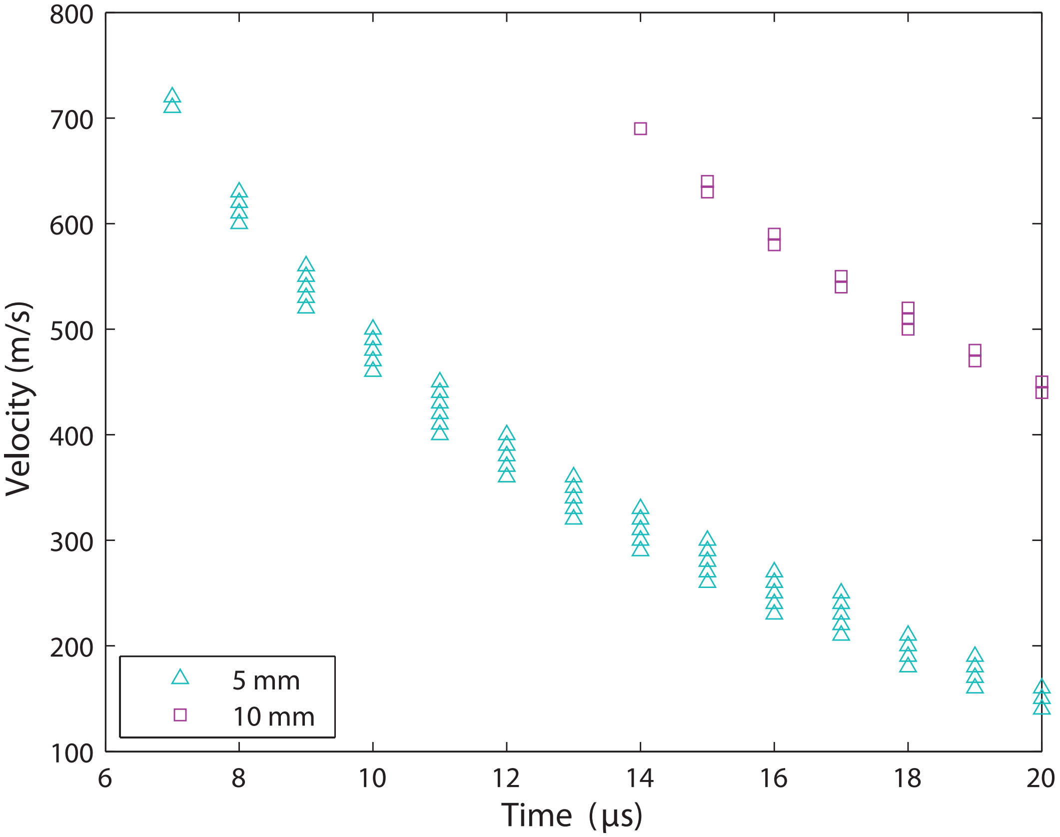

Fig. 3.2 If there are no collisions in the laser plasma, only ions that have initial velocities within a small window will be able to make it through the hole in the repeller plate and ultimately reach the detector. In particular, no ions will be observed before 7 μs at a distance of 5 mm or before 14 μs at 10 mm. This shows that ions must collide within the ablation plume in order to match experimental observations.

toward the reflectron such that the ions ultimately reach a detector below or to the side of the ion source. In this instrument, as shown in Fig. 3.1, deflector plates are used to direct the ions toward the reflectron at a downward angle, so that they will arrive at a microchannel plate below the repellers.

The deflectors create the electric field that gives the ions the downward velocity needed to reach the microchannel plate instead of doubling back on themselves. Although the electric field is mostly linear between the two electrodes, the potentials extend beyond the plates, as shown in Fig. 3.3. Since the acceleration on the ions can not be calculated directly, simulations are needed to map the trajectories. In this case, the repellers were set to 900 and 0 V and the reflectron to 720 and -105 V, typical parameters for collecting the entire slice of the plume, as will be discussed in Sec. 3.2.4. The ion velocities were assigned based on a Maxwell-Boltzmann distribution with an average kinetic energy of 5 eV, and the starting point was set at the center of the repellers. Without a good model for the ions in the plasma, the assumption about the ion positions and velocities was somewhat arbitrary, but the particular distribution did not make a significant difference for optimizing the ion direction. For example, the small hole in the repeller plate narrowed the velocity spread into the mass spectrometer considerably, but simulations with larger holes yielded similar results. Likewise, the specific isotope used had minimal effect on the trajectory, so ^{107}Ag was used for all of the simulations in this section and in Sec.3.1.3.

Because the ions reverse direction in the reflectron, it is easier to examine their trajectory through the flight tube just before they enter the reflectron, as shown in Fig. 3.4. Furthermore, the ions must pass through small windows in the reflectron plates to enter the reflectron, and it is helpful to see which ions are blocked by these shims when optimizing the electrode voltages. The reflectron sets the voltage at 20 different positions on the x axis along the flight tube to create a linear electric field. To allow the ions to pass through shims with small windows must be used instead of grids, 20 of which would reduce ion transmission to unacceptable levels. Despite the narrow width of the windows, the shims do not prevent any ions from reaching the detector, which is the same size. Since the ion trajectories tend to diverge from the centerline, only those within an even smaller region of the reflectron will be able to hit the microchannel plate. In Fig. 3.4, ions that reach the microchannel plate are in red, those that are able to be reflected back out of the reflectron are in green, and those blocked by the shims on their way into or out of the reflectron are in blue. No deflection has been applied to the ions in Fig. (a), because the deflectors are at the liner voltage of -1300 V. In contrast, Fig. (c) is close to optimal in that most of the ions at the center of the beam are able to reach the detector.

Each set of repeller and reflectron voltages, however, produces different ion velocities and times-of-flight, so slightly different levels of deflection are needed for each condition. To optimize the deflector voltage, simulations were performed for ions with starting positions along the centerline of the repeller hole for each parameter set. The optimization results for the entire plume parameters described above are shown in Fig. 3.5. The deflector voltage with the range best centered on the microchannel plate, in this case -1201 V, was used in experiments. While adjusting the deflector voltage during experiments did influence

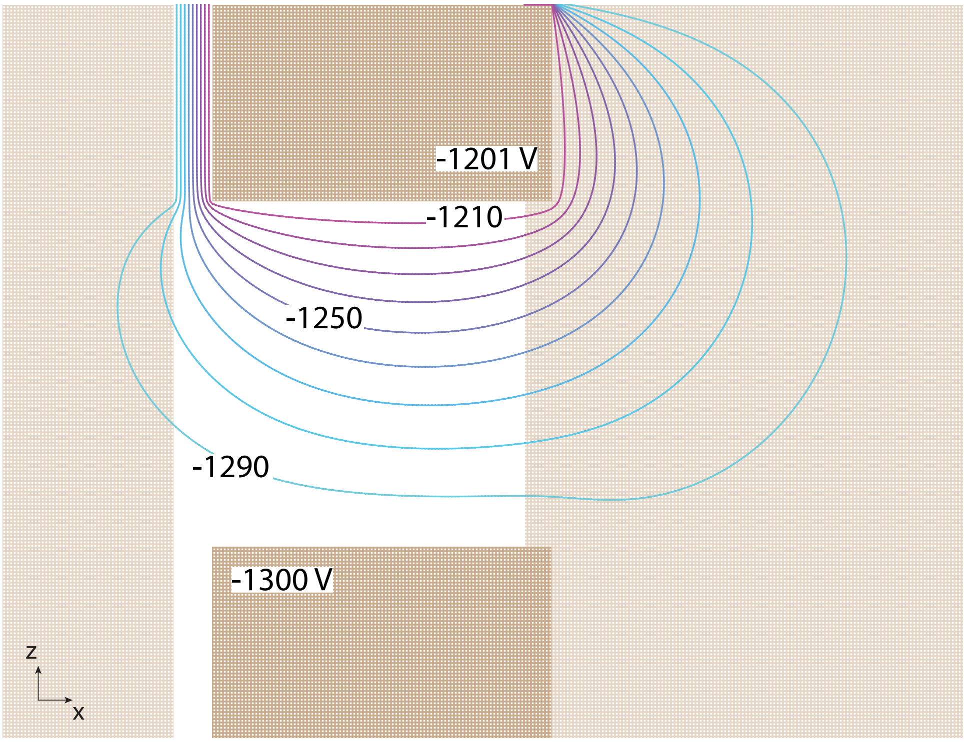

Fig. 3.3 The potential difference between the deflector plates creates an electric field that angles the ions downward in the negative z direction toward the microchannel plate. Because the potential gradients extend beyond the region between the two electrodes, a finite difference method is needed to calculate the electric field and ion trajectory. Note that ions closer to the top electrode will be deflected more because the higher potential slow them down, causing them to spend more time the deflector region. For the same reason, slower ions in the x direction will be deflected more than faster ions.

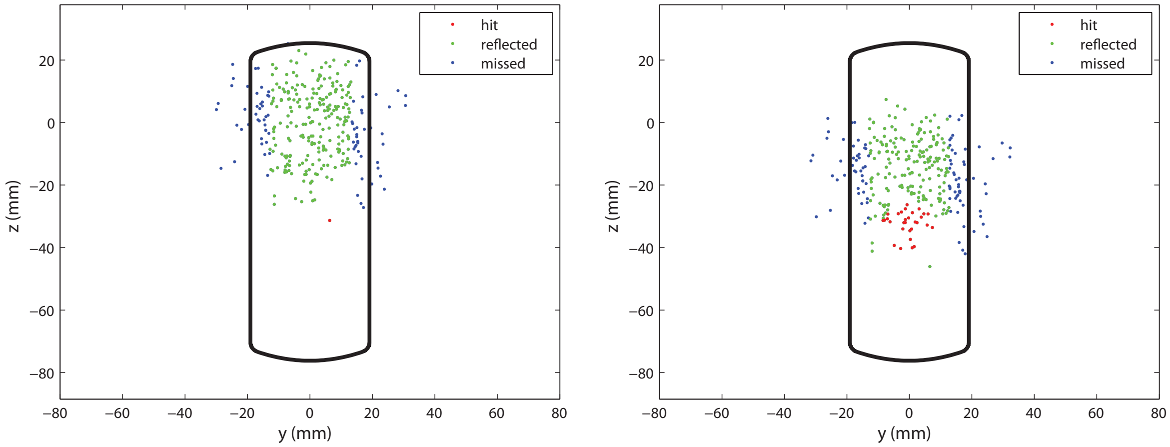

(a) Simulated ion trajectories at the reflectron with the top deflector at -1300 V.

(b) Simulated ion trajectories with the deflector at -1250 V.

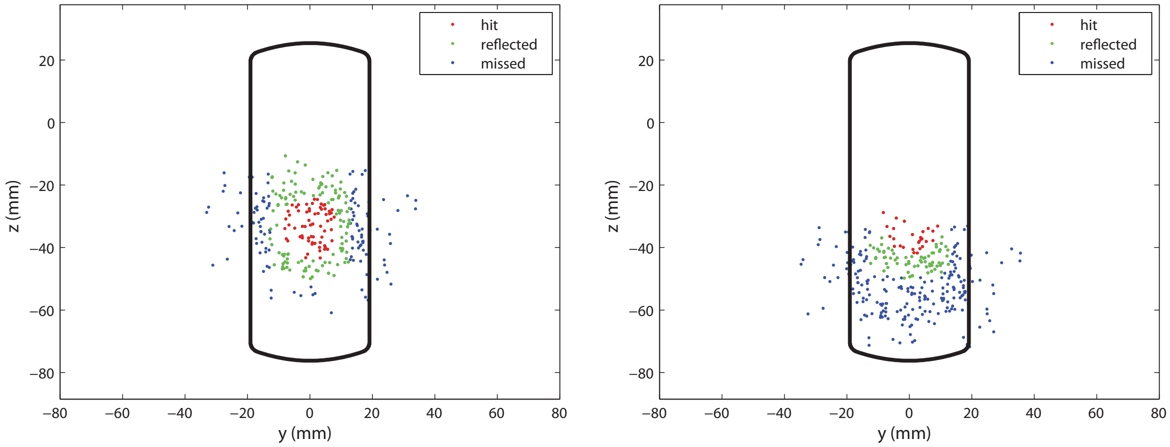

(c) Deflector at -1200 V.

(d) Deflector at -1150 V.

Fig. 3.4 Since ions trajectories within the time-of-flight mass spectrometer are reversed at the reflectron, it is easier to study the distribution of ions based on their position just before entering the reflectron. In addition, the shims that make up the reflectron have fairly small windows through which ions must pass if they are to be reflected, as indicated by the oblong outline in the plots. The ions in blue hit the shims on their way into or out of the reflectron, while the ones in green are successfully reflected back toward the detector. Only the ions in red actually reach the microchannel plates. If the deflector voltage is the same as the liner (a), the ion trajectory remains unchanged and few arrive at the detector. A voltage of -1200 V (c) comes very close to centering the ion beam on the microchannel plate.

the ion intensities, the effect is much more subtle than that predicted by the simulations, most likely because of a broader spread of ion distributions due to collisions.

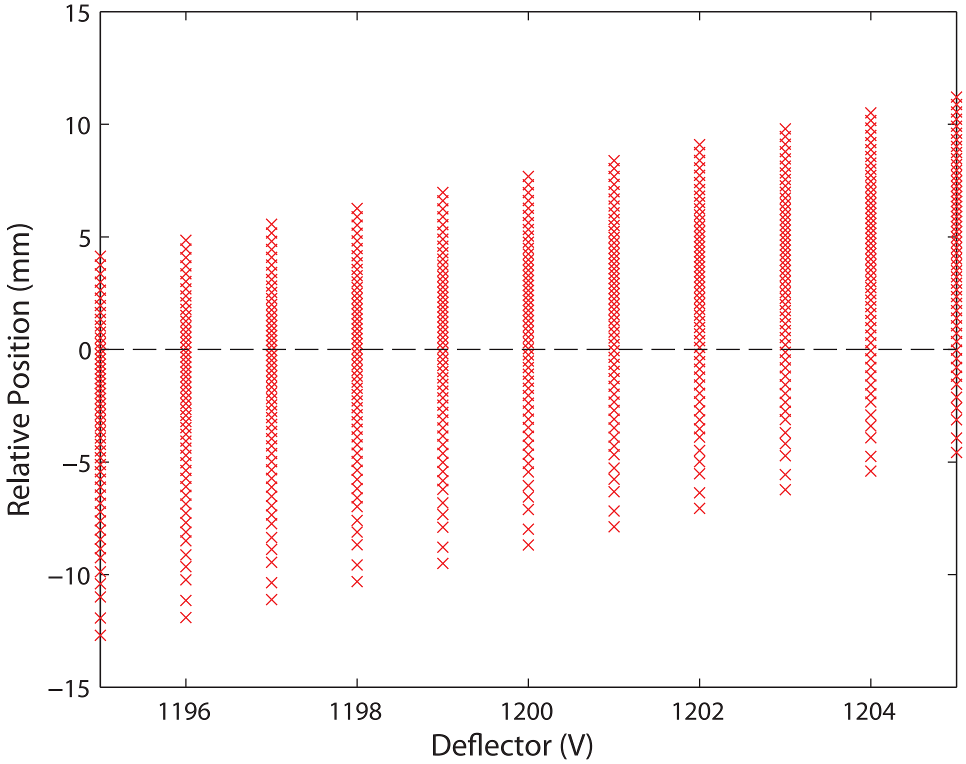

Fig. 3.5 The final z position of ions relative to the centerline of the microchannel plate for different deflector voltage. Although all of the ions within a single series started along the centerline of the repellers, they each had different velocities while passing in between the deflector plates, which resulted in slightly different degrees of deflection. The voltage with the position range closest to the center of the detector was chosen for the experiments. This was repeated for each set of repeller and reflectron voltages.

3.1.3 Ion Focusing

Fig. 3.4 showed that it is necessary to deflect the ions toward the microchannel plate, but it may also be helpful to focus the beam in order to narrow the spread of ions. Focusing the ions not only increases the intensity of the signal but also ensures that a greater proportion of the ions entering the flight tube have been detected. Including a larger percentage of ions, however, also implies averaging over a larger region of the laser plume. Hence, ion focusing involves the typical tradeoff between the intensity of the signal and the granularity of the sampling. Since this study focuses on changes within the plume, the resolution with which the plume can be profiled is especially critical. Nevertheless, it is important to consider that defocusing the ion beam may result in sampling not only a more specific area within the plume but also potentially a more biased ensemble of velocities within that specific area.

There are two methods for adjusting how are the ions are focused in the time-of-flight instrument: the deflectors and the einzel lens. Brief studies have been performed on both by simulating the ion trajectories using the same conditions as described in Sec. 3.1.2, in which the ions were given an average initial kinetic energy of 5 eV and centered exactly between the two repeller plates. As before, the simulations are not especially sensitive to the exact distribution of the intial ions. The actual spread of ion velocities from the repellers is expected to be broader and more forward-peaked than those used in the simulations. Ion focusing during experiments should thus have a similar but greater effect than observed in the simulations.

Focusing the ion beam with the deflectors produces the trajectories in Fig. 3.6. The voltages of -1201 V and -1300 V from Fig. 3.5 have been chosen as the baseline case in which there is minimal focusing beyond directing the ions toward the microchannel plate detector, as shown in Fig. 3.6(a). From this point, increasing both voltages by the same amount narrows the beam height while keeping the ions centered on the detector, as shown in Fig. 3.6(b). The focal plane is close to the surface of the reflectron and not far from the microchannel plate in Fig. 3.6(c), a near optimal condition in which the ions have been compressed to a narrow slice. Further increasing the voltage, as in Fig. 3.6(d) overfocuses the beam, expanding the distribution of ions once more as they head toward the reflectron. If it was only important to compress the ions along the z direction and not along the direction of the plume along the y axis, then deflector voltages fairly close to Fig. 3.6(c) should be used.

Because the deflectors are flat plates designed to angle the beam rather than compress it, they are very effective in minimizing the spread of ions in the z direction but may actually broaden the distribution in the y direction. To focus the ions in both directions, an einzel lens is used, in which a circular electrode increases the potential in all directions around the ion beam. As with the deflectors, the higher the voltage on the einzel lens relative to the liner baseline, the greater the degree of focusing. This is shown in Fig. 3.7, in which the voltage is increased from zero focusing at 1300 V in Fig. 3.7(a) to the maximum focus of 0 V in Fig. 3.7(d). A much larger change in potential is required when using the einzel lens compared with the deflectors, partly because the electrode in the einzel lens is half the length of the deflectors. In addition, the einzel lens is bracketed by two electrodes at the liner voltage of -1300 V, which helps create a more uniform field but also restricts influence of the focusing electrode. Consequently, the ions are not focused at the detector until a voltage of around 400 V, beyond the limit of the current system. As with the deflectors, the einzel lens has a greater effect on ions near the outer circumference of the beam, because they will not only be subject to higher potentials but also experience them for slightly longer periods of time, since the increase in potential energy along the edges corresponds to a decrease in kinetic energy and velocity. Based on the simulation results, focusing with the einzel lens is highly preferable to using the deflectors, because the ions are compressed uniformly toward the centerline of the beam, even if a larger potential difference is required

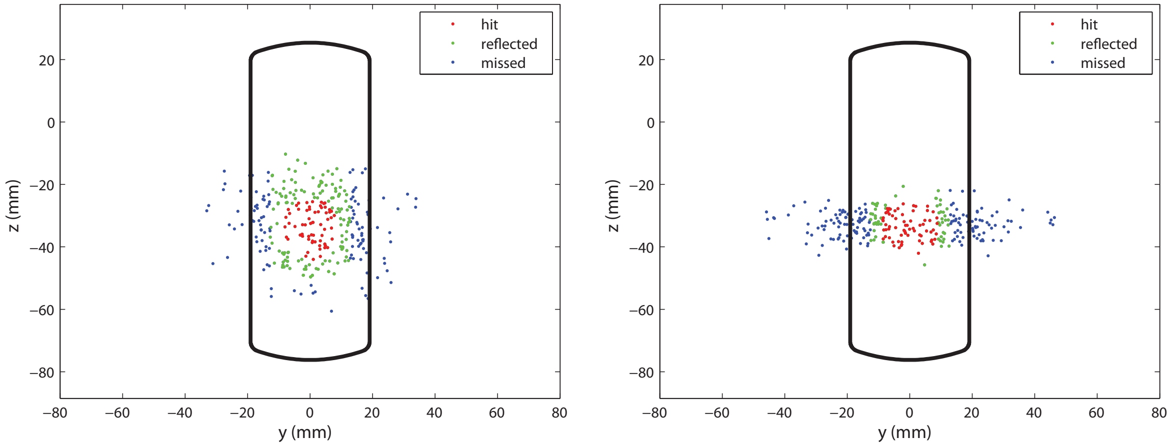

(a) Simulated ion trajectories at the reflectron with the deflectors at -1201 V and -1300 V.

(b) Simulated ion trajectories with the deflectors at -1001 V and -1100 V.

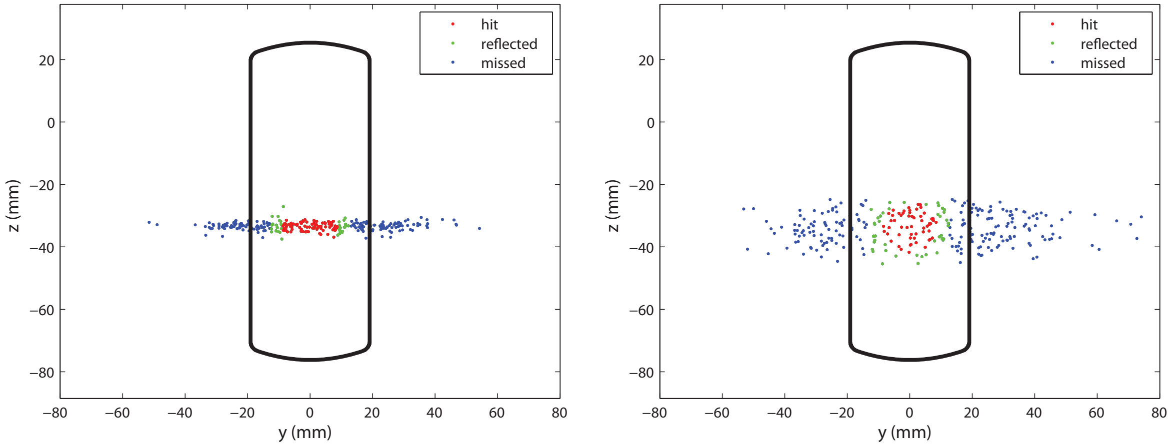

(c) Deflectors at -901 V and -1000 V.

(d) Deflectors at -701 V and -800 V.

Fig. 3.6 Increasing the voltage on both deflectors simultaneously from the optimal direction-only deflector condition (a) compresses the ions in the z direction (b) but causes the spread to increase slightly in the y direction along the length of the plume. The ions are almost perfectly focused on the microchannel plate in (c) and become overfocused with additional voltage in (d). As before, the red ions reach the detector, the green ions are able to leave the reflectron and double back toward the detector, and the blue ions collide with the surface around the window on their way either into or out of the reflectron.

to achieve the same degree of focusing. Furthermore, such a high level of focusing may prove excessive if the microchannel plate becomes saturated as a result.

Since the einzel lens does not become overfocused until around 400 V, the maximum available potential of 0 V should be used if the goal is to collect the largest percentage of ejected ions. If the detector becomes saturated or if this samples over too large a region of the plume, an intermediate value between -1300 and 0 V can be selected, but the choice of focus voltage will represent a somewhat arbitrary balance between yield and specificity. Because this parameter is more subjective, experiments were conducted to determine how the voltage on the einzel lens affects the results. The temporal profile of the isotope content for the four voltages in Fig. 3.7 are shown in Fig. 3.8.

The increase in signal intensity is relatively modest from -1300 V in Fig. 3.8(a) to -800 V in Fig. 3.8(b), with sharper rises at -400 V in Fig. 3.8(c) and 0 V in Fig. 3.8(d). The plots are fairly similar qualitatively, except that the proportion of ^{107}Ag near 20 μs increases with focus, causing the rise in the fraction of ^{107}Ag to be sharper as well. The only other major difference is the appearance of a small peak very early in Fig. 3.8(d), which is probably due to enhanced collection of the early ions. Focusing appears to have a stronger effect on the slower ions near 20 μs than the faster ions near 6 μs. This suggests that the faster ions are more forward-peaked compared to the slower ions and are less influenced by radial compression as a result. Because the curves of the isotope intensities and the ^{107}Ag fraction are the smoothest in Fig. 3.8(a), the liner voltage of -1300 V was used for the einzel lens, which corresponds to zero focusing or not using the lens at all. From Fig. 3.8, increasing the focus seemed to distort the signal without enhancing the phenomenon of isotope separation. In addition, eliminating the focus makes the problem easier to model computationally and conceptually.

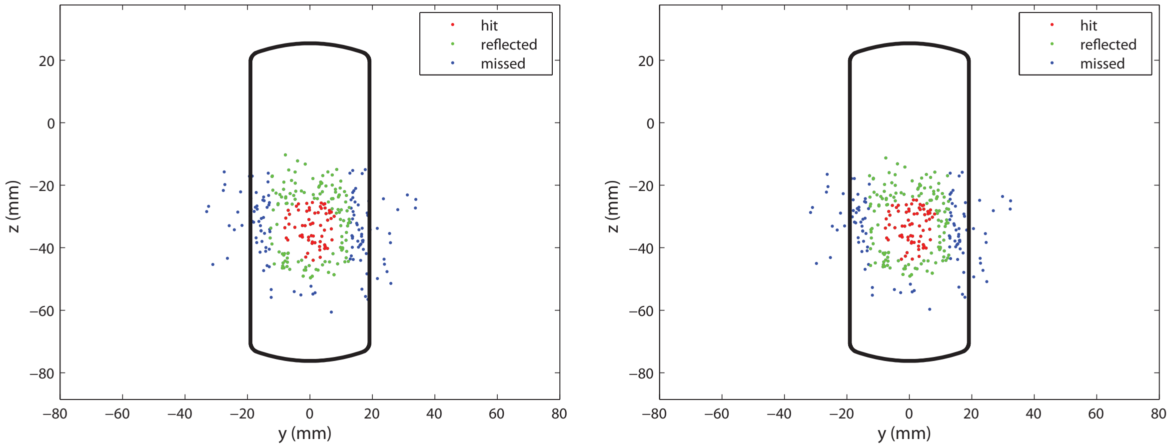

(a) Simulated ion trajectories at the reflectron with the focus at -1300 V.

(b) Simulated ion trajectories with the focus at -800 V.

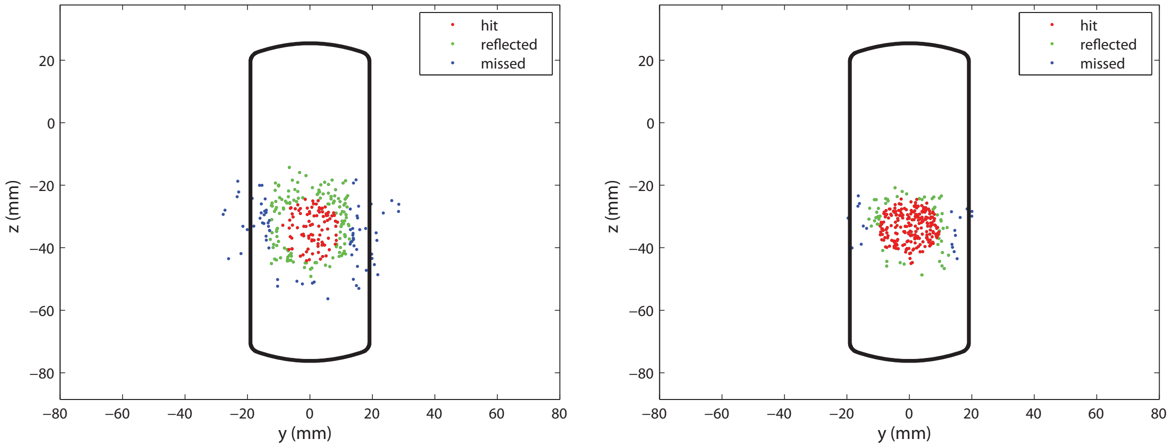

(c) Focus at -400 V.

(d) Focus at 0 V.

Fig. 3.7 Applying a voltage to the middle element of an einzel lens allows the ion beam to be compressed uniformly about the centerline but requires a higher potential difference than the deflectors to achieve the same degree of focusing. As before, -1300 V (a), the liner potential of the flight tube, represents no focus. The maximum focus allowed by the system at 0 V (d) still leaves many of the ions in the test distribution outside the microchannel plate, but may well have saturated the detector under experimental conditions.

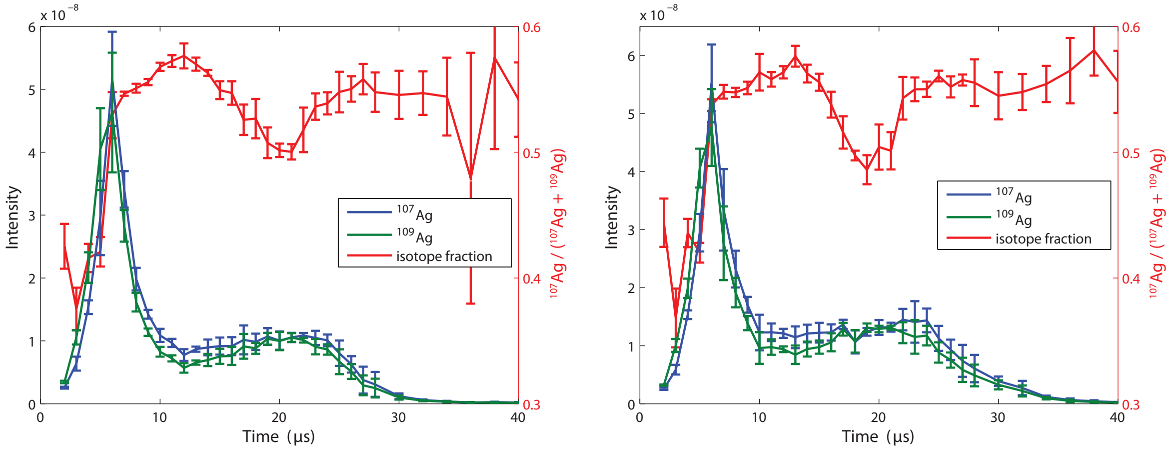

(a) Isotope content 5 mm from the target over time with the focus at -1300 V.

(b) Isotope content over time with the focus at -800 V.

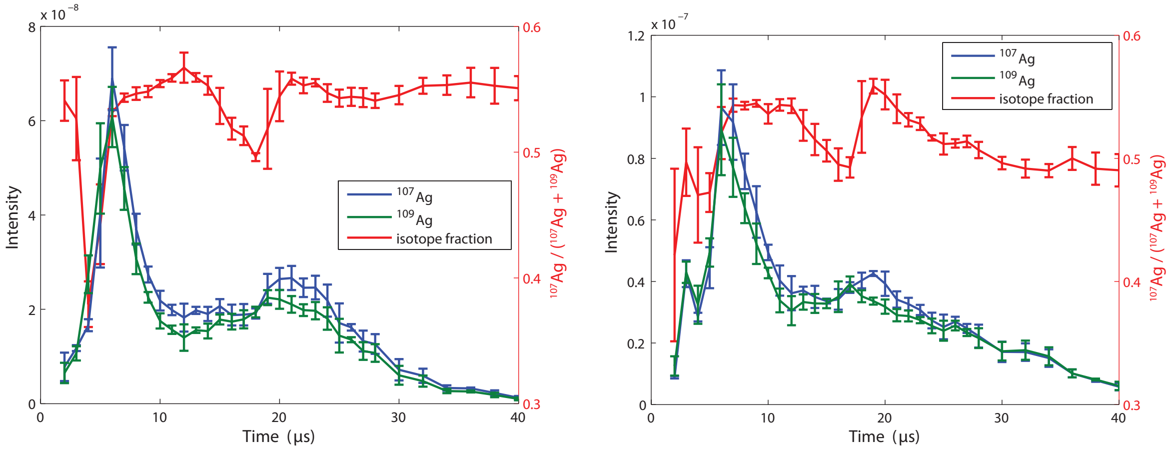

(c) Focus at -400 V.

(d) Focus at 0 V.

Fig. 3.8 The isotope intensities were measured over time for a range of focus voltages, from -1300 V (a), corresponding to no focusing, to 0 V (d), the maximum possible with this power supply. Increasing the focus had a larger effect on the slower ions near 20 μs, enhancing the intensity of both isotopes but especially the proportion of ^{107}Ag over ^{109}Ag. This causes the ^{107}Ag fraction to change more sharply but does not increase the overall magnitude of the change. Because the curves in (a) are smoother and appear to represent simpler underlying distributions, the voltage was set at -1300 V and no focusing was used.

3.2 Ion Energy

The primary purpose of the reflectron in a time-of-flight mass spectrometer is to compress the distribution of ions in time so as to provide sharper discrimination between particles of similar masses. In time-of-flight mass spectrometry, the flight time depends in part on the ion's initial velocity. Without a reflectron, a heavier ion might arrive at the detector earlier than a lighter ion, if it had a higher initial velocity in the direction of the detector. The reflectron seeks to compensate for this spread in ion energy by forcing ions with higher velocities to travel longer distances and against higher electric potentials before being reflected back toward the detector. If the potentials in the reflectron and the repellers are tuned correctly, two ions of the same mass will reach the detector at the same time, proportional to the square root of the mass, despite a large difference in velocity. The basic considerations for tuning the reflectron and the repellers in concert are described in Sec. 3.2.1.

The reflectron, however, does not just compensate for the spread in kinetic energy but also serves as an energy filter for the mass spectrometer. The electric field in the reflectron is governed by two voltages, one at either end of the field. As will be explained in Sec. 3.2.2, these two voltages set upper and lower bounds on the kinetic energy of ions that can be detected by the mass spectrometer. While Sec. 3.2.2 focuses on the implications for the starting position of the ions, their initial velocities also affect the kinetic energy spread and range of detectable ions and will be discussed in Sec. 3.2.3. Finally, Sec. 3.2.4 derives the equations governing the time-of-flight and describes the effect of the position and velocity distributions on the time-of-flight spectra.

3.2.1 Mass Resolution

While using the reflectron to compensate for velocity in a single direction is fairly straightforward, the situation is more complicated in practice when an electric field is used to accelerate the ions into the flight tube. For example, it is impossible to compensate for two ions with the same speed but opposite directions within a static electric field. Since the ion moving backward against the field will eventually arrive at the same velocity and position as the ion moving forward with the field, the backward ion will follow exactly the same trajectory as the forward ion some short time later. As a result, the backward ion will arrive at the detector after the forward ion and the two will have different times-of-flight. If the initial velocity of the forward particle is v_0 in an electric field E, the difference in their times-of-flight can be derived from the velocity of the backward particle [94],

$$v_0 = \frac{qE}{m}t - v_0, \tag{3.1}$$

yielding a turn-around time of

$$t = \frac{2mv_0}{qE}, \tag{3.2}$$

where q is the charge of the particle and m is the mass.

Based on this derivation, the turn-around time can be minimized by increasing the electric field. If two ions start at different positions, however, they will have different potentials in a high electric field, leading to a broader kinetic energy spread in the flight tube and reducing the effectiveness of the reflectron. Optimizing the mass resolution thus requires a tradeoff between large kinetic energy distributions at high repeller voltages, caused by a wide range of initial ion positions, and long turn-around times at low repeller voltages, caused by a wide range of initial ion velocities.

3.2.2 Potential Energy

As a first approximation, it is helpful to consider particles that are distributed in space but have zero velocity. Under this assumption, only the initial potential energy must be taken into account and the kinetic energy can be neglected. This assumption is valid when the differences in initial potential energy due to position, typically under an electric field of 60 to 160 V/mm with a range of 15 mm, is small relative to the differences in initial kinetic energy. Although the experimental results suggest that this assumption does not hold, this analysis provides a useful starting point for thinking about the system.

If an electric field is used to accelerate the ions into the flight tube, the velocities of the ions upon entering the mass spectrometer will depend on their initial potential energies. Within a static electric field, the potential energy of the ion is determined by its location at the time the field is established. If the electric field is fairly linear, as shown in Fig. 3.9, the potential of an ion will be proportional to its distance between the two electrodes. If the two repellers in Fig. 3.9 are separated by 15 mm, for example, an ion 5 mm from the right repeller (NEG) would have a potential energy of 300 eV. The direct correspondence between position and potential energy is an added bonus of ensuring a linear electric field between the repellers, which was described in Sec. 2.4.

The relation between position and potential energy is especially interesting in light of the fact that the reflectron can be adjusted to provide upper and lower bounds for the ion energy, as shown in Fig. 3.10. If the energy of the ion exceeds the upper voltage of the reflectron (R2), it will pass right through and hit the wall at the end of the flight tube. If the energy is below the lower voltage (R1), the ion will be broadly distributed in time, as will be shown in Sec. 3.2.4, such that it may not reach to the detector. The result is that the reflectron voltages can, to some extent, be used to select ions based on their initial position between the repellers. And, if the initial kinetic energy of the ions is much less than the potential energy imparted by the electric field, it would be possible to reconstruct the spatial profile of the plume in the lateral direction by scanning the reflectron voltages over a range of potentials.

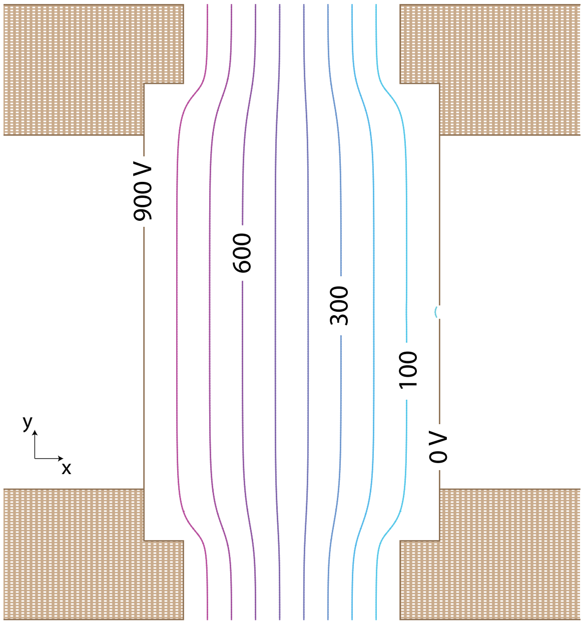

Fig. 3.9 Since the electric field between the two repellers is very close to linear, the potential energy of the ion is almost exactly proportional to its distance between the plates. By using the reflectron to filter out specific energies, ions can be selected from several ranges of positions within the plume. If kinetic energy can be neglected, scanning the isotope content over a range of potential energies would give the spatial profile of the plume in the x direction, orthogonal to the direction of the plume.

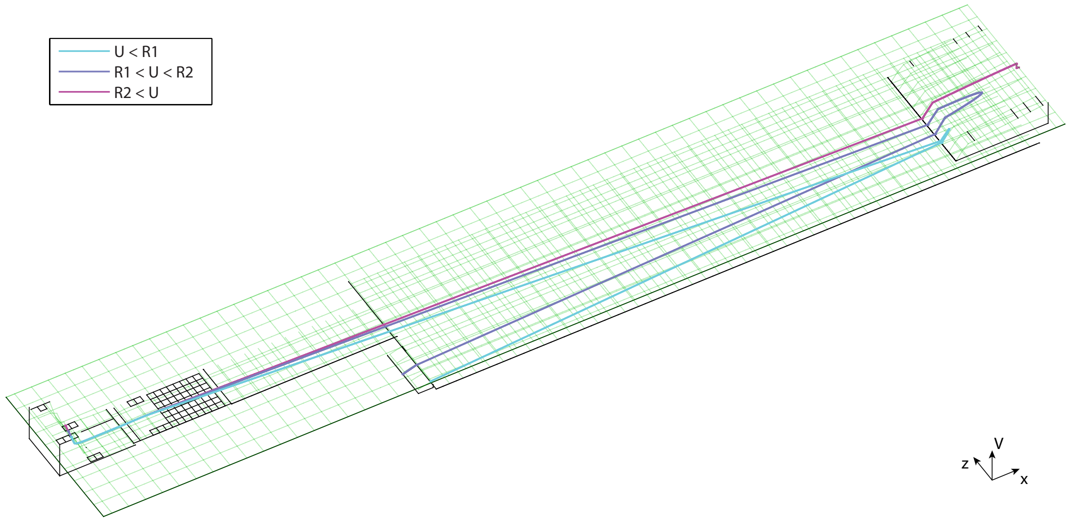

(a) Simulated ion trajectories on the potential surface with initial ion potential less than R1, in between R1 and R2, and greater than R2.

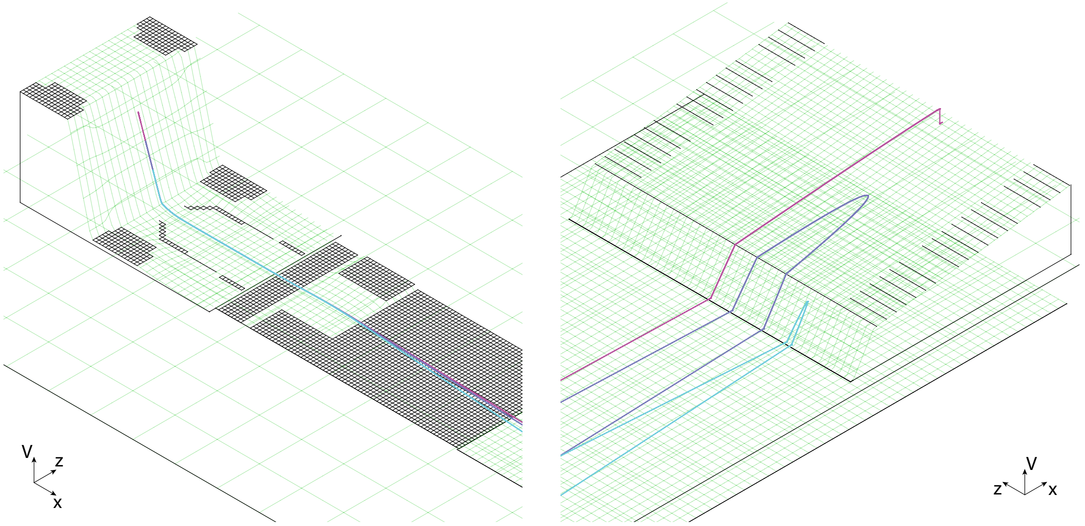

(b) From the repellers through the deflectors.

(c) Ion trajectories at the reflectron.

Fig. 3.10 The reflectron effectively serves as an energy filter for ions in the flight tube. The repeller voltages are set at 1200 and -1200 V, and the reflectron voltages at 347 and -347 V in this simulation. As shown in (a), ions that have an initial potential above 347 V will simply pass through the reflectron and collide with the end of the tube. Those with potentials between 347 and -347 V will make it to the second inclined potential surface of the reflectron and will then be directed back toward the detector. Ions with a voltage potential below -347 V will not be rejected from the system outright, but their lower velocities will cause them to be deflected more by the deflectors (b), potentially into the walls of the flight tube. In addition, since their potential energy will not allow them past the first incline in the reflectron (c), their times-of-flight will be spread out, as shown in Fig. 3.13(b), rather than compressed.

3.2.3 Kinetic Energy

With electric fields of 60 to 160 V/mm, it should be possible to select ions to within 1 mm as long as the maximum initial kinetic energy is below 60 to 160 eV, or the maximum initial velocity in the x direction is 10.4 to 17.0 km/s. The results, however, suggest that this may not be the case for ions from laser ablation under the conditions of this study. Thus, it is necessary to consider the effects of the initial kinetic energy as well.

Since the potential energy from the electric field is converted entirely to kinetic energy before the ions enter the flight tube, it is impossible for the reflectron to distinguish between initial potential energy and initial kinetic energy. The reflectron can only accept or reject ions based on total energy, the sum of the potential energy and the kinetic energy. As a result, the position information and velocity information from an ion is convoluted together and can not be separated by the reflectron. Instead, each set of repeller and reflectron voltages specifies a parameter space of positions and kinetic energies or velocities that may reach the detector. For example, if repeller voltages of 900 and 0 V and reflectron voltages of 720 and -105 V are used, ^{107}Ag ions must have position and kinetic energy combinations within the shaded area in Fig. 3.11(a) and position and velocity combinations within the shaded area in Fig. 3.11(b). In this case, the maximum x position accessible to the mass spectrometer is 4.5 mm, because the electric potential at that point is 720 V. In order for an ion at -4.5 mm to be brought back by the reflectron, however, it must not have any additional kinetic energy in the x direction. Otherwise, it would overshoot the back reflectron electrode (R2) and collide with the wall. Because of this, only ions initially at rest in the x direction can collected at -4.5 mm, and at -4 mm, which corresponds to a potential of 675 V, the magnitude of the velocity in the x direction must be less than 736 m/s. Note that it does not matter whether the velocity is positive or negative, because a negative velocity will be reversed in the electric field between the repellers. Under this set of repeller and reflectron voltages, the closer the x position is to 7.5 mm, the larger the range of velocities the ion can have and still reach the detector. Because the lower reflectron voltage (R1) is less than the negative repeller voltage (NEG), there is no lower limit on the total energy of the ions that can reach the detector.

When the repellers are set to 1200 and -1200 V and the reflectron to 347 and -347 V, ions with a low kinetic energy may be excluded if they are close to the negative repeller (NEG) and have a low potential energy, as shown in Fig. 3.12(a). This configuration is meant to collect the ions with low kinetic energies between -2.2 mm and 2.2 mm, but non-negligible kinetic energies would lead to a more complicated distribution of ions that could make it to the detector. Specifically, those with velocities and positions in the shaded area of Fig. 3.12(b) can be detected. This makes the analysis more challenging, though, because the detected ions can either be low-velocity ions near the center or high-velocity ions closer to the negative electrode on the right. Without independent information about the position or kinetic energy of the ions, all that can be said is that the observed ions fall somewhere within the shaded regions of Fig. 3.12.

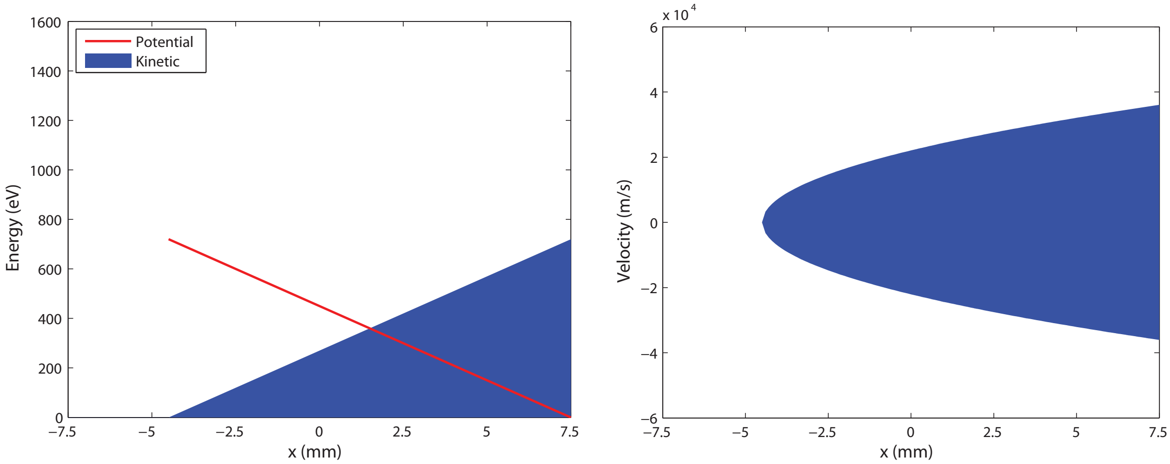

(a) Potential and accessible kinetic energy with the repellers at 900 and 0 V and the reflectron at 720 and -105 V.

(b) Accessible velocity with the repellers at 900 and 0 V and the reflectron at 720 and -105 V.

Fig. 3.11 When the lower reflectron voltage is less than the lower repeller voltage, the ion energy is limited only by the upper reflectron voltage. Since the sum of the potential and kinetic energy has be under 720 V, only ions with low speeds near -4.5 mm can be detected while ions can have a much larger range of velocities near 7.5 mm. As before, all of the ions to the left of -4.5 mm will pass through the reflectron and can not be detected.

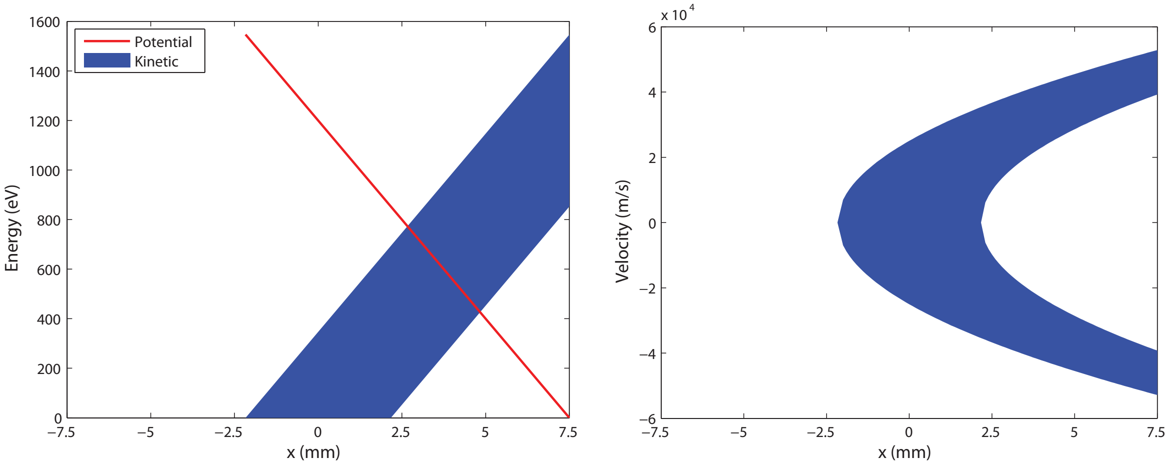

(a) Potential and accessible kinetic energy with the repellers at 1200 and -1200 V and the reflectron at 347 and -347 V.

(b) Accessible velocity with the repellers at 1200 and -1200 V and the reflectron at 347 and -347 V.

Fig. 3.12 Since the lower reflectron voltage (R1) is higher than the negative repeller voltage (NEG), there is a lower limit to the total energy of the detectable ions. The result is that ions with negligible kinetic energy will be collected from the center of the repellers, as well ions with higher kinetic energies closer to the negative repeller on the right (NEG). Without knowledge of the kinetic energy, intensities from this configuration can be difficult to interpret because of the way position and velocity are convoluted in the ion intensities.

3.2.4 *Time-of-Flight*

The main purpose of the reflectron, however, is not to filter ion energies but to minimize the spread in the time-of-flight. If ions originate at the same time and within the same plane perpendicular to the direction of flight, any spread in kinetic energy can be compensated for exactly by a flight path with the quadratic potential $V = ax^2$ [95], where a is an arbitrary constant and x is the distance into the potential field. If the initial kinetic energy is qU, then the kinetic energy at any point within the field is given by

$$\frac{1}{2}mv^2 = qU - qax^2 \tag{3.3}$$

and the time needed to reverse the particle and bring it back to its original position is

$$t = 2\int_0^{x_{max}} \frac{dx}{v} = 2\int_0^{\sqrt{U/a}} \frac{dx}{\sqrt{\frac{2q(U-ax^2)}{m}}} = \pi\sqrt{\frac{m}{2qa}} \tag{3.4}$$

where x_{max} is the maximum distance attained by the particle within the electric field, m is the mass of the ion, q is the charge, and v is the velocity of the particle in the electric field. Note that the kinetic energy term qU does not appear in the final expression for time. It is very difficult to establish such a field in practice, but the same principles can still be used to optimize the voltages in the reflectron to minimize the spread in the time-of-flight. Specifically, the time it takes for an ion with initial energy qU to be accelerated or decelerated from the potential V_1 to V_2 in a linear field is given by

$$t = \frac{v_2 - v_1}{a} \tag{3.5}$$

where

$$v_1 = \sqrt{\frac{2q(U-V_1)}{m}}, \tag{3.6}$$

$$v_2 = \sqrt{\frac{2q(U-V_2)}{m}}, \tag{3.7}$$

$$a = \frac{qE}{m}, \quad \text{and} \tag{3.8}$$

$$E = \frac{V_2 - V_1}{l} \tag{3.9}$$

where l is the length of the linear field between V_1 to V_2. The only region that can not be described by the equation above is the time within the flight tube, which is given by

$$t = \frac{L}{\sqrt{\frac{2q(U-V_L)}{m}}} \tag{3.10}$$

where L is the length of the flight tube not including the reflectron and V_L is the voltage of the liner.

An analytical solution can be found if the reflectron consists of a single potential gradient, but numerical optimization is more practical for a two-stage reflectron. For each set of experimental conditions, the upper and lower reflectron voltages were optimized to minimize the range of flight times for stationary ions distributed between the repellers. The times-of-flight for the optimal values of the two conditions described in 3.2.3 are shown in Fig. 3.13. Under the first configuration in Fig. 3.13(a) with the repellers at 900 and 0 V, the upper reflectron voltage (R2) was set to 720 V in order to include 12 of the 15 mm between the repellers and then the lower reflectron voltage (R1) was varied to minimize the peak width of the two isotopes. The second configuration in Fig. 3.13(b) had the repellers at 1200 and -1200 V, and the upper and lower reflectron voltages were kept the same magnitude but opposite signs in order to capture the center of the plume. While Fig. 3.13(b) shows a large amount of overlap between the two curves, the peaks are separated reasonably well in the actual results, suggesting that most of the ions observed originate from an even smaller range than the -2.2 to 2.2 mm window accepted by the reflectron. This plot also shows how ions with a potential energy below the lower reflectron voltage are rejected from the system, not by being excluding per se but by having their time-of-flight broadly spread out toward longer times. Not only does this minimize the signal intensity for these low-energy ions, but their slow velocity is also like to cause them to be deflected past the detector, as shown in Fig. 3.10(a).

As before, the analysis above was performed based on the potential energy derived from the position of the ions and did not take into account initial kinetic energy at all. Since the ion positions must lie within a narrow range while the variation in kinetic energy is not known, optimization over ion positions alone was the most straightforward. While this neglects a fairly important factor in the time-of-flight, the parameters derived from optimizing the potential energy spread alone generally worked very well in discriminating the two isotopes and further adjustment to the parameters tended to result in worse resolution. In addition, the relatively small widths of the isotope peaks in the voltage traces suggest a fairly narrow distribution of kinetic energies.

After this optimization has been performed, however, possible initial kinetic energies can be added back into the analysis in order to calculate the full range of the time-of-flight for a given configuration, as shown in Fig. 3.14. Figs. 3.14(a) and 3.14(c) show the possible times-of-flight for the full range of initial velocities of ^{107}Ag, and Figs. 3.14(b) and 3.14(d) include both ^{107}Ag and ^{109}Ag. As shown in Fig. 3.14(a), more negative velocities lead to longer times-of-flight, while the effect of position is more variable due to the optimization from Fig. 3.13(a). In Fig. 3.14(c), time-of-flight similarly decreases with velocity, although position also has a large effect under these conditions. Figs. 3.14(b) and 3.14(d) show a broad overlap in the times-of-flight between the two isotopes, implying that they could not be resolved if ions from the full range of positions and velocities were indeed being recorded. Since the peaks observed are fairly sharp, the ions must be drawn from a relatively small parameter space within the range of allowable positions and velocities in

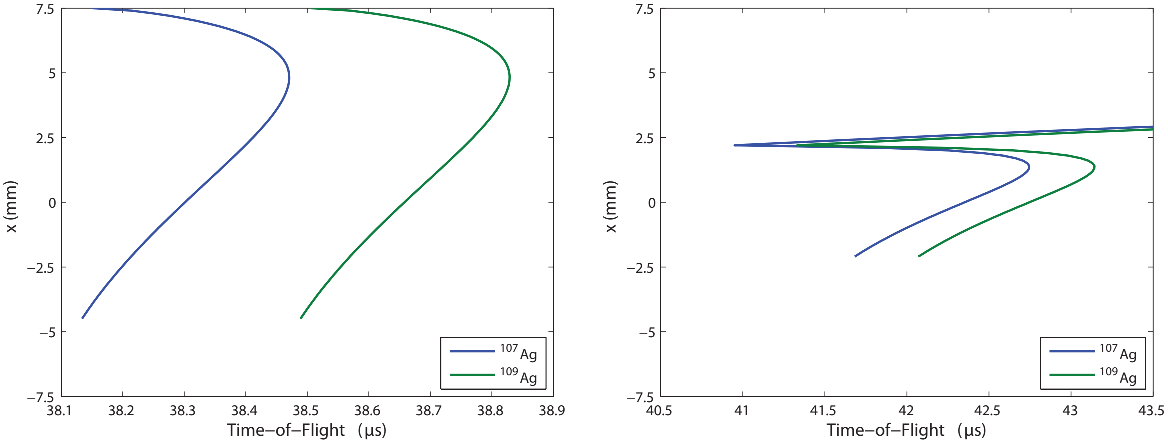

(a) Time-of-flight for the repellers at 900 and 0 V and the reflectron at 720 and -105 V.

(b) Time-of-flight for the repellers at 1200 and -1200 V and the reflectron at 347 and -347 V.

Fig. 3.13 The reflectron voltages were selected by minimizing the range of time over which stationary ions would arrive at the detector. With the repellers set to 900 and 0 V (a), the upper reflectron voltage was set at 720 V and the lower reflectron voltage optimized for time-of-flight. With the repellers set to 1200 and -1200 V (b), the upper and lower reflectron voltages were optimized with the same positive and negative voltages. In this condition, the ions with an x position above 2.2 mm are distributed broadly in time and can be neglected .

Figs. 3.11(b) and 3.12(b) respectively.

If the ions have a much smaller range of positions and velocities than shown in Fig. 3.14, several implications follow. First, if the actual position and velocity distributions were known, it might be possible to optimize the repellers and reflectron to produce even sharper peaks and higher mass resolution. Second, it may be possible to use the time-of-flight spectra themselves to determine the position and velocity distribution. Fig. 3.15, for example, shows the time-of-flight increasing with delay time for the repellers at 900 and 0 V, and this trend appears for every condition observed.

Because the time-of-flight convolutes position and velocity, it is difficult to tell if the shift in the spectra of Fig. 3.15 is due to changes in position or velocity. For comparison, simulated traces have been generated in Fig. 3.15 for ions with no velocity and a normal distribution of positions and ions at a single position with a normal distribution of velocities. Time-of-flight tends to increase closer to the negative repeller, as shown in Fig. 3.16(a), and to decrease with velocity, as shown in Fig. 3.16(b). The increase in time-of-flight with delay time in Fig. 3.15 is due either to the ion distribution shifting in the positive x direction or decreasing in velocity or both. Both explanations are plausible, because the ions should spread out closer to the repellers as the plume expands and the ions observed at later times probably have lower velocities. Because the two cases produce similar results, it is difficult to disentangle the contributions of velocity and position. Given a model for de-

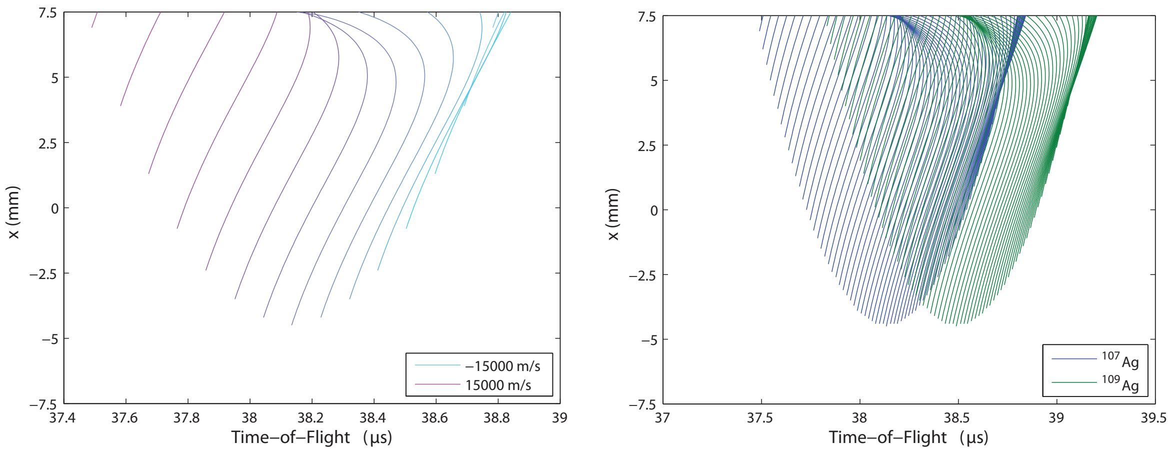

(a) Full time-of-flight range for repellers at 900 and 0 V.

(b) Time-of-flight range with both isotopes for repellers at 900 and 0 V.

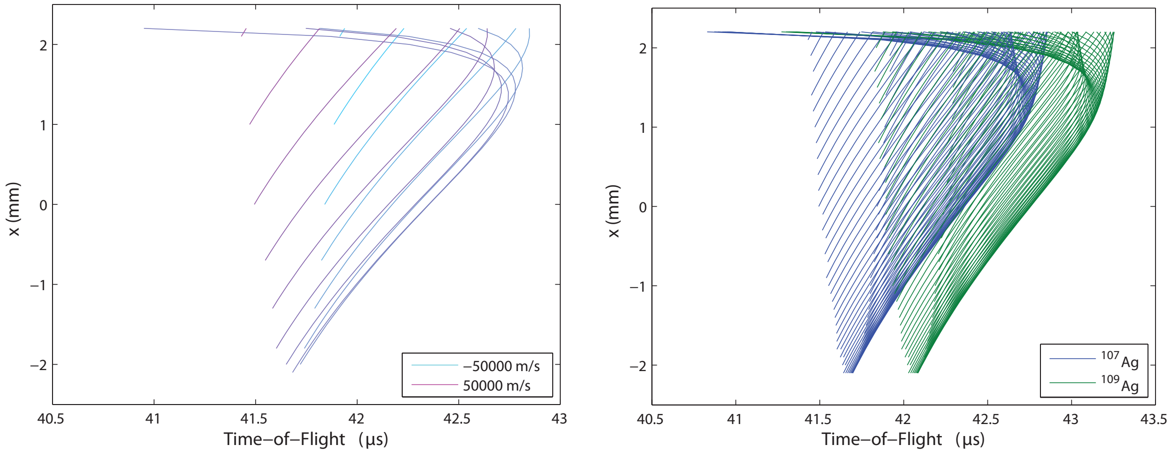

(c) Full time-of-flight range for repellers at 1200 and -1200 V.

(d) Time-of-flight range with both isotopes for repellers at 900 and 0 V.

Fig. 3.14 The full range of the time-of-flight is plotted for the two configurations for ^{107}Ag alone in (a) and (c) and for ^{107}Ag and ^{109}Ag together in (b) and (d). (a) and (c) show that time-of-flight decreases with velocity, and (b) and (d) show a significant overlap in the ions from the two isotopes were they to cover the full position and velocity distribution. In (c) and (d), the times-of-flight for positions above 2.2 mm have been removed for clarity, especially since they are broadly dispersed and unlikely to reach the detector.

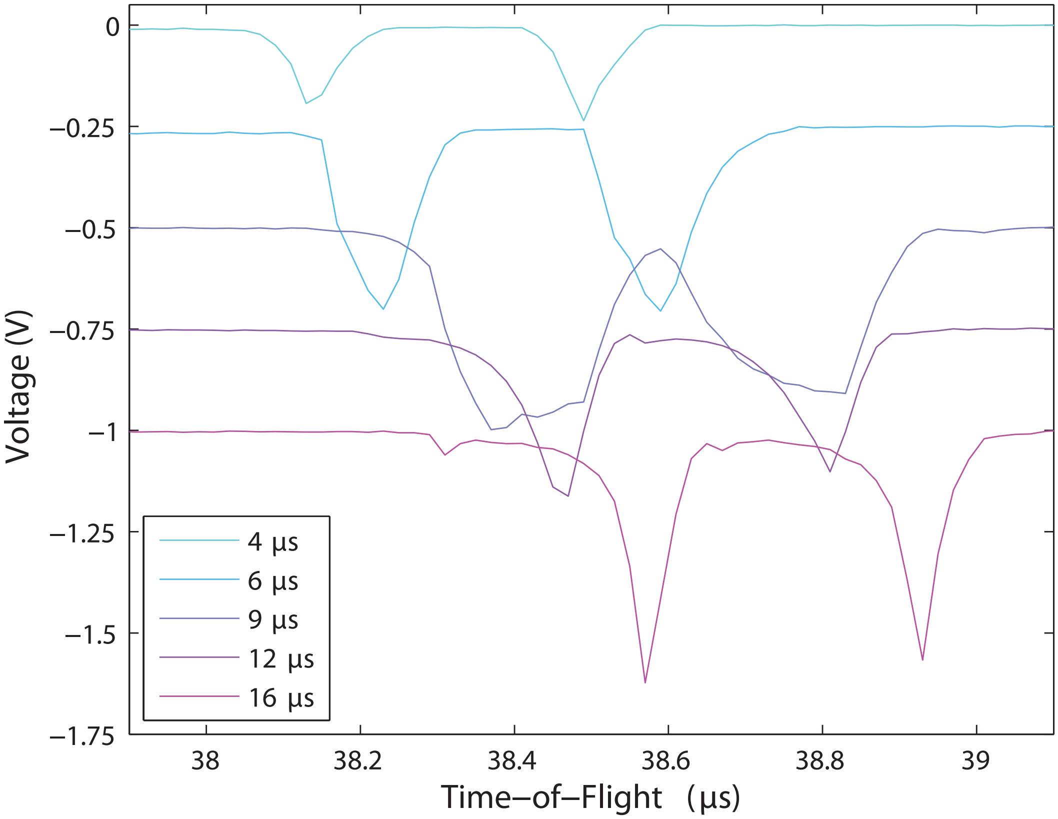

Fig. 3.15 Voltage traces for delays of 4, 6, 9, 12, and 16 μs. The time-of-flight increases with delay time under every set of repeller and reflectron voltages studied, suggesting an increase in x position or a decrease in velocity or both with time.

scribing plume propagation, however, ion traces could be simulated based on the proposed ion distribution for comparison with experimental results.

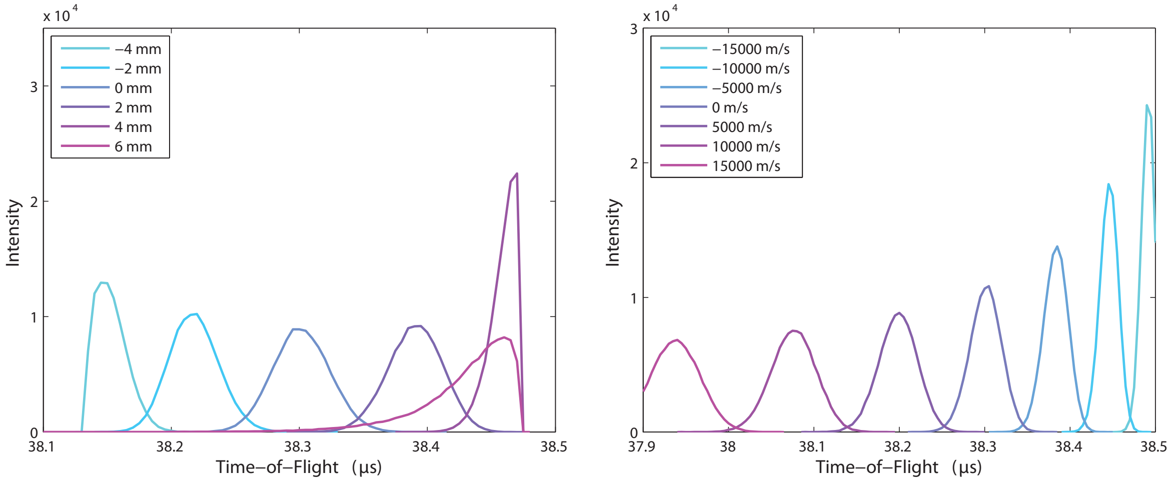

(a) Time-of-flight with ion position. A normal distribution with a standard deviation of 0.5 mm was used for the position.

(b) Time-of-flight with ion velocity. A normal distribution with a standard deviation of 1000 m/s was used for the velocity.

Fig. 3.16 Simulated voltage traces have been generated for ions with a distribution of positions at a single velocity (a) and with a distribution of velocities at a single position (b). The time-of-flight decreases consistently with velocity (b) and mostly increases with position, but an x position very close to the negative repeller will lead to a broader peak shifted slightly back toward shorter times-of-flight (a).

Chapter 4

Results and Discussion

The results are divided into three sections, based on the repeller and reflectron parameters used and the kind of experiments conducted. Full temporal and spatial profiles of the laser plume were obtained for all of the experiments in Sec. 4.1. The reflectron conditions were selected to sample the entire plume in Sec. 4.1.1, the plume center in Sec. 4.1.2, and the near side of the plume in Sec. 4.1.3. Although measurements of the entire plume showed significant changes in the isotope ratio, data from the plume center and the plume side did not. To find the parts of the plume containing an uneven distribution of isotopes, the repeller and reflectron voltages were tuned to focus on different lateral sections of the plume in Sec. 4.2. First, the central region being sampled was broadened in Sec. 4.2.1. Progressively larger sections were then measured starting from the near side of the plume and extending toward the far side in Sec. 4.2.2. Finally the voltages were configured in Sec. 4.2.3 such that a 7-mm window was stepped across the width of the plume. To minimize the time needed for these experiments, only temporal profiles were obtained in Sec. 4.2. The results showed that sampling ions from the far side of the plume yields significant changes in the isotope ratio, while the isotope distribution remains relatively close to the natural abundance when sampling ions from the near side of the plume. Sec. 4.3 concludes with the temporal and spatial profile of the ions from the far side, which represent the conditions under which the greatest deviation from the natural abundance ratio is observed.

4.1 Plume Profile

In the first experiment, the isotope content of the plume was measured in space and time for ions sampled from almost the full width of the plume, as shown in Table 2. The results showed the heavier ^{109}Ag moving ahead of the lighter ^{107}Ag, which was very unexpected because ions with less mass have higher velocities when they are given the same initial energy. A possible explanation for this counterintuitive phenomenon was that the space charge near the center of the plume was forcing the lighter isotopes from the plume center toward the periphery, leaving the heavier isotopes less affected [81, 82]. If the lighter isotopes have a higher lateral velocity while the heavier isotopes have a higher forward velocity, ^{109}Ag might appear in front of ^{107}Ag, as observed in the mass spectrometry. To test this, the repellers and the reflectron were configured to collect ions from the center of the plume as well as from the side using the parameters in Table 2. If this hypothesis was correct, ions from the plume center would likely show an enhanced effect with an even greater proportion of ^{109}Ag, while ions from the side of the plume might include more ^{107}Ag. Little change to the isotope ratio was observed under either of these conditions, however, suggesting that a more detailed study of the plume's lateral profile was needed.

	Repellers (V)		Reflectron (V)		Deflector (V)	Range (mm)	
Region	Pos	Neg	R2	R1	XY2	Far	Near
Entire Plume	900	0	720	-105	-1201	-4.5	7.5
Plume Center	1200	-1200	347	-347	-1220	-2.17	2.17
Plume Side	1200	0	360	-287	-1214	3.0	7.5

Table 2 Instrument parameters and sampling range for the entire plume, the plume center, and the plume side

4.1.1 Entire Plume

For all of the experiments in Sec. 4.1, measurements were taken up to 40 µs at distances from 0 to 16 mm every 2 mm. During the experiments, successive observations were taken at different times for a single distance, as shown in Figs. 4.1 and 4.2, before moving the target to a different distance, but it was sometimes more intuitive to plot the data at a single time over different distances, as in Figs. 4.3 and 4.4.

Fig. 4.1 shows the typical temporal profile of the plume at a distance relatively close to the target surface. The main features of this plot are the two ion peaks, a fairly sharp distribution of fast ions, centered around 5 µs, and a broader distribution of slower ions, centered around 19 µs. At a distance of 4 mm, the fast ions not only appear early in time but pass through this section of the plume completely within just a couple microseconds. The slow ions, on the other hand, emerge and disappear over tens of microseconds and never reach the peak concentration of the fast ions. Since the slow group has a lower and broader distribution of velocities, they are more likely to result from purely thermal phenomena, such as melting and evaporation, compared with the fast group, whose velocities appear to be more forward-peaked.

Observations at the first two times in Fig. 4.1 should be neglected because of the early ion effect, as described in Sec. 2.2.2. Because these ions create interference at earlier times-of-flight, they tend to have a disporportionate effect on the lighter isotope, artificially increasing the intensity and fraction of ^{107}Ag. In particular, the decrease in signal between 1 and 2 μs even before the first peak, suggests that the data from these two points include a significant number of early ions and can not be regarded as reliable indicators of the isotope content. Downward trends in the ^{107}Ag fraction at early times, on the other hand, can not be caused by early ions and may even have to overcome this effect and, thus, constitute real phenomena. Note also that the error bars for the isotope fraction may be less than that of the individual isotope intensities, if these intensities are correlated from shot to shot.

Disregarding the first two points, the fraction of ^{107}Ag starts off very low at 0.34 before increasing to 0.55 at 6 μs, reaching a peak of 0.57 at 10 μs, dropping back down to 0.51 at 20 μs, and fluctuating around the natural abundance ratio of 0.52 as the plume disappears. The high proportion of ^{109}Ag in the first couple microseconds can be attributed to the fact that the heavier isotope peak is observed just slightly ahead of the lighter isotopes in time. Since the ^{109}Ag peak is shifted just a fraction of a microsecond earlier than the ^{107}Ag peak, the fraction of ^{107}Ag is much lower than the natural abundance at 3 μs but rises rapidly as both isotopes increase in signal. Similarly, the falling edge of the ^{107}Ag peak lags that of the ^{109}Ag. As a result, the ^{107}Ag fraction increases above the natural abundance after the fast ion peak of 5 μs. This skew in the isotope ratio is not as dramatic, however, because of a more gradual decrease in the ion intensities at lower concentrations, likely due to overlap with the rising edge of the slow ion distribution. The slow ion peak is itself generally much closer to the natural abundance ratio. Within this distribution, ^{107}Ag is slightly overrepresented at both the rising and falling edges of the peak. This could be consistent with a space charge explanation of the isotope distribution in that the lighter isotopes are being pushed both slightly ahead and slightly behind the peak center of the slow ions. At even later times after 30 μs, the fraction of ^{107}Ag appears to return to the natural abundance ratio, at least within the increasing uncertainty of the rapidly diminishing ion intensities.

The isotope content of the plume was measured over a range of distances, and Fig. 4.2 includes the results at 0, 2, 4, 8, 12, and 16 mm. Both the fast and slow ion groups shift later in time at larger distances away from the target, which is appropriate for ions with a forward velocity. At 0 mm near the surface, the fast peak is centered at 2 μs, which increases to 5 μs at 4 mm and 10 μs at 16 mm. The slow ion peak appears at 7 μs at 0 mm, 13 μs at 2 mm, and 19 μs at 4 mm, and the distribution spreads out broadly in time at greater distances. The fast ion peak is fairly narrow below 8 mm but exhibits a broad shoulder toward later times in temporal profiles at longer distances, such as in Figs. 4.2(e) and 4.2(f). If the shoulder in the fast peak results from the slow ions spreading toward early times at longer distances, this would imply that these ions are moving back toward the target with time.

As described earlier for Fig. 4.1, excluding the spurious data points from the early ions, the^{107}Ag fraction in Fig. 4.2 tends to start well below the natural abundance due to a slight shift toward earlier times on the part of the fast ^{109}Ag peak. This trend is fairly distinct at distances below 8 mm but, although still apparent, becomes somewhat muddled by the early ions above 8 mm. The ^{107}Ag fraction increases with the fast peak and reaches its maximum just above the natural abundance, typically near the falling edge of the fast peak.

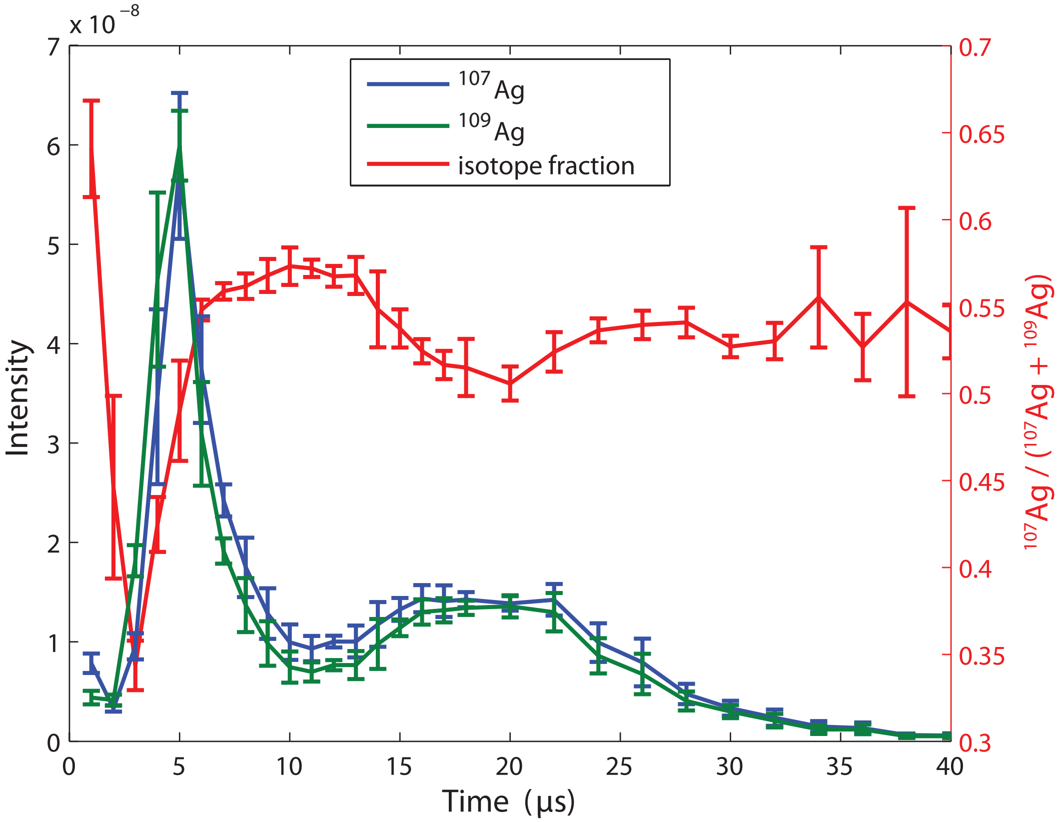

Fig. 4.1 The isotope content was measured across the entire laser plume over different delay times 4 mm from the target surface. The amount of ^{107}Ag and ^{109}Ag are plotted in blue and green respectively, and the fraction of ^{107}Ag is in red. Close to the target, two distinct distributions of ions are observed: a fast group at early times centered around 5 μs and a slower group around 19 μs. Within the fast ions, ^{109}Ag leads ^{107}Ag by a fraction of a microsecond, as evidenced by the sharp dip in the ^{107}Ag composition early on. The slow ions do not show as dramatic a shift in the distribution.

Note that the sharp increase in the ^{107}Ag fraction in 4.2(f), while partly due to the lighter isotope catching up to the heavier isotope, is somewhat unreliable due to poor resolution in the time-of-flight, which may have led to overestimating the amount of ^{107}Ag. Finally, there tends to be a dip in the ^{107}Ag composition near the slow peak, with the ^{107}Ag fraction rising to either side. While the isotope ratio typically settles toward the natural abundance at later times, the proportion of ^{107}Ag remains somewhat higher at 40 μs at 8 mm and 12 mm, potentially a result of the lighter isotopes spreading out faster than the heavier isotopes.

Plotting ion intensity with distance instead of time, as in Figs. 4.3 and 4.4, provides snapshots of the ablation plume in time. The error bars and the isotope fraction have been omitted from these plots for clarity. Fig. 4.3 focuses on the fast peak and shows how the ion

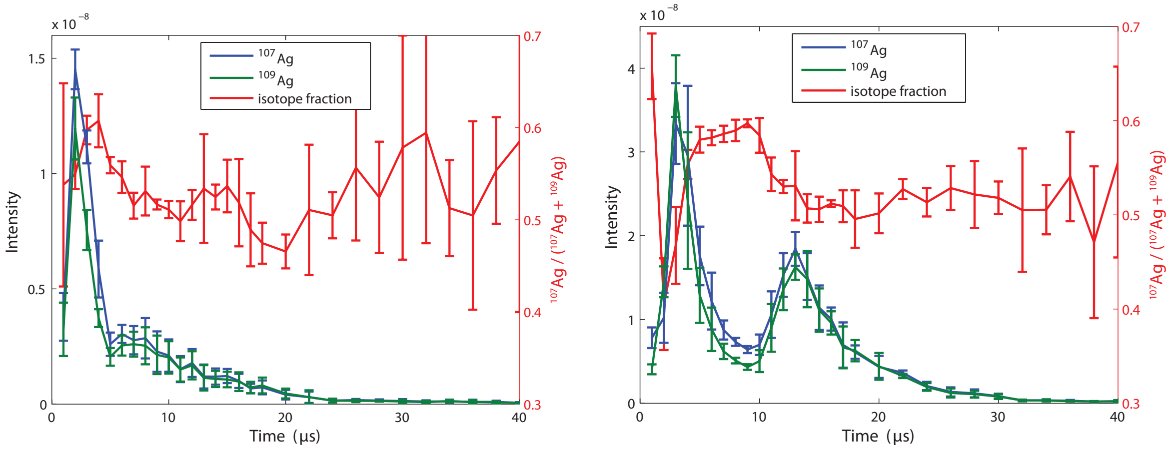

(a) Isotope content with time at 0 mm. **(b)** Isotope content at 2 mm.

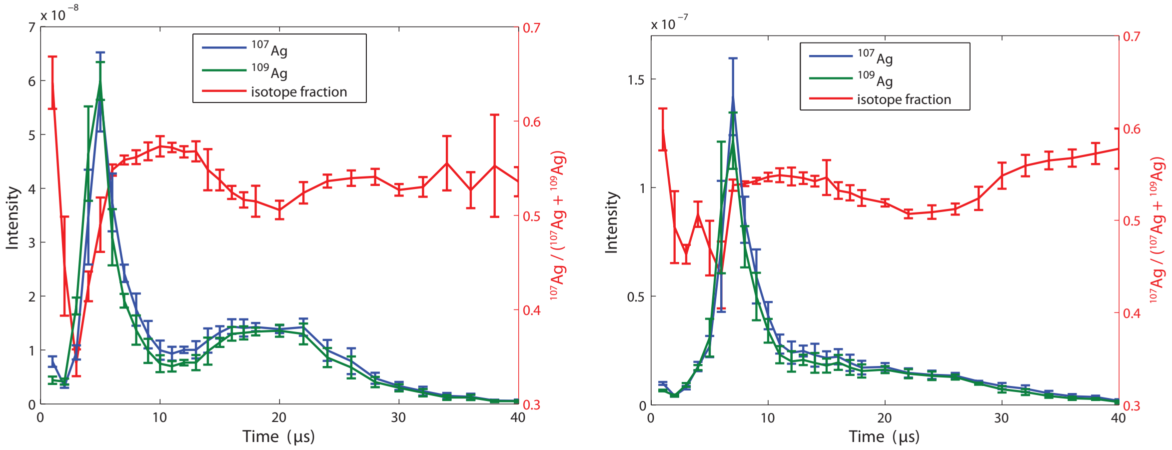

(c) At 4 mm. **(d)** At 8 mm.

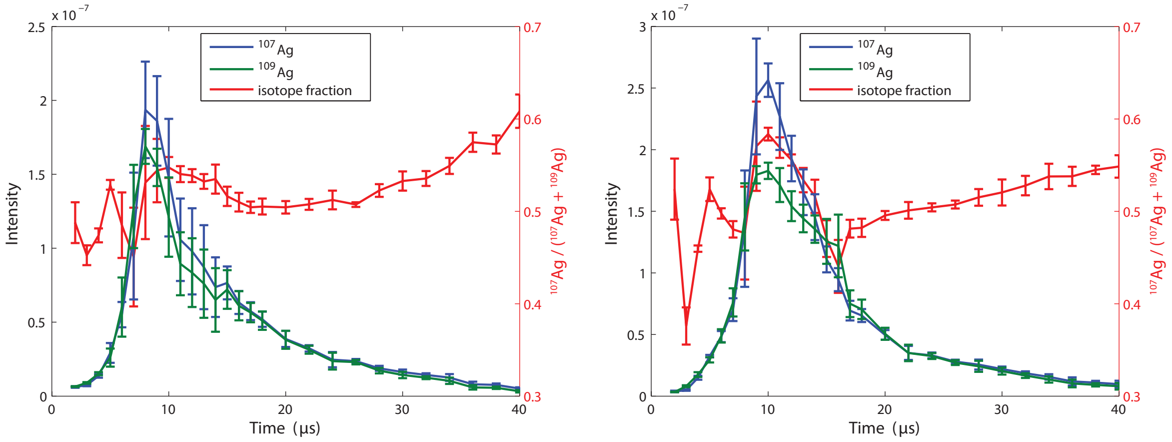

(e) At 12 mm. **(f)** At 16 mm.

Fig. 4.2 The isotope content was measured across the entire plume over a range of times at different distances from the target surface. Temporal profiles from shorter distances show the fast and slow ion distributions. The relative decrease in ^{107}Ag at early times persists and is due to the fast ^{107}Ag peak being shifted slightly later in time relative to the ^{109}Ag.

distribution increases in magnitude as it leaves the target surface. The graphs also confirm that the fast ^{109}Ag peak is centered farther away from the target and leads the ^{107}Ag peak in both space and time.

Fig. 4.4 focuses on the timescale over which the slow peak develops near the target. The slower shoulder of the fast ion peak at larger distances is also included in these graphs. The slow ions at short distances in Fig. 4.4 have a little less than half the intensity of the fast ions at short distances in Figs 4.3(a) and 4.3(a) and much less intensity than the fast ions at larger distances, so the peak is relatively subtle in the spatial profile. It is not clear from the graphs whether these slow ions originate from the target surface or from backflow of the fast ion distribution. The fast ions in Fig. 4.4 seem to have slowed their forward progress compared to earlier times and may even be spreading back toward the target with time, which accounts for the broad shoulder in Figs 4.2(e) and 4.2(f). The larger ^{107}Ag intensity in Fig. 4.4(a) may be due to the falling edge of the fast peak or may be an artifact of poor mass resolution at large distances.

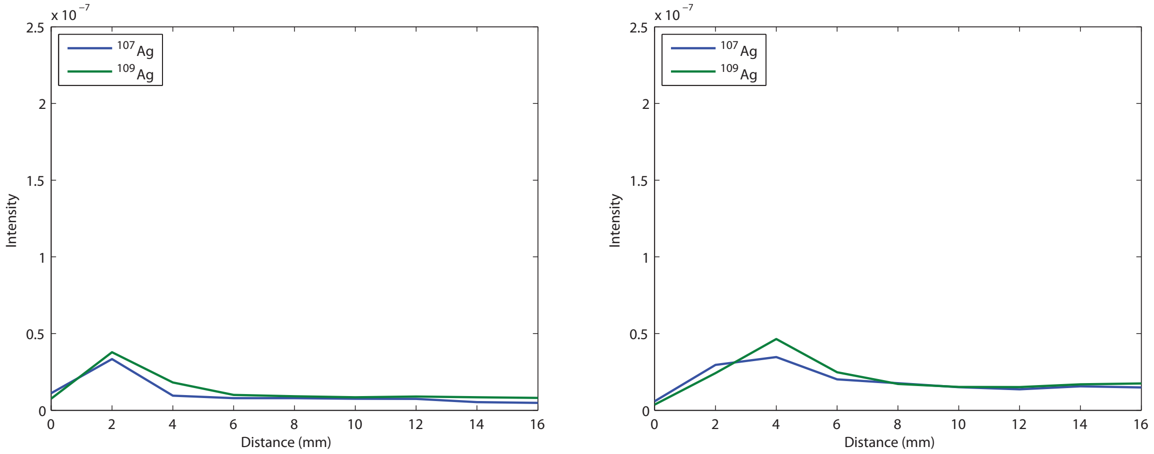

(a) Isotope content with distance at 3 μs. **(b)** Isotope content at 4 μs.

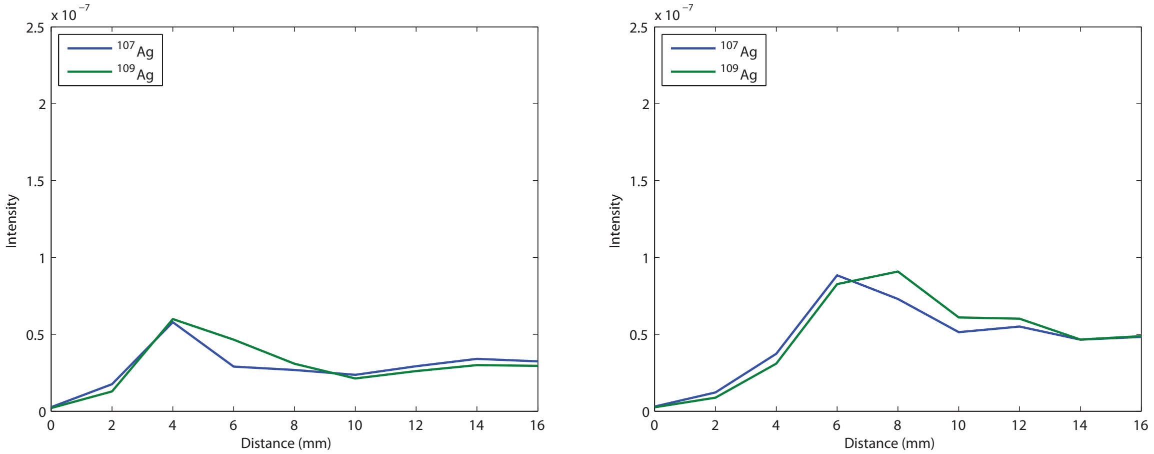

(c) At 5 μs. **(d)** At 6 μs.

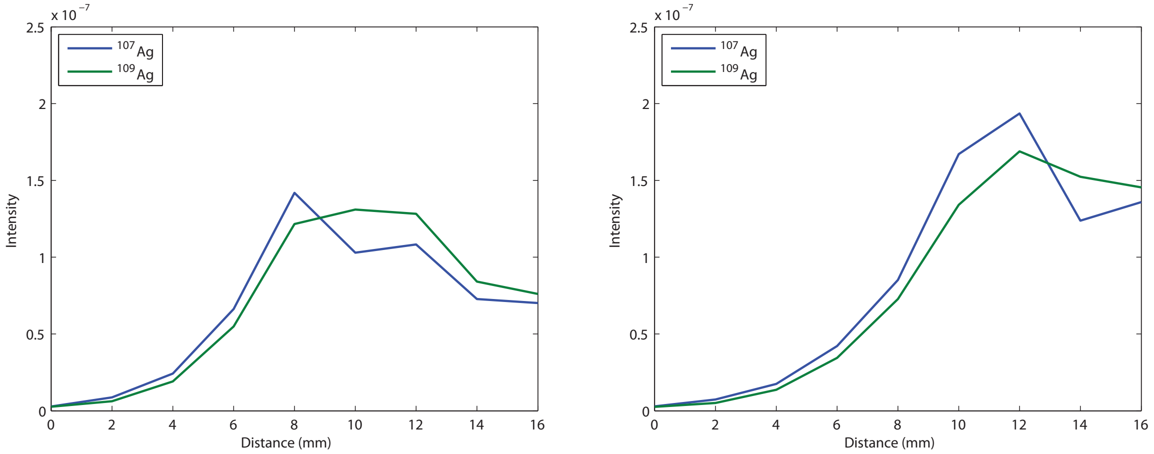

(e) At 7 μs. **(f)** At 8 μs.

Fig. 4.3 The isotope content is plotted against distance from 3 to 8 μs. Among these fast ions, the ^{109}Ag distribution leads the ^{107}Ag group in space and time.

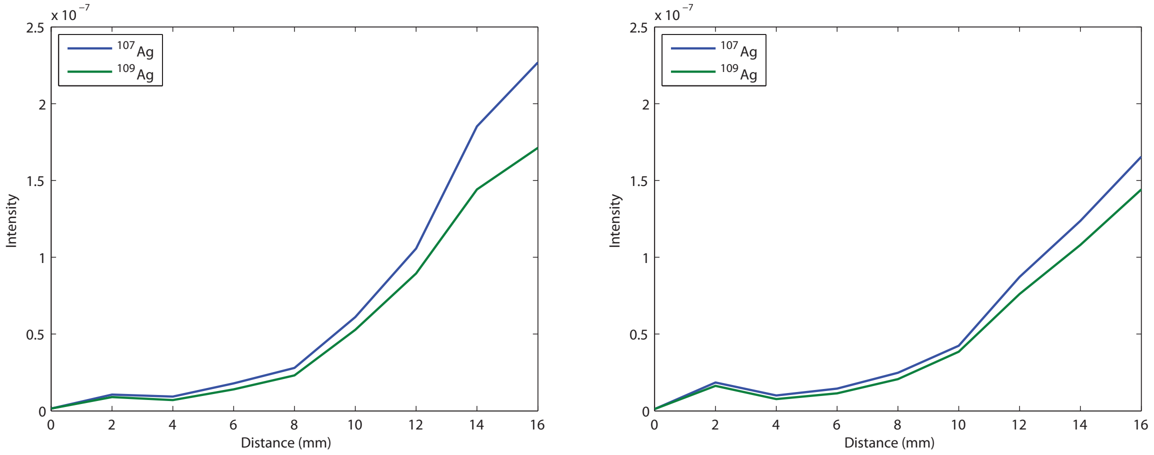

(a) Isotope content with distance at 11 µs. **(b)** Isotope content at 13 µs.

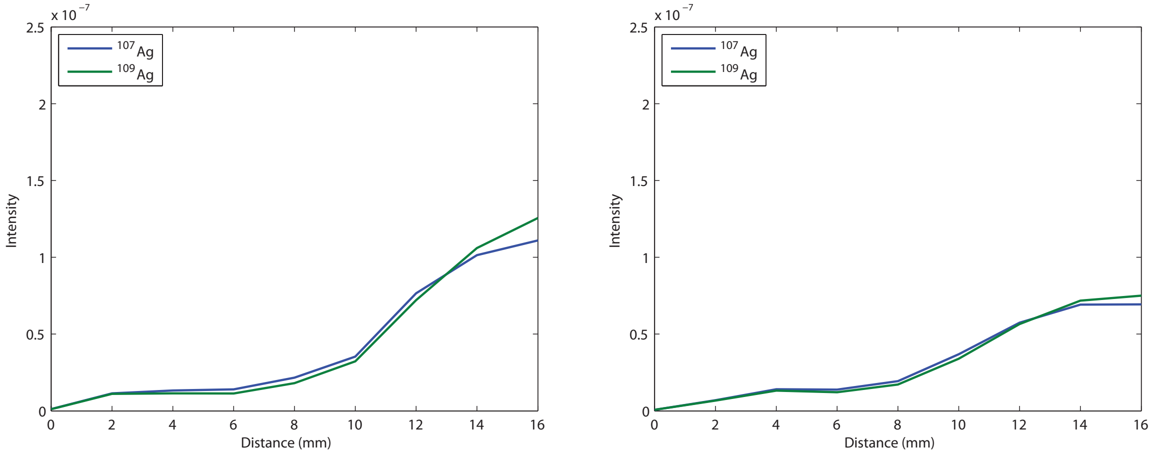

(c) At 15 µs. **(d)** At 17 µs.

Fig. 4.4 The isotope content is plotted against distance from 11 to 17 µs. The slow ions near the target have a much lower intensity than the fast ions shown to the right. At this point, the fast peak is no longer moving ahead as rapidly with time.

4.1.2 Plume Center

That ^{109}Ag appears ahead of ^{107}Ag in both time and space was very unexpected, but could be caused by the lighter isotopes being forced off-axis while the heavier isotopes remained near the center of the plume. In this case, ions along the center of the plume might include a larger proportion of ^{109}Ag while those near the side might contain more ^{107}Ag. To test this hypothesis, the repeller and reflectron voltages were configured to sample ions from the center of the plume in one experiment and ions from the side in the another.

Fig. 4.5 shows the isotope content at different distances as a function of time. Due to the reduced signal from sampling a smaller part of the plume, the early ions caused a proportionally greater degree of interference and the isotope ratios tended to be less reliable before 8 or 9 µs, especially farther away from the target. As mentioned previously, sharp increases in the fraction of ^{107}Ag at early times are almost certainly a product of this artifact, especially where the lighter isotope deviates from the curve of the peak in Figs. 4.5(c), 4.5(d), and 4.5(e).

Because the early ions interfere with the signal at very short timescales, it is possible that an additional fast ion peak may have been clipped entirely from these results. Nevertheless, based on the graphs in Fig. 4.5, it is clear that the subset of ions recorded in this experiment behave very differently from those sampled across the whole plume. The two ion distributions in Figs. 4.5(b) and 4.5(c) are relatively slow, have small ion intensities, and appear to merge into a single peak at around 6 mm in 4.5(d). As before, at longer distances only a single ion distribution remains, in this case with a small shoulder toward later times, but these peaks are also centered later in time than those for the entire plume in Fig. 4.2. In fact, the ions plotted in Fig. 4.5 appears to have characteristics and intensity similar to the slow ion distributions in Fig. 4.2 and may even have comprised part of that group in the earlier measurements.

The ^{107}Ag fraction does not change dramatically in Fig. 4.5, dipping only slightly toward earlier times and rising slightly toward later times near the target. This is consistent with the explanation that these ions are the same as the slow distribution from the entire plume and suggests that even in this group ^{109}Ag is just a little faster than ^{107}Ag. In the temporal profile of the whole plume, the decrease in the fraction of ^{107}Ag may have been pushed slightly later by the falling edge of the fast ^{107}Ag peak.

The spatial profile of the isotope content is shown in Fig. 4.6, and it is difficult to detect any major differences in the distribution of the two isotopes. The behavior of the ions in general, however, does differ significantly from that of the entire plume and is more similar to the shoulder of the fast ions from Fig. 4.4 in terms of how they increase in concentration and then slowly fade away from the surface rather than moving steadily forward like the fast ions in Fig. 4.3.

4.1.3 Plume Side

Based on the premise that space charge is pushing the lighter isotopes to the side while keeping the heavier isotopes near the center, configuring the system for sampling ions

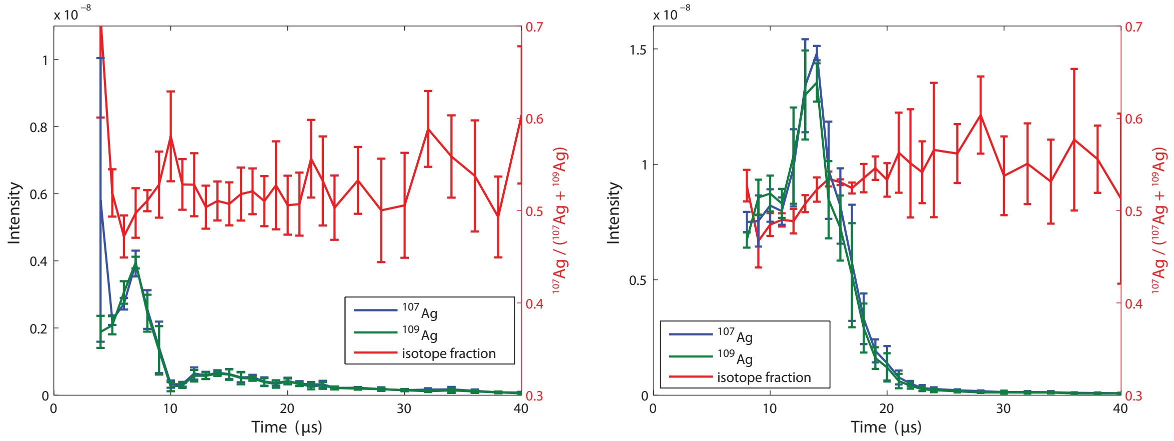

(a) Isotope content with time at 0 mm.

(b) Isotope content at 2 mm.

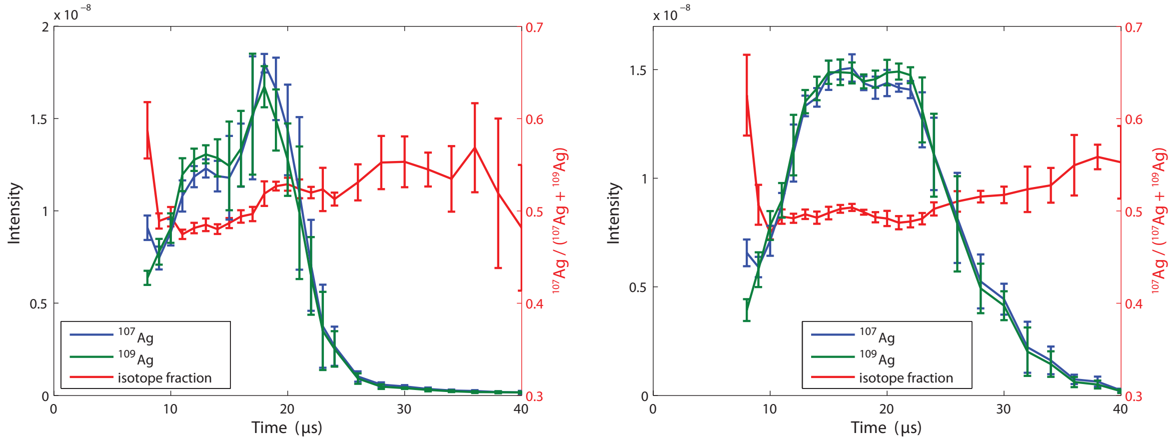

(c) At 4 mm.

(d) At 6 mm.

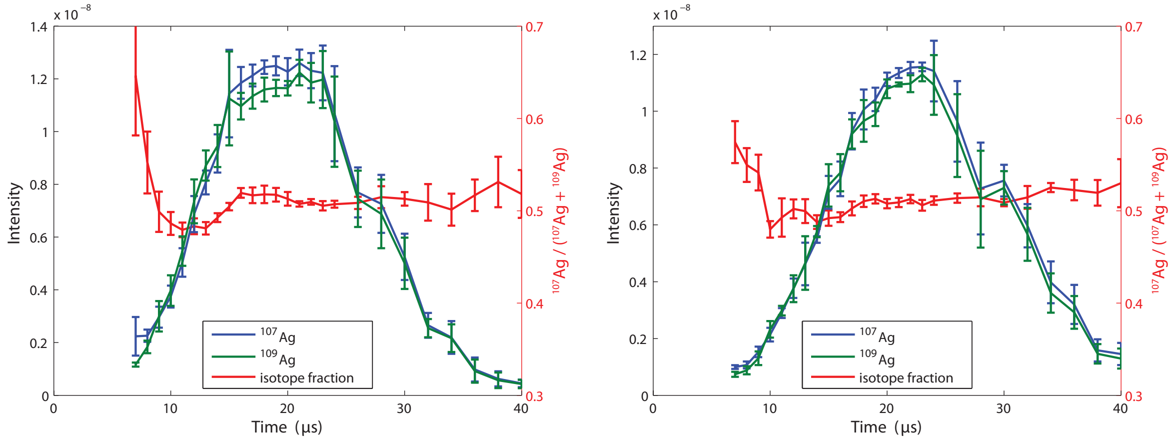

(e) At 10 mm.

(f) At 16 mm.

Fig. 4.5 The isotope content was measured near the center of the plume over a range of times at different distances from the target surface. The ions observed under this configuration appear to correspond to the slow distribution from the entire plume, with the ^{107}Ag fraction dipping only slightly near the rising edge of the ion peak.

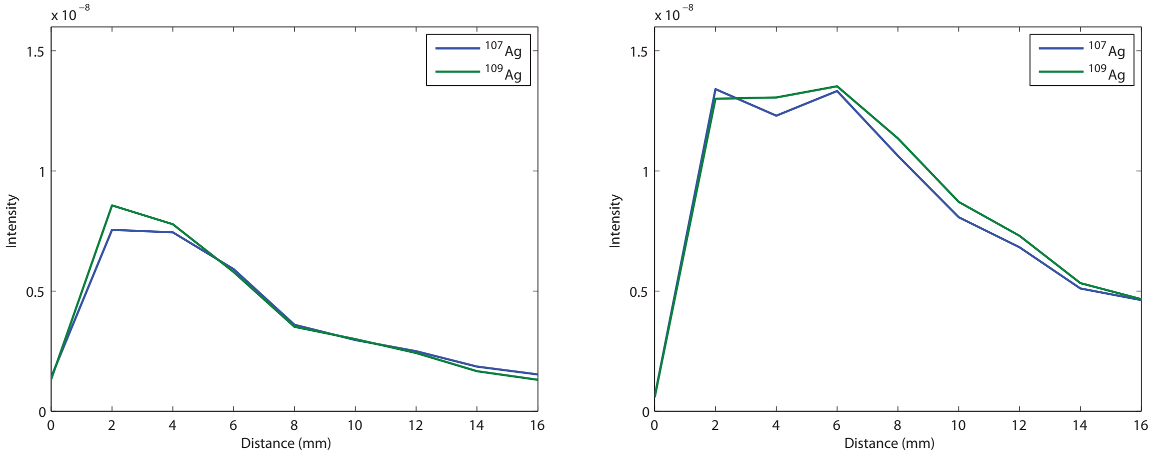

(a) Isotope content with distance at 9 μs.

(b) Isotope content at 13 μs.

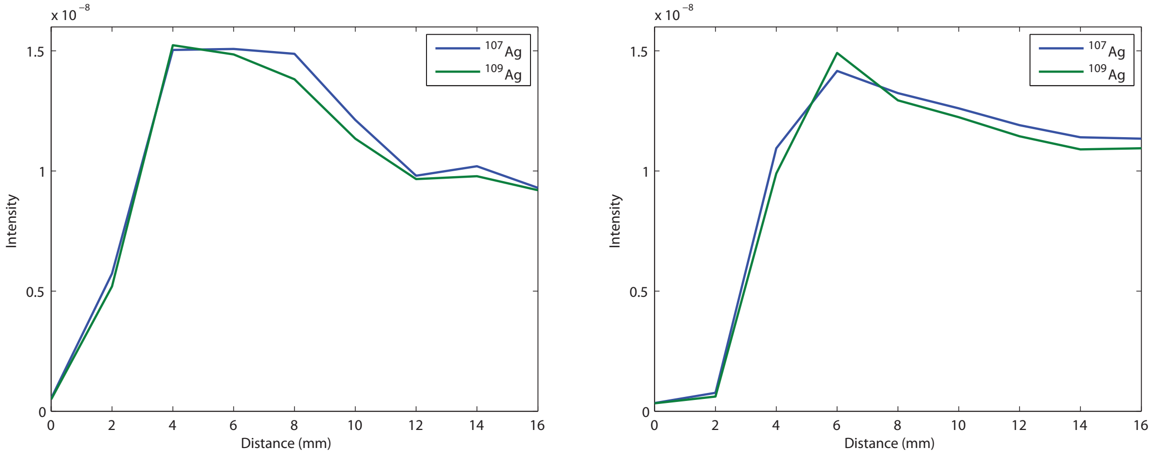

(c) At 17 μs.

(d) At 21 μs.

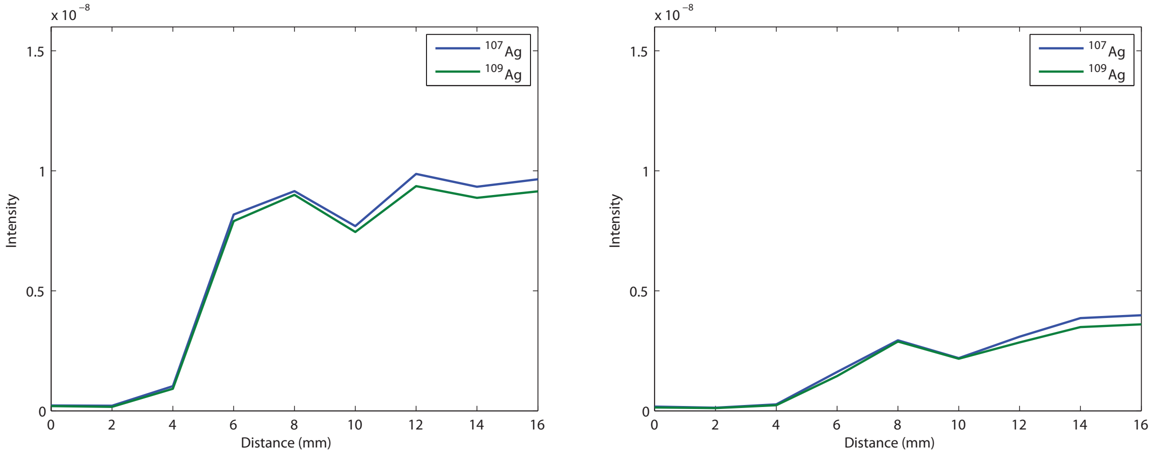

(e) At 26 μs.

(f) At 34 μs.

Fig. 4.6 The isotope content near the center of the plume was plotted against distance. The ion peak tends to rise and fall in intensity over time, showing little forward motion compared with the fast ions in Fig. 4.3. Throughout this group of ions, the isotope distribution remains fairly even.

from the side of the plume should yield data complementary to sampling from the center. Contrary to expectations, however, the results obtained using parameters for sampling the plume side are strikingly similar to the results from the plume center in Sec. 4.1.2. The temporal profiles in Fig. 4.7 also show two slow ion distributions that merge at 6 mm in Fig. 4.7(d), the large ion group in Figs. 4.7(e) and 4.7(f) also have slight shoulders toward later times, and the ^{107}Ag fraction also dips slightly toward the rising edge of the ion peak. In spite of applying completely different voltages to the repellers and the reflectron, there are few differences in the temporal profiles of Fig. 4.7 or the spatial profiles of Fig. 4.8 for the side of the plume when compared with those for the plume center in Figs. 4.5 and 4.6.

4.1.4 Early Ions

Especially when compared to the entire plume in Sec. 4.1.1, the isotope ratio for the plume center and the plume side in Sec. 4.1.2 and 4.1.3 exhibit very little change. The sharp swing in the isotope ratio when measuring the entire plume, however, mostly takes place in the first few microseconds, which are less accessible when examining the center and side of the plume due to interference from early ions. Thus, it could be argued that the same isotope separation may still exist in the center and side of the plume but simply could not be detected through the noise of the early ions.

Fig. 4.9 shows that this is not the case. Although the noise from the early ions has a larger magnitude when scanning the plume center and plume side in Fig. 4.9(b), the ion peaks for ^{107}Ag and ^{109}Ag remain at a much lower absolute intensity than those for the entire plume in Fig. 4.9(a). Even accounting for the fact that a smaller region of the plume is being collected, the amplitude of these peaks is still much lower than expected. Although the early ions generate greater interference for the plume center and plume side, examining the oscilloscope traces suggests an absence of ejected ions at early times, which is part of the reason the ion peaks are more difficult to distinguish from the early ions. Thus, the lack of a difference in the isotope ratio is due to the physical absence of fast ions and not the inability to quantify them.

4.1.5 Ion Energy

One explanation for the absence of fast ions in the center and side of the plume is that the system was not configured to observe them. As described in Sec. 3.2.3, the reflectron can not select for potential energy alone, so velocity is restricted as well as position when using the voltages to sample a specific lateral cross-section of the plume. As a result, the configuration for the plume center does not exactly select for ions in the center of the plume but those with a specific velocity and position combination. Similarly, the configuration for the plume side includes only ions under a specific kinetic energy threshold. The exact parameter space of the accessible ions is shown in Fig. 4.10.

If the kinetic energy of the ions is small relative to their potential energy between the repellers, Fig. 4.10 shows that the voltages used for the entire plume would collect the vast majority of the ions in the plume, the plume center configuration would collect most of the

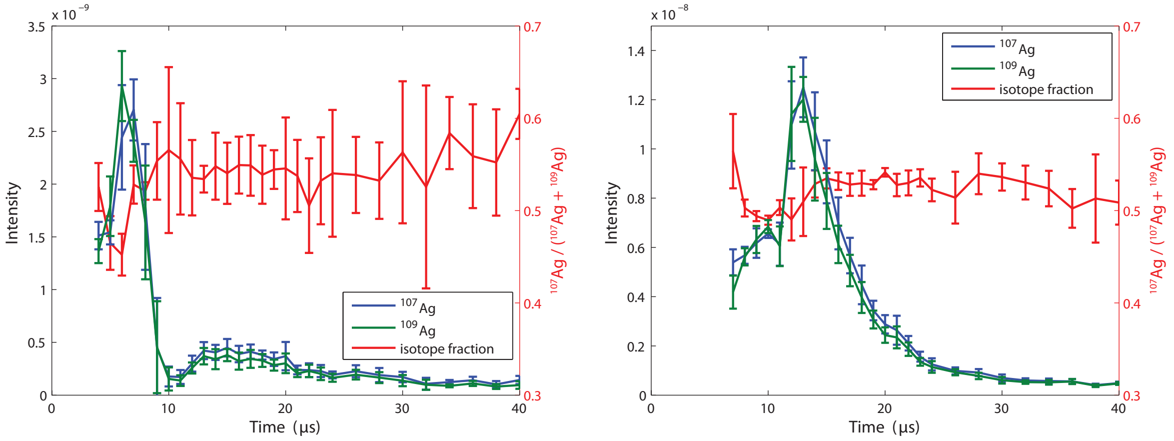

(a) Isotope content with time at 0 mm. **(b)** Isotope content at 2 mm.

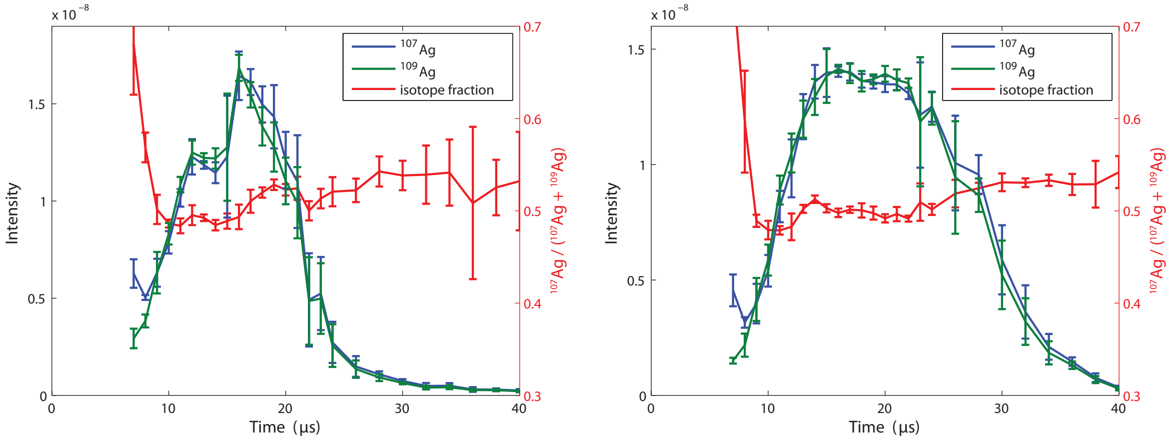

(c) At 4 mm. **(d)** At 6 mm.

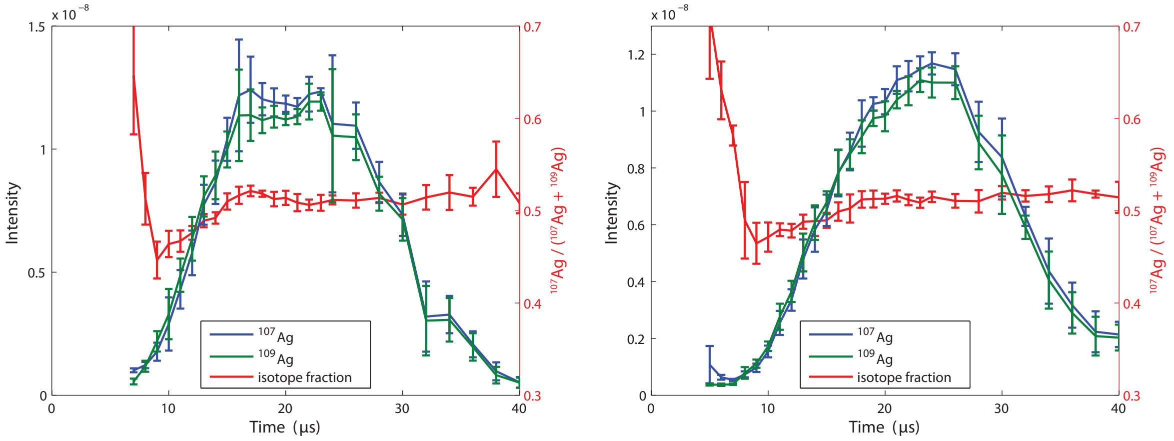

(e) At 10 mm. **(f)** At 16 mm.

Fig. 4.7 The isotope content was measured near the side of the plume at different distances from the target surface. The results are very similar to the data obtained from the plume center, with mostly slower ions observed under this configuration and the ^{107}Ag fraction decreasing slightly toward the rising edge of the ion peak.

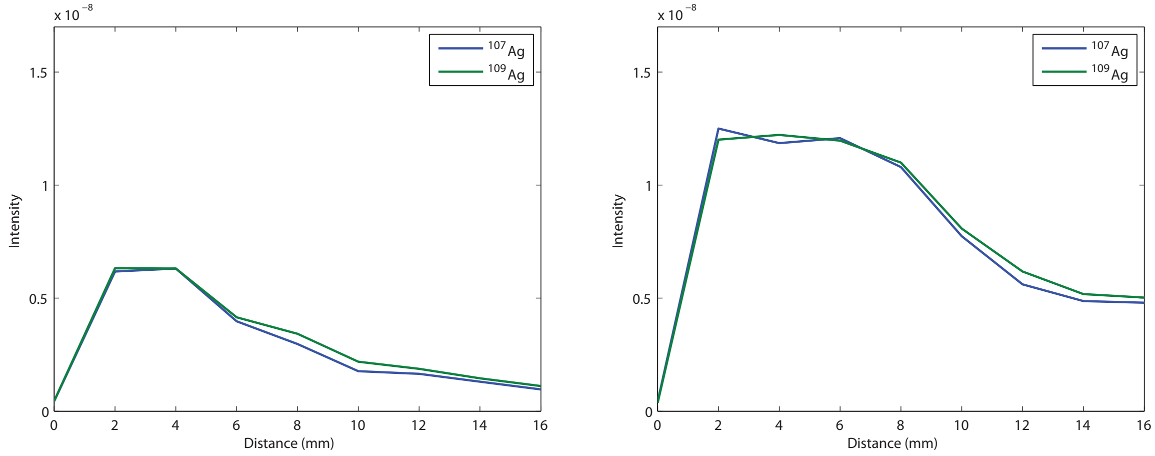

(a) Isotope content with distance at 9 μs.

(b) Isotope content at 13 μs.

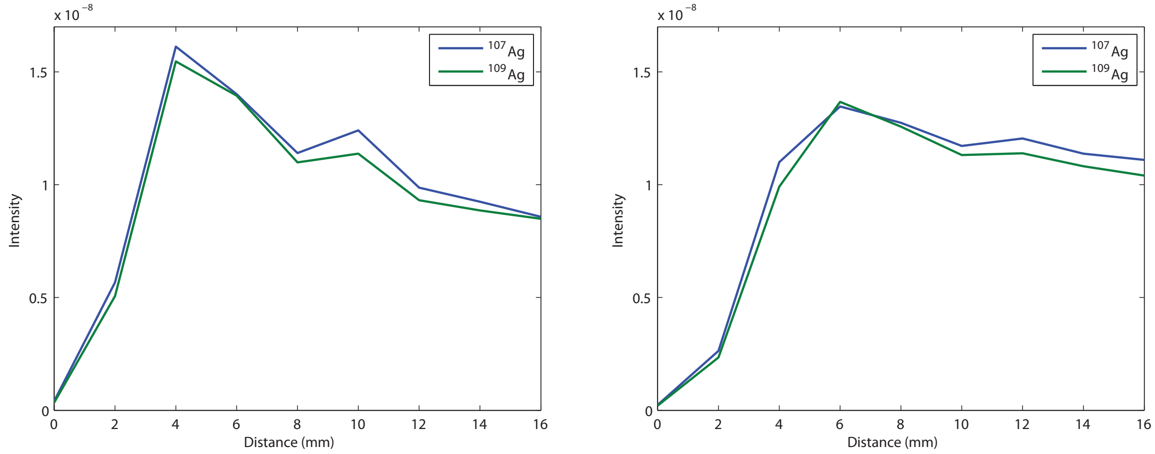

(c) At 17 μs.

(d) At 21 μs.

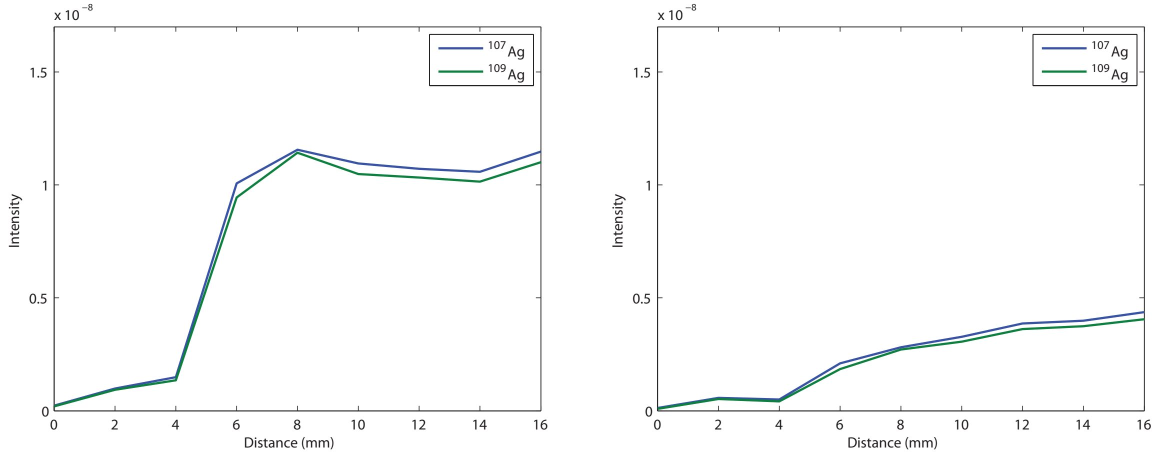

(e) At 26 μs.

(f) At 34 μs.

Fig. 4.8 The isotope content near the side of the plume was plotted against distance. Despite the different reflectron parameters, the spatial profile is very similar to that for the center of the plume in Fig. 4.6. The peak shows little forward motion and the isotope ratio is close to even.

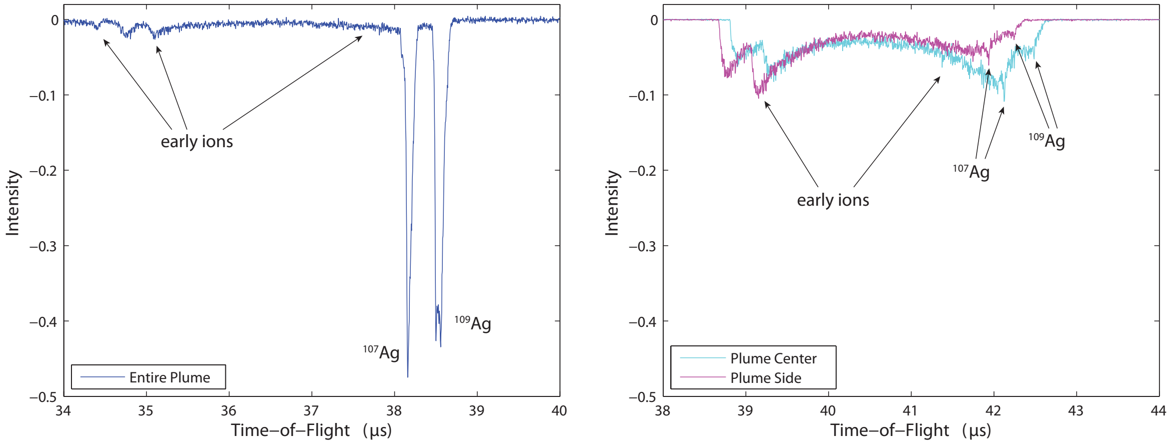

(a) Voltage trace for the entire plume at 4 μs and 4 mm.

(b) Voltage trace for the plume center and the plume side at 4 μs and 4 mm.

Fig. 4.9 Not only are the early ions more prominent in (b), but the pulsed ions, whose peak areas are used for the isotope content, have much lower intensities. The difficulty quantifying the isotope ratio at early times for the plume center and plume side is largely due to the lack of fast ions, so there is a true qualitative difference between the entire plume and the plume side and center, which can not be explained by the presence of early ions.

ions in the center region, and the plume side configuration would collect those to the side near the entrance of the mass spectrometer. The fact that the spatial and temporal profile of the plume center and plume side are very similar to the slow ions from the entire plume suggests that this is indeed the case for ions with low kinetic energies. That the faster ions could not be detected is readily apparent for the plume side configuration based on its lower kinetic energy and velocity thresholds in Fig. 4.10. Furthermore, this is consistent with Fig. 4.9(b), in which the intensity of the ^{107}Ag and ^{109}Ag ions are lowest for the plume side. Fig. 4.10, however, shows that higher velocities, at least in some parts of the plume, can be detected using the plume center configuration. If the fast ions are not observed using these parameters, they must arise from a combination of position and velocity accessible to the entire plume configuration but not to the plume center. In the graph, the fast ions must reside in the yellow regions that do not overlap with the cyan or magenta.

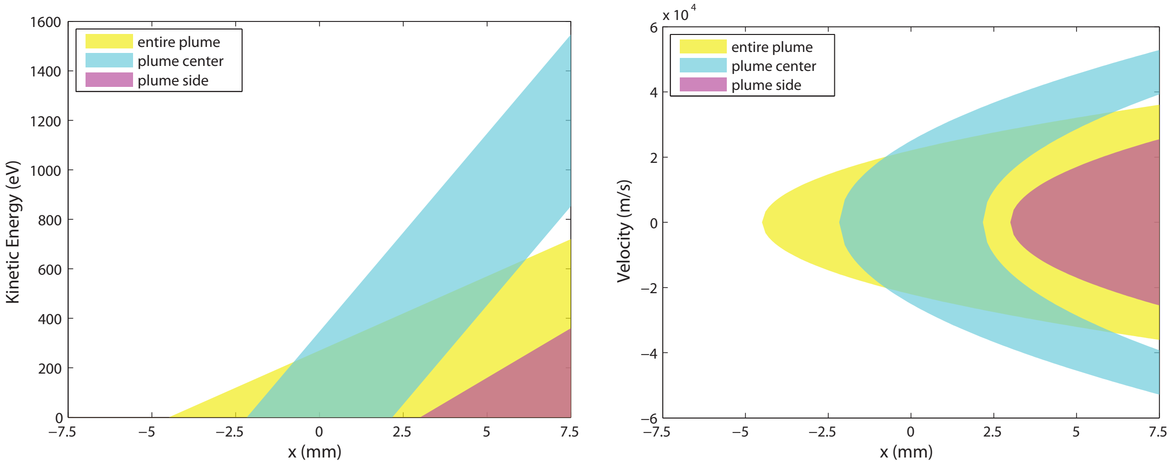

(a) Accessible ion kinetic energies and positions under the three configurations.

(b) Accessible combinations of ion velocity and position under the three configurations.

Fig. 4.10 Because kinetic energy is convoluted with potential energy in the reflectron (a), the ions sampled represent a parameter space that includes only velocity and position combinations in (b). Although the plume center configuration does allow for some ions with high kinetic energy, it does not cover the same velocity region as the entire plume configuration. The plume side configuration, on the other hand, is completely unable to access high velocity ions because of its low energy cutoff.

4.2 Lateral Profile

Neither sampling the center of the plume nor sampling the side of the plume produced the changes in the isotope ratio observed when measuring the entire plume. This suggests that the ions examined under those conditions were not the ones responsible for isotope separation. In order to isolate the ions that do show different isotope distributions, a variety of configurations for the repellers and reflectron were tested. First, the repeller voltages were adjusted to widen the center part of the plume being sampled in Sec. 4.2.1. Next, the lateral slice being measured was slowly increased from a small sliver near the entry to the mass spectrometer until it encompassed most of the plume in Sec. 4.2.2. Finally, a lateral slice with a fixed window was scanned across the width of the plume in Sec. 4.2.3. As before, these nominal descriptions assume that the ions have relatively low kinetic energy, but the actual regions from which the ions are sampled include both position and velocity and are somewhat more complicated. For all of the measurements in this section, the temporal profile was obtained at a single distance from the target surface to allow for rapid analysis using a larger number of voltage configurations.

4.2.1 Sampling the Plume Center

Since the voltages used for the plume center in Sec. 4.1.2 did not capture the ions which showed isotope separation, ions were sampled from successively wider regions of the plume starting from the center and spreading out toward the sides, as shown in Table 3. With the optimal reflectron voltages fixed, the lateral slice was broadened by reducing the repeller voltages so that the reflectron voltages would encompass larger and larger shares of the space between the two repellers.

Repellers (V)		Reflectron (V)		Deflector (V)	Range (mm)	
Pos	Neg	R2	R1	XY2	Far	Near
1100	-1100	336	-336	-1201	-2.29	2.29
900	-900	336	-336	-1201	-2.8	2.8
700	-700	336	-336	-1201	-3.6	3.6
500	-500	336	-336	-1201	-5.04	5.04

Table 3 Instrument parameters and sampling range for the plume center

In Fig. 4.11, lower repeller voltages correspond to wider swathes from the center of the plume. Fig. 4.11(a) is very similar to Fig. 4.5(e) taken at the same distance in the experiment on the plume center, except that the rising edge of the ion peak comes to a sharp point, suggesting that there may be two distinct groups of ions in the area under the curve. The part of the peak at earlier times does indeed increase dramatically as larger regions are sampled in Figs. 4.11(b) and 4.11(c) until these faster ions come to dominate the group in Fig. 4.11(d). While the transition for ^{107}Ag toward earlier times is fairly steady, Fig. 4.11(d) introduces an extra ^{109}Ag peak centered near 20 μs.

For the first three graphs in Fig. 4.11, the isotope ratio remains fairly stable. If the large curve is thought of as being divided into a fast peak and a slow peak, there is slightly more ^{107}Ag near the fast peak and slightly more ^{109}Ag near the slow peak, which becomes hidden in the shoulder of the fast ions. This is consistent not only with the ions from the plume center and the plume side in Sec. 4.1.2 and 4.1.3 but also with the slow ions from the entire plume. In Fig. 4.11(c), however, there is slightly more ^{109}Ag both before and after the peak ion intensity, which is somewhat unusual since the natural abundance ratio includes slightly more ^{107}Ag. An enormous shift in the isotope ratio, however, takes place in Fig. 4.11(d). Not only does the fast ^{109}Ag peak lead the corresponding ^{107}Ag, but there is also a large increase in the number of slower ^{109}Ag ions at later times. This increase in ^{109}Ag around 20 μs is not matched by a peak in ^{107}Ag and causes the ^{107}Ag fraction drop sharply before stabilizing back near the natural abundance. Capturing a broad swath of the ions across the center of the plume both recovers the original isotope skew in the fast ions and produces a new decrease in the ^{107}Ag fraction at later times due to an unexpected distribution of ^{109}Ag.

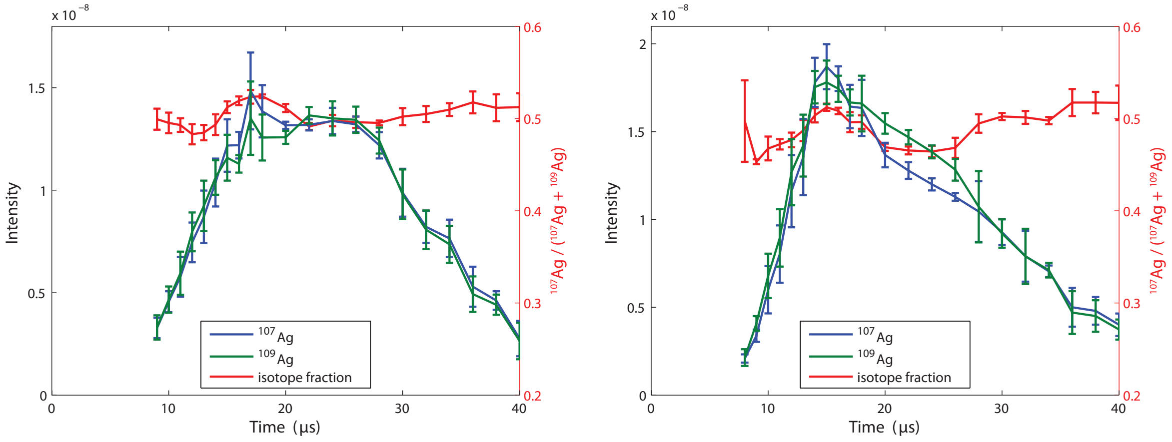

(a) Isotope content over time at 10 mm with the repellers at 1100 and -1100 V.

(b) Isotope content with the repellers at 900 and -900 V.

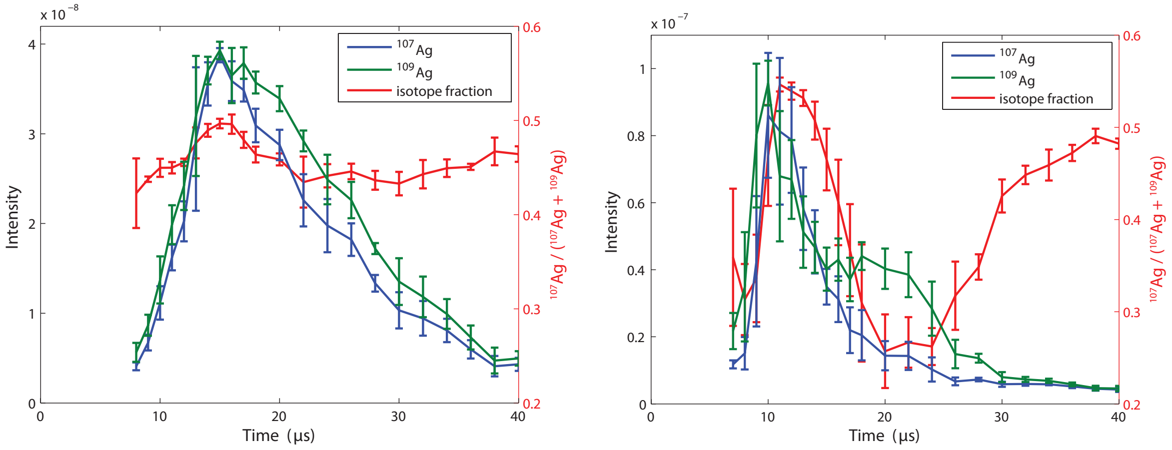

(c) Repellers at 700 and -700 V.

(d) Repellers at 500 and -500 V.

Fig. 4.11 The repeller voltages were decreased to sample successively broader swathes of the plume center. The concentration of faster ions increases with the width of the sampling window, but not until the repellers are lowered to 500 and -500 in (d) is there a major change in the isotope ratio. The graph in (d) includes both the shift in the fast ^{109}Ag peak toward earlier times, which was observed in the entire plume, and an additional ^{109}Ag peak at later times, which was highly unanticipated.

The parameter space of position and velocity when sampling the three largest widths are shown in Fig. 4.12. Setting the repellers to lower voltages not only includes a broader region but also favors lower velocities. Using the widest configuration of 500 and -500 V extends the sampling to two regions not covered by higher voltages. Both are low-velocity zones, one close to the mass spectrometer and the other on the far side of the plume. Since the region near the mass spectrometer would also have been sampled while examining the plume side, the ions responsible for the additional ^{109}Ag are most likely from the far side of the plume. The decreasing kinetic energy requirement of the near side, however, may be contributing to the increasing fast peak by incorporating additional ions of moderate velocity.

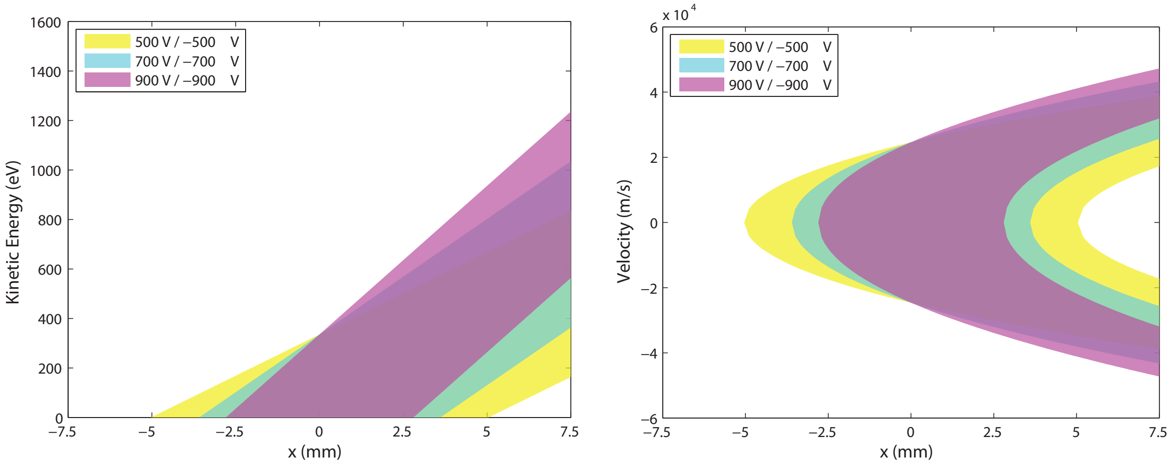

(a) Accessible combinations of ion kinetic energy and position as the sampled width is increased from the center.

(b) Accessible combinations of ion velocity and position as the sampled width is increased from the center.

Fig. 4.12 As the repeller voltages are reduced, a broader region is sampled and more ions can be collected at low velocities to either side of the plume. Since the ions on the right near the entrance to the mass spectrometer would already have been sampled by the plume side measurement, those on the far side of the plume are more likely to play a role in the isotope separation.

4.2.2 Cumulative Sampling from the Plume Side

A similar effort was made to widen the sampling window from one edge of the plume to the other over multiple trials. With the repellers set to 1200 and 0 V, the upper reflectron voltage was slowly increased, as shown in Table 4, until it covered just over two-thirds the width of the plume.

The temporal profile at 10 mm from the target was graphed in Fig. 4.13 for six representative reflectron voltages. As before, there appear to be at least two ion distributions

Repellers (V)		Reflectron (V)		Deflector (V)	Range (mm)	
Pos	Neg	R2	R1	XY2	Far	Near
1200	0	80	-478	-1210	6.5	7.5
1200	0	160	-416	-1210	5.5	7.5
1200	0	240	-362	-1210	4.5	7.5
1200	0	320	-311	-1210	3.5	7.5
1200	0	400	-263	-1210	2.5	7.5
1200	0	480	-217	-1210	1.5	7.5
1200	0	560	-173	-1210	0.5	7.5
1200	0	640	-133	-1210	-0.5	7.5
1200	0	720	-95	-1210	-1.5	7.5
1200	0	800	-62	-1210	-2.5	7.5
1200	0	880	-33	-1210	-3.5	7.5

Table 4 Instrument parameters and sampling range for cumulative sampling from the plume side

covered under the plotted curves. At the very low reflectron voltages in Fig. 4.13(a), which represent a small sliver of ions near the entrance to the mass spectrometer, the ion peak is slightly skewed in favor of faster ions. As the voltage is increased and the sampling window spreads out toward the plume center, slower ions begin to dominate and increase the ion concentration at later times. Only after the sampling width covers more than half the plume in Fig. 4.13(d) is there a significant increase in faster ions, which pulls the curve up to an early peak in Figs. 4.13(e) and 4.13(f).

The only change in the isotope ratio is the sharp drop in ^{107}Ag at early times, due to the faster ^{109}Ag in the fast ion peak. The slight shift in the fast peak between the two isotopes first becomes apparent at a reflectron voltage of 480 V in Fig. 4.13(c). At this point, just under half the plume is being measured, and the dip in the ^{107}Ag fraction becomes slightly more pronounced as the sampling window is increased to cover more of the plume. This is generally consistent with the results from Sec. 4.1, which show that changes in the isotope ratio are observed for the entire plume but not the plume side. If a large enough region from the side of the plume is used, as in Fig. 4.13(c), the drop in the ^{107}Ag fraction begins to appear whereas no shift in the isotope ratio is observed when the sampling window is set to the center of the plume.

One advantage of taking successively larger regions from the plume side is that the ion intensities can be subtracted to give the isotope content in each incremental slice. Although there is a large degree of uncertainty from taking the difference of two noisy curves, the graphs in Fig. 4.14 show distinctly which isotopes are being added to the temporal profile as the size of the sampling window is increased. Consistent with Fig. 4.13, expanding the

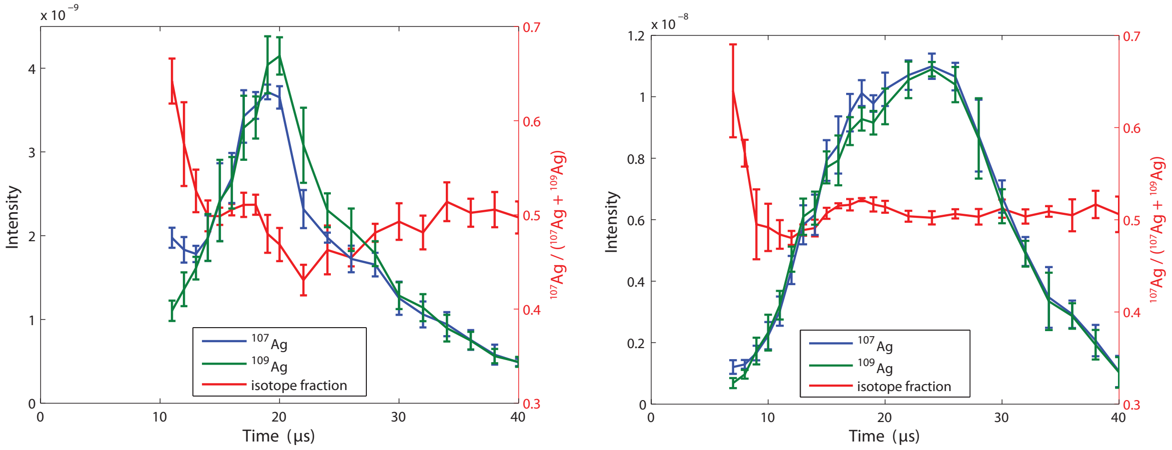

(a) Isotope content over time at 10 mm with the reflectron at 160 V.

(b) Isotope content over time with the reflectron at 320 V.

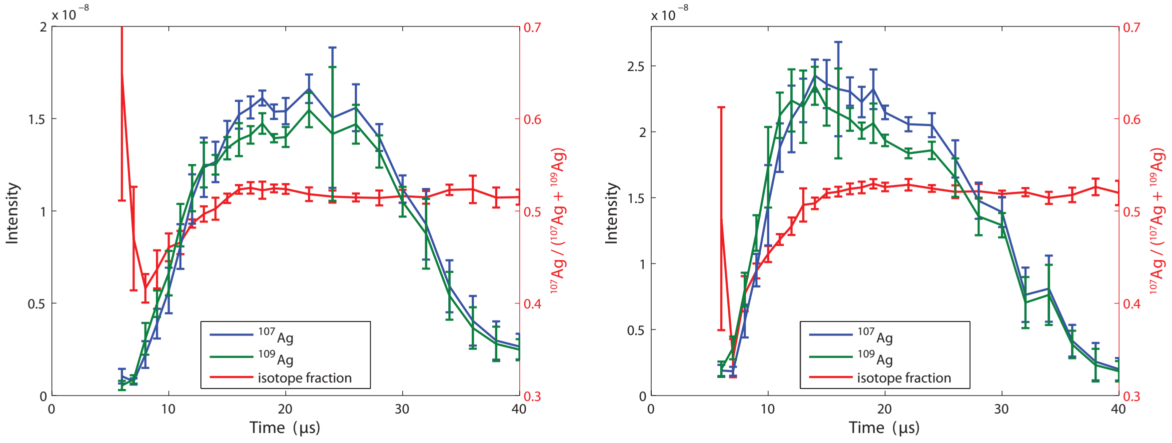

(c) Reflectron at 480 V.

(d) Reflectron at 640 V.

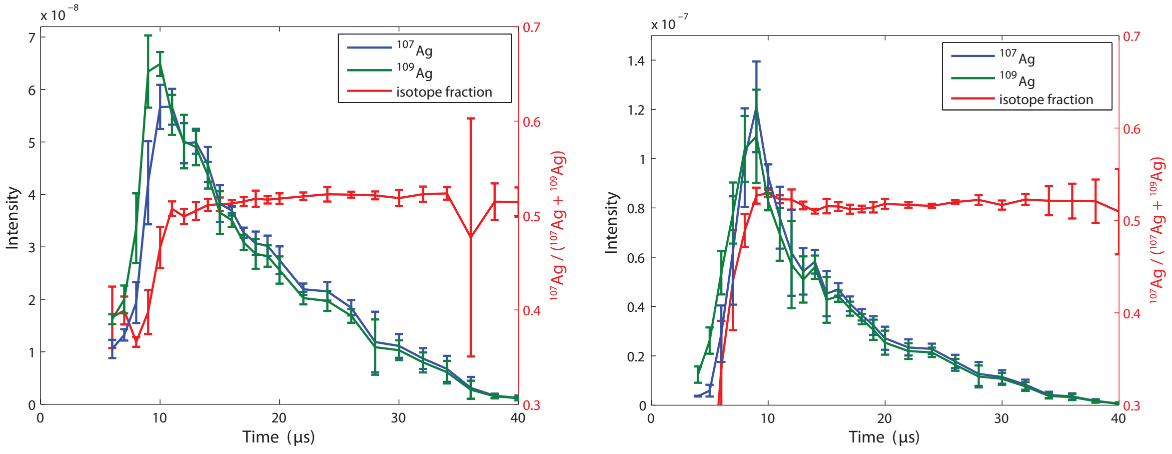

(e) Reflectron at 800 V.

(f) Reflectron at 880 V.

Fig. 4.13 In this series, the sampling window is expanded from one side of the plume to the other. As this sampling width is increased, a larger number of ions are detected at early times and these ions provide the shift in the fast isotope peaks that causes the ^{107}Ag fraction to drop early on.

sampling width initially increases the number of slower ions, as shown in Fig. 4.14(b). As the window increases toward the center of the plume, the ion distribution shifts toward earlier times and higher velocities, and further broadening the sampling on the far side of the plume Fig. 4.14(d) yields mostly fast ions.

The error bars for the ^{107}Ag fraction have not been shown in Fig. 4.14, because they become unreasonably large when the uncertainties are propagated from the ion intensities. Although the decrease in the ^{107}Ag composition at early times is remarkably consistent across all sections of the plume, this may partly arise as an artifact of the early ions. This is especially likely with lower reflectron voltages, where ion intensities are lower and interferences play a larger role. Since the early ions will artificially increase the ^{107}Ag intensity preferentially for measurements made near the mass spectrometer, subtracting these ions may result in proportionally more ^{109}Ag. When more ions are included at higher reflectron voltages, the early ions are less significant and the drop in the ^{107}Ag fraction at early times in Figs. 4.14(c) and 4.14(d) is more likely to reflect actual phenomena.

The parameter space accessible to the mass spectrometer in Fig. 4.15 shows that the energy limit set by the reflectron both increases the accessible kinetic energy and extends the spatial range over which ions can be detected. Based on the results, the increase in kinetic energy may play the more important role, considering that raising the reflectron voltage tends to allow a larger number of fast ions into the mass spectrometer and these fast ions appear to be responsible for the drop in the ^{107}Ag fraction at early times. It is important, though, to recognize that the kinetic energy described in Fig. 4.15 is perpendicular to the plume along the direction of the mass spectrometer while the fast ions that have entered the mass spectrometer at early times have high velocities along the direction of the plume. It is certainly possible, of course, for the ions to have high velocities in both directions.

4.2.3 Lateral Sections of the Plume

Instead of subtracting one spatial profile from another, the repellers and reflectron can also be configured to sample these lateral slices directly. If the reflectron voltages are kept constant, adjusting the the repellers in parallel yields lateral sections of the plume, as shown in Table 5. Since the reflectron must still compensate for the energy difference in the ions, the parameters are constrained such that only relatively large slices 7 mm in width can be obtained. Scanning this 7 mm window across the plume nonetheless yielded some unexpected results.

Several of the trends in Fig. 4.16 are similar to those observed when taking cumulative regions in Sec. 4.2.2. There appear to be at least two ion distributions under the curve, and fast ions are favored as the sampling window moves away from the mass spectrometer. Toward the far side of the plume, the absolute intensity of both ions increases as does the proportion of ^{109}Ag. The appearance of an additional slow ion peak in Fig. 4.16(d) consisting exclusively of ^{109}Ag, however, is unusual. Although these results are similar those obtained when increasing the sampling width at the plume center in Sec. 4.2.2, the effect is even more dramatic when the parameters are tuned to focus on the far side of the

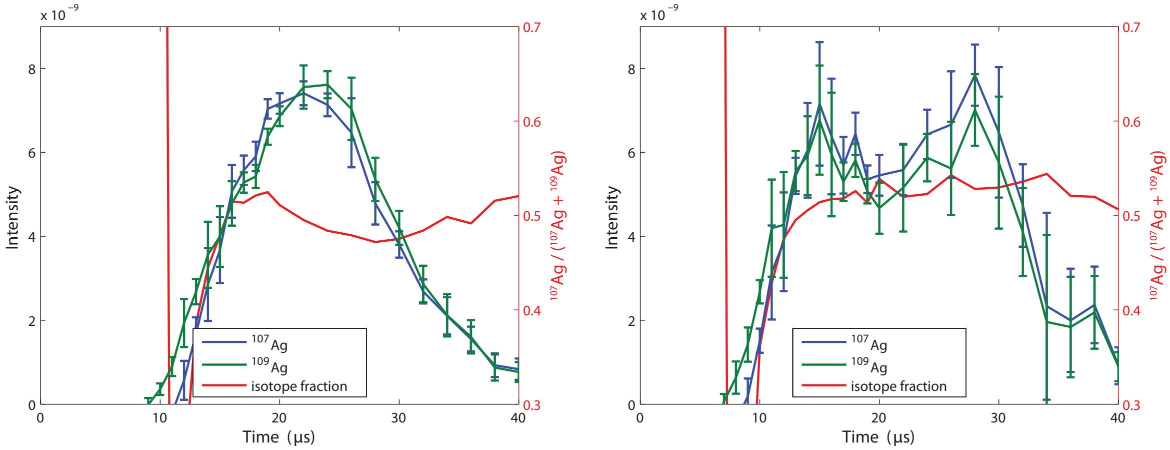

(a) Difference in the isotope content between the reflectron at 240 V and the reflectron at 80 V.

(b) Between the reflectron at 400 V and the reflectron at 240 V.

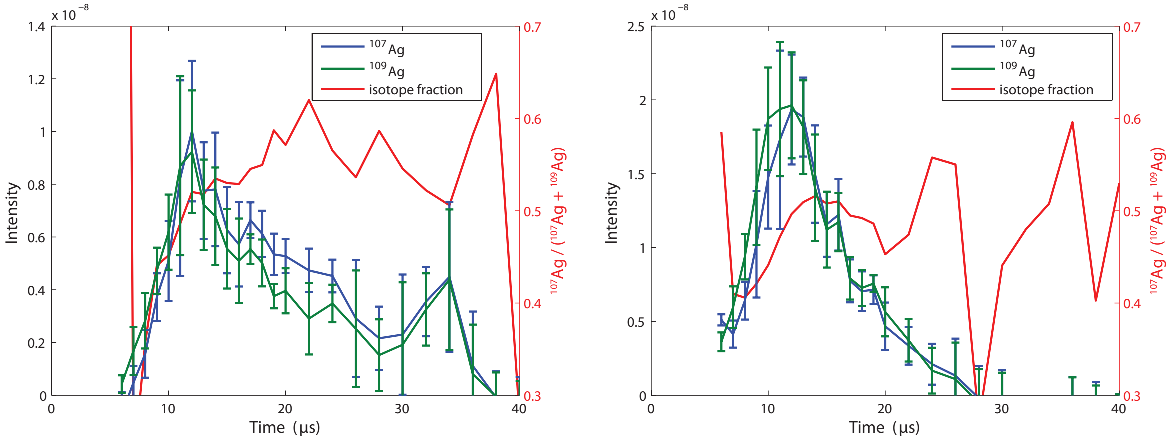

(c) Between the reflectron at 560 V and the reflectron at 400 V.

(d) Between the reflectron at 720 V and the reflectron at 560 V.

Fig. 4.14 Taking the difference in the isotope intensity between successively larger slices of the plume yields the isotope content in each incremental region. The changes in ion intensity are more apparent in this series of graphs. Broadening the window near the mass spectrometer captures a distribution of relatively slow ions (a), while increasing the sampling width near the center of the plume collects primarily fast ions that cause the initial dip in the ^{107}Ag fraction (d). The error bars for the fraction of ^{107}Ag have been omitted, because they are too large to be useful. The drop in the ^{107}Ag fraction at lower voltages may be an artifact of the early ions, but the change is more likely to be real at higher voltages with increased ion intensity.

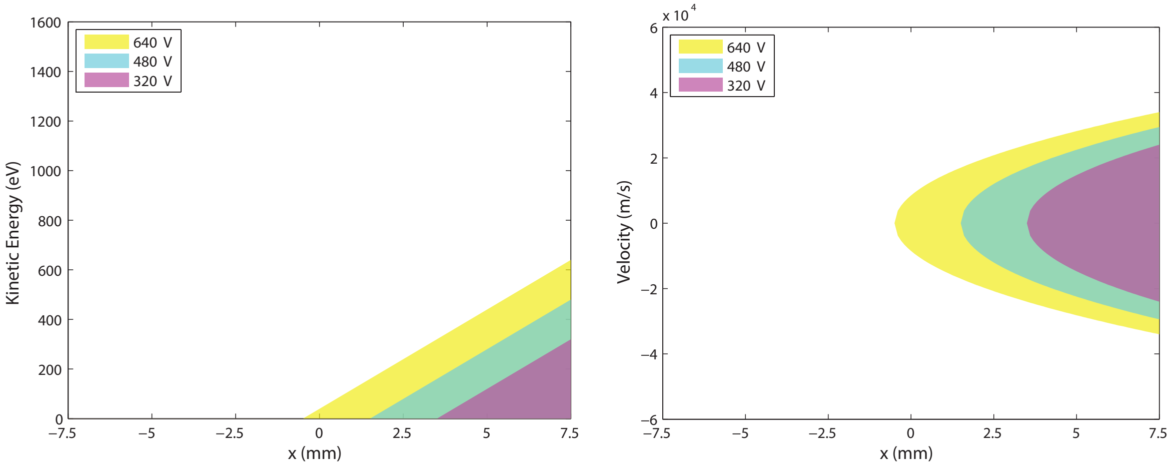

(a) Accessible combinations of ion kinetic energy and position as the sampled region is increased from the side.

(b) Accessible combinations of ion velocity and position as the sampled region is increased from the side.

Fig. 4.15 Increasing the reflectron voltage to broaden the sampling width provides a clear instance in which the kinetic energy and potential energy can not be distinguished. Expanding the sampling window across the plume also allows higher velocity ions to be detected, which may account for the increasing number of fast ions at higher voltages.

Repellers (V)		Reflectron (V)		Deflector (V)	Range (mm)	
Pos	Neg	R2	R1	XY2	Far	Near
1083	-417	283	-417	-1225	0.5	7.5
988	-512	288	-412	-1224	-0.5	6.5
889	-611	289	-411	-1224	-1.5	5.5
789	-711	289	-411	-1224	-2.5	4.5
691	-809	291	-409	-1224	-3.5	3.5
592	-908	292	-408	-1224	-4.5	2.5
492	-1008	292	-408	-1224	-5.5	1.5
393	-1107	293	-407	-1224	-6.5	0.5
293	-1207	293	-407	-1224	-7.5	-0.5

Table 5 Instrument parameters and sampling range for lateral sections of the plume

plume. This valley in the ^{107}Ag fraction appears only subtly when measuring the entire plume and not at all when examining cumulative regions.

The isotope ratio also bears resemblance to sampling the center of the plume in Sec. 4.2.1. On the side close to the mass spectrometer in Figs. 4.16(a) and 4.16(b), there is very little change in the isotope ratio. Even at the center of the plume in Fig. 4.16(c), the dip in the ^{107}Ag fraction at early times is fairly modest, although the entire profile shows more ^{109}Ag at all points, as in Fig. 4.11(c). The shift in the fast ^{109}Ag peak is more pronounced in in Fig. 4.16(d), but the appearance of the secondary ^{109}Ag peak at later times is striking. Without a corresponding ^{107}Ag distribution, this produces a very large skew in the isotope ratio. Because the effect is the most dramatic in this instance, this configuration of sampling ions from the far side of the plume was used for a full spatial and temporal profile.

Constraints on the reflectron parameters required a relatively large sampling window, as shown in Fig. 4.17. Shifting the window rather than increasing the cumulative sampling region, however, allows for a constant sampling width. Based on the accessible parameter space in Fig. 4.17, the slow ^{109}Ag peak is more likely to have originated from farther ions with low kinetic energies rather than from near ions with very high kinetic energies. Configurations with the window closer to the mass spectrometer already have a fairly high kinetic energy limit, and similar results with regard to the additional ^{109}Ag were observed when using lower voltages near the center of the plume where high velocities remained inaccessible, as shown in Fig. 4.12. If these extra ^{109}Ag ions have relatively low kinetic energies, however, it is particularly suprising that they are only observed on the far slide of the plume but not on the near side closer to the mass spectrometer. Assuming a symmetric plume, corresponding ions on the near side should be accessible to the sampling windows close to the mass spectrometer. One difference between the two sides, however, is that the ions on the near side can enter the flight tube directly, while those on the far side must cross the plume to get to the mass spectrometer. The heavier ions may be preferentially making it through the plume and into the flight tube, although such a large discrepancy is still unexpected considering the small difference in the mass of the isotopes.

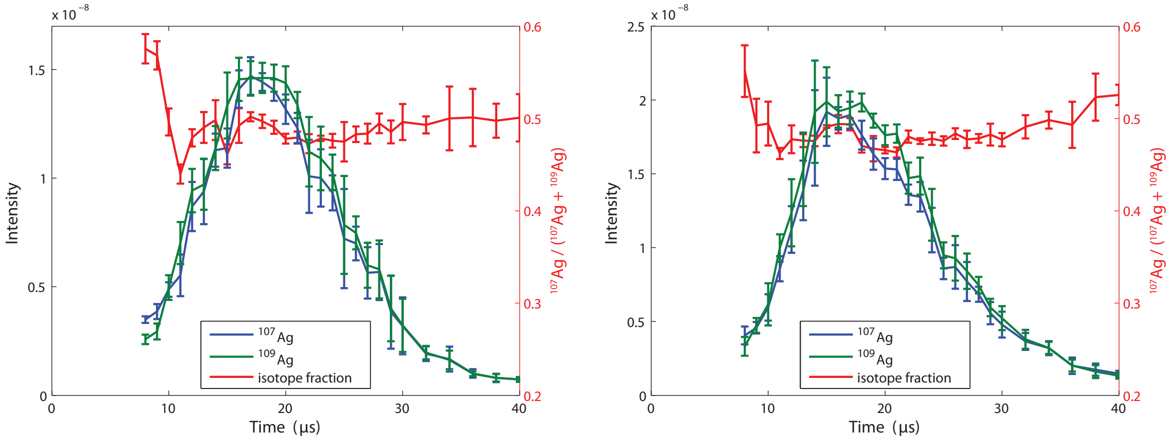

(a) The isotope content over time 10 mm from the target surface from 0.5 to 7.5 mm.

(b) The isotope content 10 mm from the target surface from -1.5 to 5.5 mm.

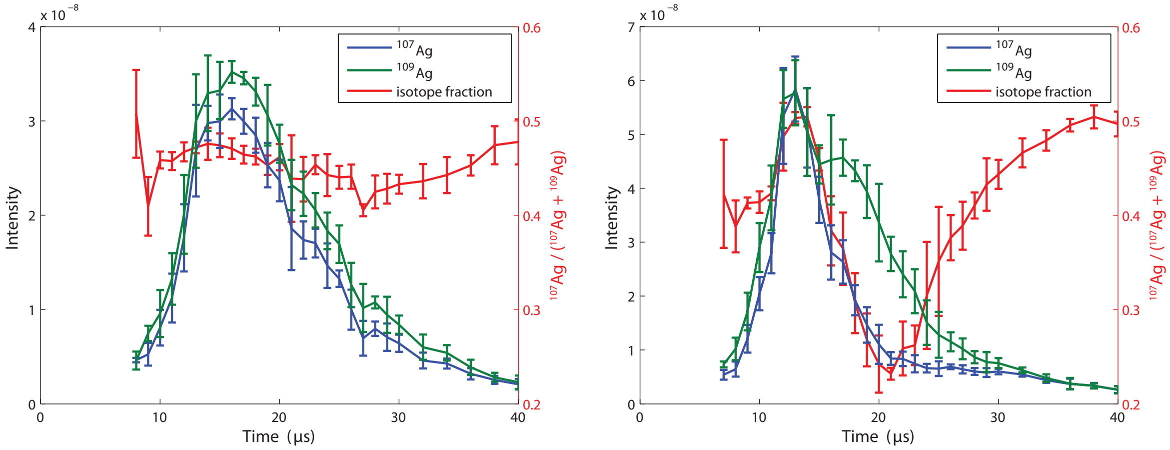

(c) From -3.5 to 3.5 mm.

(d) From -5.5 to 1.5 mm.

Fig. 4.16 Keeping the reflectron voltages constant while changing the repeller voltages in parallel allows a fixed window of 7 mm to be scanned across the plume. The plots here show similar effects to the cumulative measurements, with faster ions becoming more prominent as the window moves from the near side toward the center. On the far side of the plume, however, not only is there the initial dip in the ^{107}Ag fraction at early times but a secondary ^{109}Ag peak, unaccompanied by corresponding ^{107}Ag ions, appears at later times, causing a large imbalance between the two isotopes.

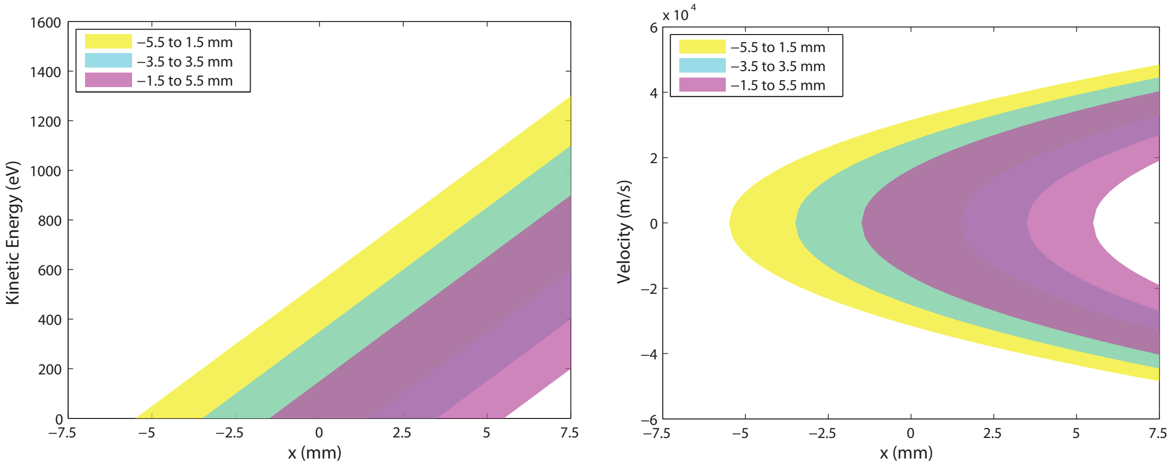

(a) Accessible combinations of ion kinetic energy and position as the sampled window is scanned across the width of the plume.

(b) Accessible combinations of ion velocity and position as the sampled window is scanned across the width of the plume.

Fig. 4.17 Since most of the configurations in this experiment can access relatively large kinetic energies, the changes in the isotope ratio is likely due to ions that originate from the far side of the plume. This is surprising, since the plume should be symmetric, but the sampling technique may favor ^{109}Ag on the side away from the entrance to the mass spectrometer.

4.3 Far Side of the Plume

The parameters that allowed for sampling from a lateral section on the far side of the plume were chosen for a more detailed study of isotope separation. As in Sec. 4.1, a full temporal and spatial profile was obtained using the configuration that produced the maximum change in the isotope ratio.

The plots in Fig. 4.18 are similar to those for the entire plume in that they feature two major ion distributions, a fast group at early times and a slow group at later times, that gradually merge into a single peak at about 8 mm from the target surface. While the behavior of the fast ions, with the ^{109}Ag peak leading the ^{107}Ag, has been observed under many different conditions, the evolution of the slow ions is novel. Within the slow peak, the two isotopes are fairly even at 2 mm in Fig. 4.18(b), with ^{109}Ag leading slightly in time. At 4 mm in 4.18(c), however, the ^{109}Ag concentration rises toward the leading edge of the slow ions while ^{107}Ag falls instead. This additional group of ions manifests as a broad shoulder at longer distances from the target surface, until the two isotopes become almost even again at 16 mm in 4.18(f).

The spatial distribution of the isotopes is plotted in Figs. 4.19 and 4.20. Fig. 4.19 shows ^{109}Ag moving ahead of ^{107}Ag in both space and time, which accounts for the low ^{107}Ag fraction at the leading edge of the plume. The development of the slow ^{109}Ag peak is captured in Fig. 4.20, and it appears as if the ^{109}Ag ions are lagging in space, remaining stationary while the ^{107}Ag continues to move ahead. This explanation is unlikely, however, since it suggests that the ^{107}Ag ions at large distances are not matched by a corresponding ^{109}Ag peak, which is clearly not the case based on the temporal profile at 16 mm in Fig. 4.18(f). Fig. 4.20 is nevertheless informative in showing the two ion distributions closely matched at 14 μs in Fig. 4.20(a) and the ^{109}Ag group sustaining its concentration while the ^{107}Ag dissipates.

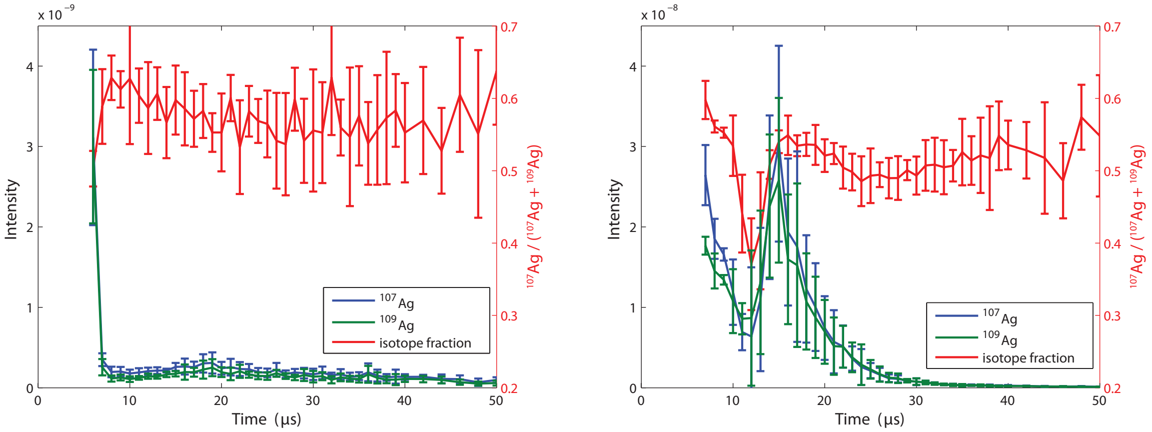

(a) Isotope content with time at 0 mm.

(b) Isotope content at 2 mm.

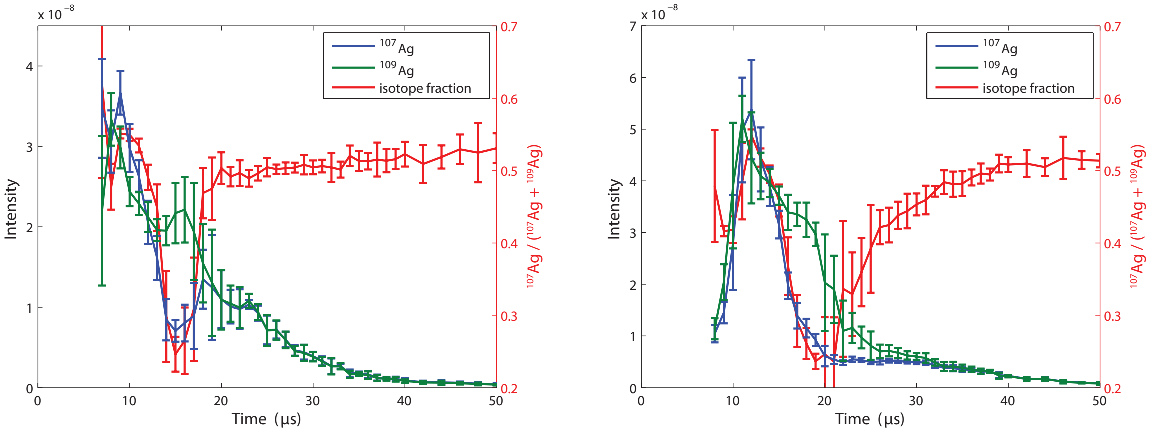

(c) At 4 mm.

(d) At 8 mm.

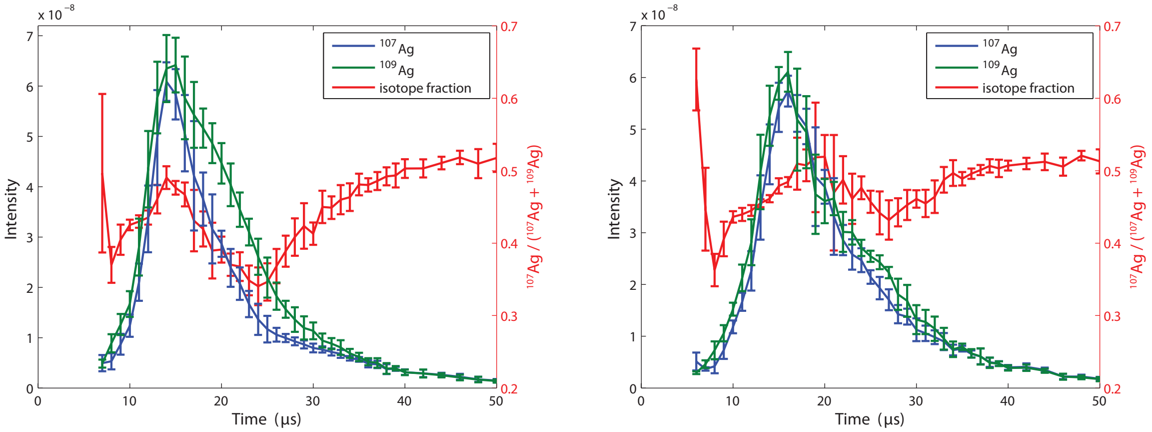

(e) At 12 mm.

(f) At 16 mm.

Fig. 4.18 The isotope content was measured for ions in a 7 mm window on the far side of the plume. The fast ions behave similarly to previous configurations, with the ^{109}Ag ions just ahead of the ^{107}Ag at early times. An additional ^{109}Ag peak, however, appears at the rising edge of the slow ions in (c), and it persists at larger distances, dramatically reducing the ^{107}Ag fraction. No corresponding peak of slow ^{107}Ag exists.

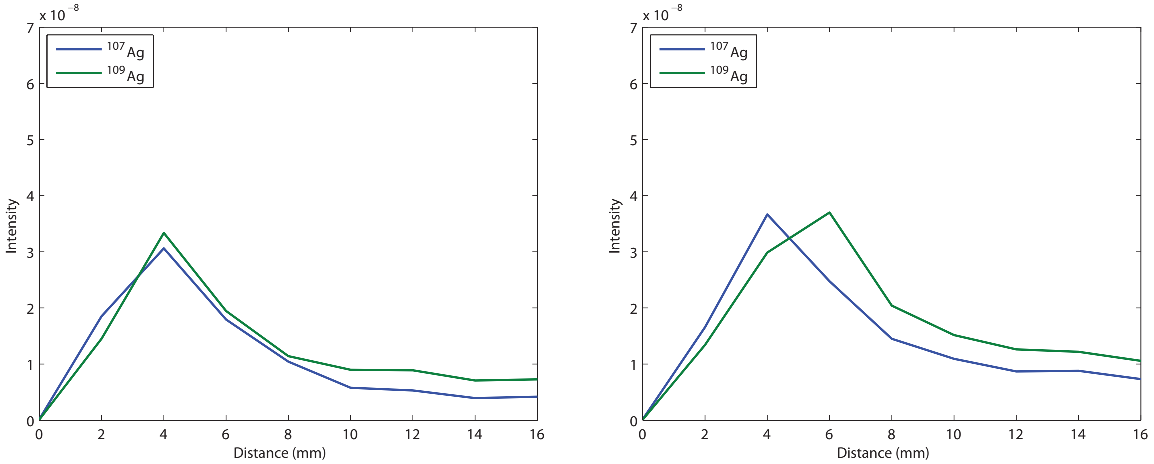

(a) Isotope content with distance at 8 µs. **(b)** Isotope content at 9 µs.

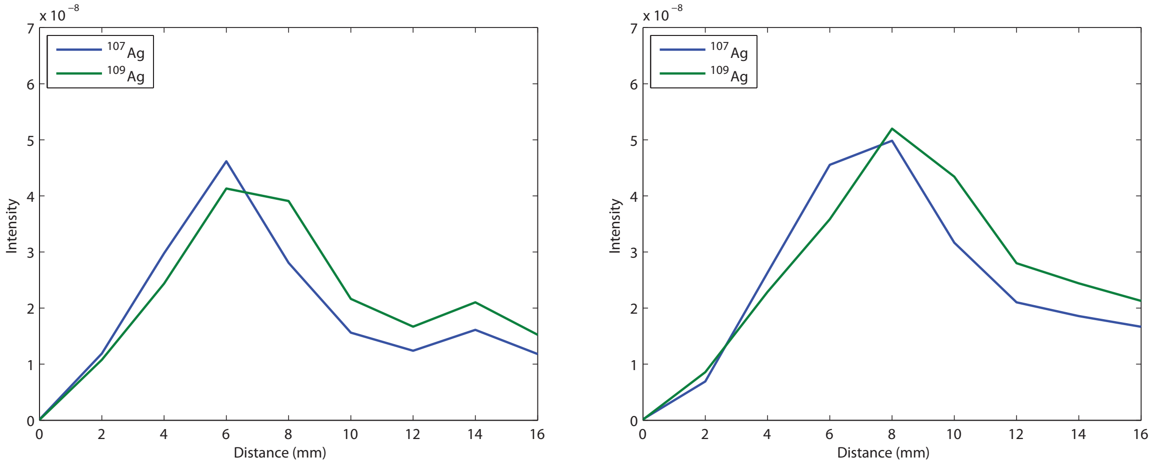

(c) At 10 µs. **(d)** At 11 µs.

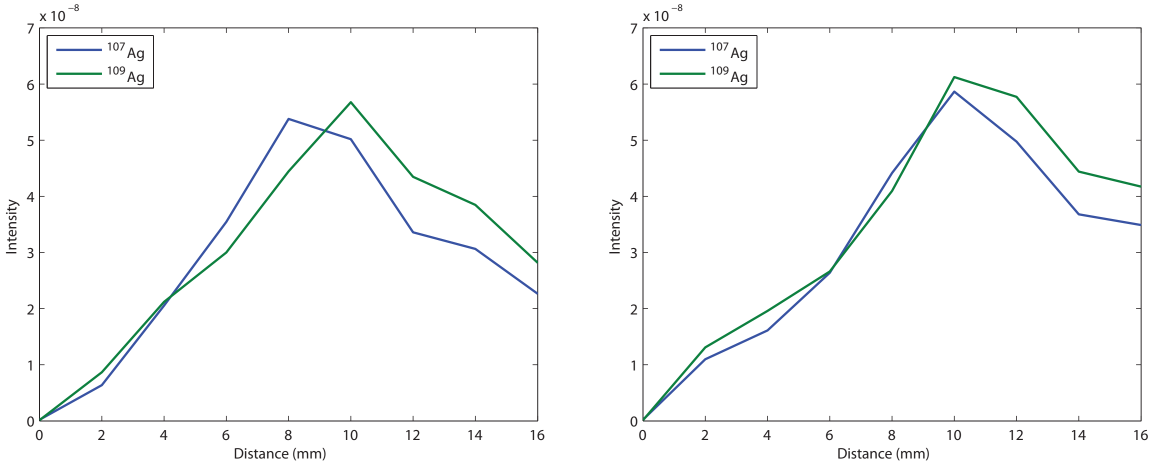

(e) At 12 µs. **(f)** At 13 µs.

Fig. 4.19 Among the fast ions, ^{109}Ag leads ^{107}Ag in both space and time. This phenomenon has been consistently observed any time the fast ions are present.

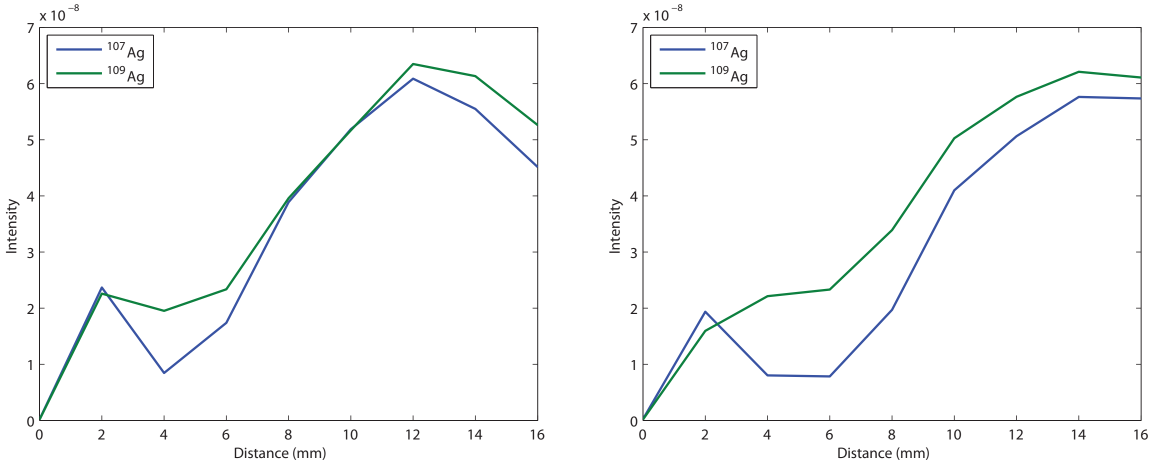

(a) Isotope content with distance at 14 µs. **(b)** Isotope content at 16 µs.

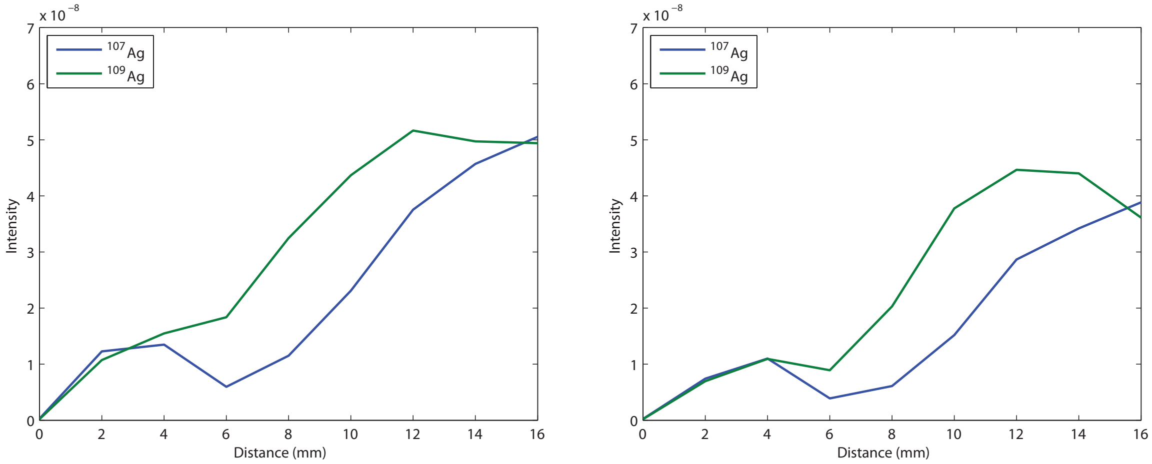

(c) At 18 µs. **(d)** At 20 µs.

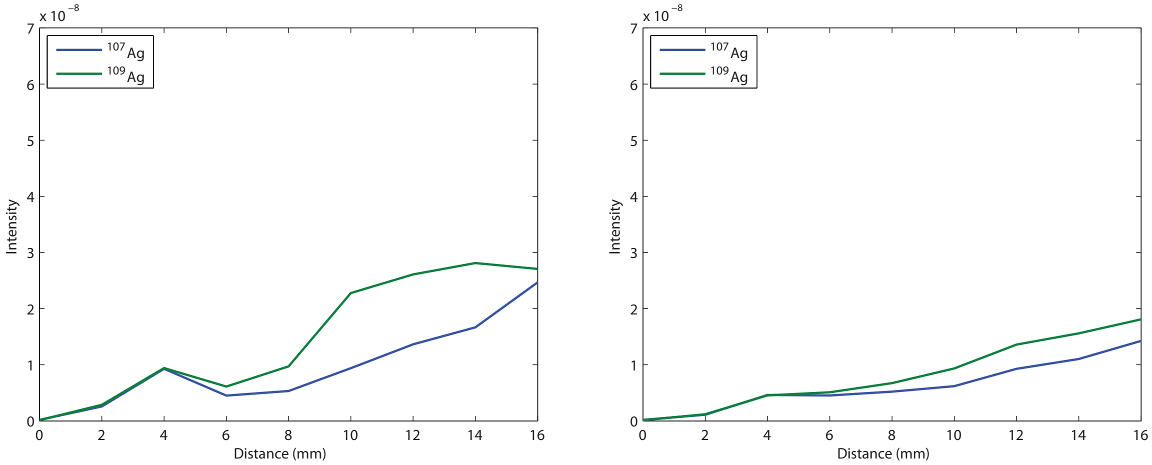

(e) At 24 µs. **(f)** At 28 µs.

Fig. 4.20 The appearance of an additional slow ^{109}Ag peak was unexpected. Based on these graphs, the ^{109}Ag ions appear to remain in place while the ^{107}Ag continue to move away from the target.

Chapter 5

Conclusions and Recommendations

The work described in this thesis can be broadly divided into two parts: developing and validating the time-of-flight mass spectrometer for isotope analysis in the laser plume and using this instrument to study the phenomenon of isotope separation within the plume itself. This chapter will begin with a brief review of the equipment modifications and analysis of instrumental parameters. The changes to the instrument and study of experimental variables were the basis for a thorough examination of the ablation plume, and the results yielded a map of the isotopes in the plasma as the plume developed with time. Conclusions regarding the nature of isotope separation during laser ablation will be drawn from these results, and future directions based on this research will be described in brief.

5.1 Orthogonal Acceleration Time-of-Flight Mass Spectrometry for Studying Laser Ablation

Due to the complexity of the time-of-flight mass spectrometer, careful study of the instrument parameters played a crucial role in the research. Because the phenomena were highly unexpected, extensive analysis was performed to ensure the validity of the experimental results as changes were made to the system. The most important alteration to the instrument involved modifying the repeller geometry, first removing the ring electrode from the ion trap system and then swapping the hyperbolic endcaps for flat plate electrodes. Although the original rationale for removing the ring electrode was to allow for the spatial profile to be observed, the changes in the electric field proved critical to the phenomenon of isotope separation. Specifically, the isotope ratio was reversed upon removing the ring and general characteristics of plume development changed as well. An analysis of the electric field between the flat plates and calculation of the ion trajectories using the SIMION finite difference package validated the principle that orthogonal slices of the plume were being sampled in the final configuration.

Changing the repeller design also allowed the target to be moved to difference distances from the entrance of the mass spectrometer. By measuring the ions at different target positions over a range of time delays, the spatial and temporal profile of the plume could be reconstructed in order to visualize the development of the plume during laser ablation. This process produced snapshots of the plume that revealed the position and relative movement of the two isotope distributions.

Finally, an analysis of the ion trajectory under various experimental conditions suggested that the voltage of the repellers and reflectron could be configured to collect different lateral slices of the plume, making it possible to vary the sampled widths along the direction of the mass spectrometer. This allowed ions from different parts of the plume to be selected in yet another spatial dimension. The primary role of the reflectron was not to act as an energy filter, however, but to compress the temporal spread of ions with different energies. As a result, the selectivity of the sampled regions was limited to broad swathes near the mass spectrometer, at the center of the plume, and on the far side of the plume. Furthermore, the kinetic energy of the ions was inextricably linked with the potential energy, so the position information could not be completely deconvoluted from the velocity information. By collecting data using different sets of parameters, however, general conclusions could be made about the position and velocity of the sampled ions.

5.2 Isotope Separation in the Ablation Plume

The complex nature of the instrument demands that several additional considerations be taken into account when interpreting the results. First the system is only capable of detecting a very small proportion of the ions produced each time the laser is fired. The ability to interrogate small parts of the plume and to observe differences in the isotope content across space and time forms the basis of this study. Conversely, most of the ions in a given shot are not collected and some ions may never be observed at all. The simulations and experimental data suggest that the early ions and very fast ions, in particular, can not be characterized with the mass spectrometer. The early ions, described in Sec. 2.2.2, enter the flight tube even before the voltage potential is applied to the repellers and, as a result, their times-of-flight can not be resolved. Very fast ions present an even greater concern, as discussed in Sec. 3.1.1 because the plume is expected to have a significant forward velocity away from the target. With the flight tube perpendicular to the plume direction, ions above a certain velocity will hit the wall of the flight tube before reaching the detector, as simulated in Sec. 3.1.1. Due to collisions in the plume, however, a significant number of these very fast ions are scattered in the perpendicular direction along the axis of the flight tube and are detected by the mass spectrometer, but these scattered ions may not necessarily be representative of the fast ion population.

The other major concern is that the repellers may alter the plume as the ions are being sampled. While the simulations show a linear electric field between the repellers and trajectories from the ablation chamber to the microchannel plate, these calculations are valid for a single ion under idealized conditions. Interactions between the ions in the plume and between the ions and the electrodes, especially after the high voltage repellers are applied, may influence how the plume is sampled. By creating an electric field across the plume, the repellers are effectively forcing all the charged particles toward the mass spectrometer, so the very act of measuring the ions may inadvertently change their intensity and distribution. Ion interactions during sampling are especially likely when examining the far side of the plume, because the rest of the plume remains between the ions from the far side and the entrance to the mass spectrometer as the ions of interest are being ejected.

Isotope separation does appear to take place at two points during the development of the laser plume. Among the fast ions, the ^{109}Ag peak has been shown to lead ^{107}Ag consistently in time and space. At early times, the spatial profiles always show the ^{109}Ag slightly ahead of the ^{107}Ag distribution, and the reflectron parameters suggest that these fast ions originate from the near side of the plume with high velocities in the orthogoal direction as well as in the direction of the plume. Although it is counterintuitive for the heavier isotopes to appear first, this result has been repoduced for a wide range of instrument parameters. One possible explanation is that a positive space charge from the early ions, which appear before the fast ion peak and are too fast to be measured by the instrument, preferentially pushes the lighter ions back toward the target, leaving the heavier ions in front.

The other instance of isotope separation is even more surprising and difficult to explain. When the repeller and reflectron voltages are set to sample ions from the side of the plume away from the mass spectrometer, an additional ^{109}Ag peak suddenly appears at later times without a corresponding ^{107}Ag peak. This is especially puzzling, considering that no such ions are found when examining the near side of the plume. Based on the spatial profiles, these extra ^{109}Ag ions appear as though they were originally part of the fast peak but have remained stationary instead of moving forward with the ^{107}Ag peak. Although this description of the phenomenon can not be independently confirmed, the experiments have consistently revealed the presence of these extra ^{109}Ag ions when the far side of the plume is sampled. Space charge may play a role here as well, by allowing the heavier ions to cross the plume toward the mass spectrometer while deflecting the lighter ions off-axis [81, 82]. Under this scenario, pulsing the repellers would lead to a large change in the measured isotope ratio, even if the isotopes were not separated in the original plume. The effect observed, however, is inordinately large given the small mass difference between the silver isotopes.

5.3 Future Work

Despite extensive study of this phenomenon, many questions remain regarding the mechanism of isotope separation during laser ablation. This section outlines potential directions for future work on this topic. The first two parts describe specific courses of action in terms of modifying the instrument and examining the phenomenon respectively while the last part suggests a novel application for the methods and instrumentation developed in this study.

5.3.1 Instrument Development

Given the limitations of the equipment, most of the avenues for characterizing isotope separation have been exhausted over the course of this study. If this instrument were to be used for further experiments, these two changes would expand the range and specificity of the system and could lead to improved results.

The first is an increase in the maximum voltage on the repeller plates, which is limited by both the power supply and the high voltage switch. This would allow for a higher electric field and a sharper potential gradient between the repellers. If this gradient were large enough, the kinetic energy of the ions might indeed be negligible compared to the potential energy at different parts of the plume. As a result, the voltage range of the reflectron would correspond much more closely to the position of the ion rather than position convoluted with velocity, as with the current parameters.

Second, the grid in front of the detector should be independently controlled instead of being tied to the flight tube liner. This would provide a more direct mechanism for filtering out ions below the energy threshold than using the reflectron to deflect them off-axis. With the grid serving as the low energy filter, the lower reflectron voltage would be free to perform its primary role of reducing the temporal spread of the ions. Under this configuration, the upper reflectron voltage would place an upper limit on the ion energies, the detector grid would set the lower limit, and the lower reflectron voltage would be used solely to optimize the reflectron for mass resolution instead of the performing the last two roles simultaneously, as is the case in the current setup. With an independent low energy filter, not only would mass resolution improve, but there would be much more flexibility in specifying which lateral slice to measure.

5.3.2 Atomic Absorption Spectrometry

As described above, the time-of-flight mass spectrometer itself poses a lot of challenges for studying laser ablation. Some of the ions can not be observed, and the very process of sampling the plume inevitably alters it in ways that are difficult to quantify. Furthermore, a complex scheme for setting the parameters is required to specify which part of the plume is being sampled. Thus, while time-of-flight mass spectrometry is excellent at obtaining isotope ratios, there may be a better technique for studying the ions in the laser plume.

Chief among these is atomic absorption spectrometry. Although absorption spectrometry has much lower sensitivity compared to mass spectrometry and high-resolution diode lasers are needed to distinguish different isotopes, this technique allows for direct interrogation of the laser plume with much less concern for the ion velocities. The spatial profile can be obtained by moving the beam or the target and the resolution is determined by the laser beam. In addition, a complete temporal profile can be obtained with each shot, since absorption is monitored continuously. The primary disadvantage of this technique compared to time-of-flight mass spectrometry is the difficulty measuring two isotopes at the same time. If two diode lasers are used, for example, they must be aligned such that they pass through the plume at the same location [67]. Nevertheless, such direct measurements of the plume hold significant advantages and should be considered for investigating this phenomenon. Furthermore, if the ultimate goal of the research is to improve optical means of isotope detection, using optical techniques to study laser ablation might ease the transition from theory to application.

5.3.3 Chemistry in the Laser Plume

Although this study could not provide definitive conclusions regarding isotope separation in the laser plume, the capabilities demonstrated by the instrument suggest that time-of-flight mass spectrometry might be even more helpful for studying plasma chemistry during laser ablation. The same techniques used to obtain the isotope distribution in the plume could be applied to inorganic diatoms or molecular fragments in order to monitor their concentration at different positions and different times during ablation. Providing this detailed description of the chemistry in the plume would be helpful for any technique in which laser ablation is used to sample molecules or compounds. Knowing when and where oxides form, for example, is especially important for laser ablation molecular isotope spectroscopy. This system could be used to analyze the temporal and spatial profile of molecular ions during laser ablation and, in doing so, improve the detection of isotopes in the laser plume.

References

[1] C. Talmadge, “Deterring a Nuclear 9/11”, The Washington Quarterly **30**, 21 (2007).

[2] A. Lowrey, “Obama Calls Oil Sufficient to Cut Reliance On Iran”, The New York Times, March 31, 2012, A1.

[3] J. Rogin, “Obama says there’s enough oil in the world to cut off Iran”, `http://thecable.foreignpolicy.com/posts/2012/03/30/obama_says_there_s_enough_oil_in_the_world_to_cut_off_iran`, March 30, 2012.

[4] S. L. Myers and S.-H. Choe, “North Koreans Agree to Freeze Nuclear Efforts”, The New York Times, March 1, 2012, A1.

[5] J. Rogin, “Nuke deal: State talks moratorium, North Korea talks food”, `http://thecable.foreignpolicy.com/posts/2012/02/29/us_and_north_korea_disagree_on_what_was_agreed_at_meeting`, February 29, 2012.

[6] T. Masse, “Nuclear Terrorism Redux: Conventionalists, Skeptics, and the Margin of Safety”, Orbis **54**, 302 (2010).

[7] United Nations, “Treaty on the Non-Proliferation of Nuclear Weapons (NPT)”, `http://www.un.org/disarmament/WMD/Nuclear/NPTtext.shtml`, 1968.

[8] D. L. Donohue, “Strengthening IAEA safeguards through environmental sampling and analysis”, Journal of Alloys and Compounds **271-273**, 11 (1998).

[9] M. Kraiem, S. Richter, H. Kühn, and A. Y., “Development of an improved method to perform single particle analysis by TIMS for nuclear safeguards”, Analytica Chimica Acta **688**, 1 (2011).

[10] International Atomic Energy Agency, IAEA Safeguards Glossary, 2002.

[11] T. B. Taylor, “Nuclear Safeguards”, Annual Review of Nuclear Science **25**, 407 (1975).

[12] P. M. Grant, K. J. Moody, I. D. Hutcheon, D. L. Phinney, R. E. Whipple, A. A. Haas, J. S., J. E. Andrews, G. L. Klunder, R. E. Russo, T. E. Fickies, G. E. Pelkey, B. D. Andresen, D. A. Kruchten, and S. Cantlin, "Nuclear forensics in law enforcement applications", Journal of Radioanalytical and Nuclear Chemistry **235**, 129 (1998).

[13] W. H. Dunlop and H. P. Smith, "Who Did It? Using International Forensics to Detect and Deter Nuclear Terrorism", Arms Control Today **36**, 6 (2006).

[14] M. May, J. Davis, and R. Jeanloz, "Preparing for the worst", Nature **443**, 907 (2006).

[15] É. Széles, Z. Varga, and Z. Stefánka, "Sample preparation method for analysis of swipe samples by inductively coupled plasma mass spectrometry", Journal of Analytical Atomic Spectrometry **25**, 1014 (2010).

[16] D. L. Donohue, "Peer Reviewed: Strengthened Nuclear Safeguards", Analytical Chemistry **74**, 28A (2002).

[17] J. Švedkauskaitė LeGore, K. Mayer, S. Millet, A. Nicholl, R. G., and D. Baltrūnas, "Investigation of the isotopic composition of lead and of trace elements concentrations in natural uranium materials as a signature in nuclear forensics", Radiochimica Acta **95**, 601 (2007).

[18] K. Mayer and M. F. Wallenius, "Nuclear forensic science—From cradle to maturity", Journal of Alloys and Compounds **444-445**, 50 (2007).

[19] K. Mayer, M. Wallenius, and I. Ray, "Nuclear forensics—a methodology providing clues on the origin of illicitly trafficked nuclear materials", Analyst **130**, 433 (2005).

[20] M. Wallenius, P. Peerani, and L. Koch, "Origin determination of plutonium material in nuclear forensics", Journal of Radioanalytical and Nuclear Chemistry **246**, 317 (2000).

[21] K. J. Moody, I. D. Hutcheon, and P. M. Grant, *Nuclear Forensic Analysis*, CRC Press, 2005.

[22] B. Pellaud, "Proliferation aspects of plutonium recycling", Comptes Rendus Physique **3**, 1067 (2002).

[23] H. C. Paxton, Los alamos critical-mass data, Technical Report LAMS-3067, Los Alamos Scientific Laboratory, 1964.

[24] M. Magara, T. Sakakibara, S. Kurosawa, M. Takahashi, S. Sakurai, Y. Hanzawa, F. Esaka, K. Watanabe, and S. Usuda, "Isotope Ratio Measurement of Uranium in Safeguards Environmental Samples by Inductively-Coupled Plasma Mass Spectrometry (ICP-MS)", Journal of Nuclear Science and Technology **39**, 308 (2002).

[25] M. Wallenius and K. Mayer, “Age determination of plutonium material in nuclear forensics by thermal ionisation mass spectrometry”, Fresenius’ Journal of Analytical Chemistry **366**, 234 (2000).

[26] C. T. Nguyen, “Age-dating of highly enriched Uranium by γ-spectrometry”, Nuclear Instruments and Methods in Physics Research B **229**, 103 (2005).

[27] L.-E. De Geer, “Radionuclide Evidence for Low-Yield Nuclear Testing in North Korea in April/May 2010”, Science & Global Security: The Technical Basis for Arms Control, Disarmament, and Nonproliferation Initiatives **20**, 1 (2012).

[28] G. Tamborini, D. Phinney, O. Bildstein, and M. Betti, “Oxygen Isotopic Measurements by Secondary Ion Mass Spectrometry in Uranium Oxide Microparticles: A Nuclear Forensic Diagnostic”, Analytical Chemistry **74**, 6098 (2002).

[29] J. S. Becker, “State-of-the-art and progress in precise and accurate isotope ratio measurements by ICP-MS and LA-ICP-MS”, Journal of Analytical Atomic Spectrometry **17**, 1172 (2002).

[30] J. S. Becker, *Inorganic Mass Spectrometry: Principles and Applications*, Wiley, 2007.

[31] G. R. Gilmore, *Practical Gamma-Ray Spectrometry*, Wiley, 2nd edition, 2008.

[32] K. Abbas, G. Nicolaou, D. Pellottiero, P. Schwalbach, and L. Koch, “Gamma spectrometry of spent nuclear fuel using a miniature CdTe detector”, Nuclear Instruments and Methods in Physics Research A **376**, 248 (1996).

[33] C. T. Nguyen and J. Zsigrai, “Basic characterization of highly enriched uranium by gamma spectrometry”, Nuclear Instruments and Methods in Physics Research B **246**, 417 (2006).

[34] S. F. Terracol, A. Shafinaz, T. R. Niedermayr, I. D. Hau, O. B. Drury, Z. A. Ali, T. Miyazaki, M. F. Cunningham, J. G. Dreyer, J. D. Leacock, and S. Friedrich, “Ultra-High Resolution Gamma-Ray Spectrometer Development for Nuclear Attribution and Non-Proliferation Applications”, IEEE Nuclear Science Symposium Conference **2**, 1006 (2004).

[35] R. Gunnink, MGA: A gamma-ray spectrum analysis code for determining plutonium isotopic abundances. volume 1. methods and algorithms., Technical Report UCRL-LR-103220-Vol.1, Lawrence Livermore National Laboratory, 1990.

[36] A. J. Dempster, “A new method of positve ray analysis”, Physical Review Series II **11**, 316 (1918).

[37] J. R. de Laeter, *Applications of Inorganic Mass Spectrometry*, Wiley, 2001.

[38] X. Hou, W. Chen, Y. He, and B. T. Jones, "Analytical Atomic Spectrometry for Nuclear Forensics", Applied Spectroscopy Reviews **40**, 245 (2005).

[39] M. Betti, "Isotope ratio measurements by secondary ion mass spectrometry (SIMS) and glow discharge mass spectrometry (GDMS)", International Journal of Mass Spectrometry **242**, 169 (2005).

[40] V. R. Deline, C. A. Evans, Jr., and P. Williams, "A unified explanation for secondary ion yields", Applied Physics Letters **33**, 578 (1978).

[41] M. Betti, G. Tamborini, and L. Koch, "Use of Secondary Ion Mass Spectrometry in Nuclear Forensic Analysis for the Characterization of Plutonium and Highly Enriched Uranium Particles", Analytical Chemistry **71**, 2616 (1999).

[42] S. Greenfield, I. L. Jones, and C. T. Berry, "High-pressure Plasmas as Spectroscopic Emission Sources", Analyst **89**, 713 (1964).

[43] R. S. Houk, V. A. Fassel, G. D. Flesch, H. J. Svec, A. L. Gray, and C. E. Taylor, "Inductively coupled argon plasma as an ion source for mass spectrometric determination of trace elements", Analytical Chemistry **52**, 2283 (1980).

[44] H. Niu and R. S. Houk, "Fundamental aspects of ion extraction in inductively coupled plasma mass spectrometry", Spectrochimica Acta Part B: Atomic Spectroscopy **51**, 779 (1996).

[45] A. R. Date and A. L. Gray, "Development Progress in Plasma Source Mass Spectrometry", Analyst **108**, 159 (1983).

[46] A. R. Date and A. L. Gray, "Plasma Source Mass Spectrometry Using an Inductively Coupled Plasma and a High Resolution Quadrupole Mass Filter", Analyst **106**, 1255 (1981).

[47] B. S. Ross and G. M. Hieftje, "Alteration of the ion-optic lens configuration to eliminate mass-dependent matrix-interference effects in inductively coupled plasma-mass spectrometry", Spectrochimica Acta Part B: Atomic Spectroscopy **46**, 1263 (1991).

[48] C. N. Maréchal, P. Télouk, and F. Albarède, "Precise analysis of copper and zinc isotopic compositions by plasma-source mass spectrometry", Chemical Geology **156**, 251 (1999).

[49] N.-C. Chu, R. N. Taylor, V. Chavagnac, R. W. Nesbitt, R. M. Boella, J. A. Milton, C. R. German, G. Bayon, and K. Burton, "Hf isotope ratio analysis using multi-collector inductively coupled plasma mass spectrometry: an evaluation of isobaric interference corrections", Journal of Analytical Atomic Spectrometry **17**, 1567 (2002).

[50] R. E. Russo, X. L. Mao, C. Liu, and J. Gonzalez, "Laser assisted plasma spectrochemistry: laser ablation", Journal of Analytical Atomic Spectrometry **19**, 1084 (2004).

[51] D. Günther and B. Hattendorf, "Solid sample analysis using laser ablation inductively coupled plasma mass spectrometry", Trends in Analytical Chemistry **24**, 255 (2005).

[52] J. Woodhead, S. Swearer, J. Hergt, and R. Maas, "In situ Sr-isotope analysis of carbonates by LA-MC-ICP-MS: interference corrections, high spatial resolution and an example from otolith studies", Journal of Analytical Atomic Spectrometry **20**, 22 (2005).

[53] R. Hergenröder, "Laser-generated aerosols in laser ablation for inductively coupled plasma spectrometry", Spectrochimica Acta Part B: Atomic Spectroscopy **61**, 284 (2006).

[54] J. Gonzalez, X. L. Mao, J. Roy, S. S. Mao, and R. E. Russo, "Comparison of 193, 213 and 266 nm laser ablation ICP-MS", Journal of Analytical Atomic Spectrometry **17**, 1108 (2002).

[55] R. E. Russo, X. Mao, J. J. Gonzalez, and S. S. Mao, "Femtosecond laser ablation ICP-MS", Journal of Analytical Atomic Spectrometry **17**, 1072 (2002).

[56] G. S. Hurst, M. G. Payne, S. D. Kramer, and J. P. Young, "Resonance ionization spectroscopy and one-atom detection", Reviews of Modern Physics **51**, 767 (1979).

[57] K. Wendt and N. Trautmann, "Recent developments in isotope ratio measurements by resonance ionization mass spectrometry", International Journal of Mass Spectrometry **242**, 161 (2005).

[58] Z. Ma, R. N. Thompson, K. R. Lykke, M. J. Pellin, and A. M. Davis, "New instrument for microbeam analysis incorporating submicron imaging and resonance ionization mass spectrometry", Review of Scientific Instruments **66**, 3168 (1995).

[59] D. A. Cremers, A. Beddingfield, R. Smithwick, R. C. Chinni, C. R. Jones, B. Beardsley, and L. Karch, "Monitoring Uranium, Hydrogen, and Lithium and Their Isotopes Using a Compact Laser-Induced Breakdown Spectroscopy (LIBS) Probe and High-Resolution Spectrometer", Applied Spectroscopy **66**, 250 (2012).

[60] W. Pietsch, A. Petit, and A. Briand, "Isotope ratio determination of uranium by optical emission spectroscopy on a laser-produced plasma - basic investigations and analytical results", Spectrochimica Acta Part B: Atomic Spectroscopy **53**, 751 (1998).

[61] B. W. Smith, I. B. Gornushkin, L. A. King, and J. D. Winefordner, "A laser ablation-atomic fluorescence technique for isotopically selective determination of lithium in solids", Spectrochimica Acta Part B: Atomic Spectroscopy **53**, 1131 (1998).

[62] R. E. Russo, A. A. Bol'shakov, X. Mao, C. P. McKay, D. L. Perry, and O. Sorkhabi, "Laser Ablation Molecular Isotopic Spectrometry", Spectrochimica Acta Part B: Atomic Spectroscopy **66**, 99 (2011).

[63] C. López-Moreno, S. Palanco, J. J. Laserna, F. DeLucia, Jr., A. W. Miziolek, J. Rose, R. A. Walters, and A. I. Whitehouse, "Test of a stand-off laser-induced breakdown spectroscopy sensor for the detection of explosive residues on solid surfaces", Journal of Analytical Atomic Spectrometry **21**, 55 (2006).

[64] B. W. Smith, A. Quentmeier, M. Bolshov, and K. Niemax, "Measurement of uranium isotope ratios in solid samples using laser ablation and diode laser-excited atomic fluorescence spectrometry", Spectrochimica Acta Part B: Atomic Spectroscopy **54**, 943 (1999).

[65] A. Quentmeier, M. Bolshov, and K. Niemax, "Measurement of uranium isotope ratios in solid samples using laser ablation and diode laser-atomic absorption spectrometry", Spectrochimica Acta Part B: Atomic Spectroscopy **56**, 45 (2001).

[66] L. A. King, I. B. Gornushkin, D. Pappas, B. W. Smith, and J. D. Winefordner, "Rubidium isotope measurements in solid samples by laser ablation-laser atomic absorption spectroscopy", Spectrochimica Acta Part B: Atomic Spectroscopy **54**, 1771 (1999).

[67] H. Liu, A. Quentmeier, and K. Niemax, "Diode laser absorption measurement of uranium isotope ratios in solid samples using laser ablation", Spectrochimica Acta Part B: Atomic Spectroscopy **57**, 1611 (2002).

[68] B. A. Bushaw and N. C. Anheier, Jr., "Isotope ratio analysis on micron-sized particles in complex matrices by Laser Ablation-Absorption Ratio Spectrometry", Spectrochimica Acta Part B: Atomic Spectroscopy **64**, 1259 (2009).

[69] C. A. Smith, M. A. Martinez, D. K. Veirs, and D. A. Cremers, "Pu-239/Pu-240 isotope ratios determined using high resolution emission spectroscopy in a laser-induced plasma", Spectrochimica Acta Part B: Atomic Spectroscopy **57**, 929 (2002).

[70] K. H. Kurniawan and K. Kiichiro, "Hydrogen and Deuterium Analysis Using Laser-Induced Plasma Spectroscopy", Applied Spectroscopy Reviews **41**, 99 (2006).

[71] A. D'Ulivo, M. Onor, E. Pitzalis, R. Spiniello, L. Lampugnani, G. Cristoforetti, S. Legnaioli, V. Palleschi, A. Salvetti, and T. E., "Determination of the deuterium/hydrogen ratio in gas reaction products by laser-induced breakdown spectroscopy", Spectrochimica Acta Part B: Atomic Spectroscopy **61**, 797 (2006).

[72] F. R. Doucet, G. Lithgow, R. Kosierb, P. Bouchard, and M. Sabsabi, "Determination of isotope ratios using Laser-Induced Breakdown Spectroscopy in ambient air at atmospheric pressure for nuclear forensics", Journal of Analytical Atomic Spectrometry **26**, 536 (2011).

[73] H. Niki, T. Yasuda, and I. Kitazima, "Measurement Technique of Boron Isotopic Ratio by Laser-induced Breakdown Spectroscopy", Journal of Nuclear Science and Technology **35**, 34 (1998).

[74] X. Mao, A. A. Bol'shakov, D. L. Perry, O. Sorkhabi, and R. E. Russo, "Laser Ablation Molecular Isotopic Spectrometry: Parameter influence on boron isotope measurements", Spectrochimica Acta Part B: Atomic Spectroscopy **66**, 604 (2011).

[75] X. Mao, A. A. Bol'shakov, I. Choi, C. P. McKay, D. L. Perry, O. Sorkhabi, and R. E. Russo, "Laser Ablation Molecular Isotopic Spectrometry: Strontium and its isotopes", Spectrochimica Acta Part B: Atomic Spectroscopy **66**, 604 (2011).

[76] P. D. Gupta, R. Bhatnagar, and D. D. Bhawalkar, "Isotopic enhancement in laser-produced plasmas", Journal of Applied Physics **51**, 3422 (1980).

[77] P. P. Pronko, P. A. VanRompay, Z. Zhang, and J. A. Nees, "Isotope Enrichment in Laser-Ablation Plumes and Commensurately Deposited Thin Films", Physical Review Letters **83**, 2596 (1999).

[78] P. D. Gupta and P. A. Naik, "Comment on "Isotope Enrichment in Laser-Ablation Plumes and Commensurately Deposited Thin Films"", Physical Review Letters **86**, 1386 (2001).

[79] P. A. VanRompay, Z. Zhang, J. A. Nees, and P. P. Pronko, "Isotope separation and enrichment by ultrafast laser ablation", Proceedings of SPIE **3934**, 43 (2000).

[80] S. H. Tan and G. Horlick, "Matrix-effect observations in inductively coupled plasma mass spectrometry", Journal of Analytical Atomic Spectrometry **2**, 745 (1987).

[81] G. R. Gillson, D. J. Douglas, J. E. Fulford, K. W. Halligan, and S. D. Tanner, "Non-spectroscopic interelement interferences in inductively coupled plasma mass spectrometry", Analytical Chemistry **60**, 1472 (1988).

[82] S. D. Tanner, "Space charge in ICP-MS: calculation and implications", Spectrochimica Acta Part B: Atomic Spectroscopy **47**, 809 (1992).

[83] J. W. Olesik and M. P. Dziewatkoski, "Time-resolved measurements of individual ion cloud signals to investigate space-charge effects in plasma mass spectrometry", Journal of the American Society for Mass Spectrometry **7**, 362 (1996).

[84] T. W. Burgoyne, G. M. Hieftje, and R. A. Hites, "Space Charge Evaluation in a Plasma-Source Mass Spectrograph", Analytical Chemistry **69**, 485 (1997).

[85] R. E. Russo, G. L. Klunder, P. Grant, and B. D. Andresen, "Laser ablation ion-storage time-of-flight mass spectrometry", Applied Physics A: Materials Science & Processing **69**, S895 (1999).

[86] G. L. Klunder, P. M. Grant, B. D. Andresen, and R. E. Russo, "Direct Chemical Analysis of Solids by Laser Ablation in an Ion Storage Time-of-Flight Mass Spectrometer", Analytical Chemistry **76**, 1249 (2004).

[87] D. M. Chambers, L. I. Grace, and B. D. Andresen, "Development of an Ion Store/Time-of-Flight Mass Spectrometer for the Analysis of Volatile Compounds in Air", Analytical Chemistry **69**, 3780 (1997).

[88] J. K. Böhlke, J. R. de Laeter, P. De Bièvre, H. Hidaka, H. S. Peiser, K. J. R. Rosman, and P. D. P. Taylor, Isotopic compositions of the elements, 2001, Technical report, International Union of Pure and Applied Chemistry, 2001.

[89] H. Liu, O. V. Borisov, X. Mao, S. Shuttleworth, and R. E. Russo, "Pb/U Fractionation during Nd:YAG 213 nm and 266 nm Laser Ablation Sampling with Inductively Coupled Plasma Mass Spectrometry", Applied Spectroscopy **54**, 1435 (2000).

[90] COMSOL AB, *COMSOL Multiphysics: Modeling Guide, Version 3.4*, 2007.

[91] D. J. Manura and D. A. Dahl, *SIMION Version 8.0: User Manual*, 2008.

[92] R. Kelly, "On the dual role of the Knudsen layer and unsteady, adiabatic expansion in pulse sputtering phenomena", Journal of Chemical Physics **92**, 5047 (1990).

[93] M. S. Rafique, M. Khaleeq-ur Rahman, M. S. Anwar, F. M. A. Ashfaq, and K. Siraj, "Angular distribution and forward peaking of laser produced plasma ions", Laser and Particle Beams **23**, 131 (2005).

[94] M. Guilhaus, "Principles and Instrumentation in Time-of-flight Mass Spectrometry: Physical and Instrumental Concepts", Journal of Mass Spectrometry **30**, 1519 (1995).

[95] B. A. Mamyrin, "Laser assisted reflectron time-of-flight mass spectrometry", International Journal of Mass Spectrometry and Ion Processes **131**, 1 (1994).